UCONN LIBRARY

University of Connecticut
OpenCommons@UConn

Doctoral Dissertations | University of Connecticut Graduate School

7-28-2017

Exploring Heterogeneities near Earth's Inner Core Boundary with Seismic Body Waves

MANAWADUGE S. DESILVA
University of Connecticut, susinidesilva@gmail.com

Follow this and additional works at: https://opencommons.uconn.edu/dissertations

Recommended Citation
DESILVA, MANAWADUGE S., "Exploring Heterogeneities near Earth's Inner Core Boundary with Seismic Body Waves" (2017). *Doctoral Dissertations*. 1569.
https://opencommons.uconn.edu/dissertations/1569

Exploring Heterogeneities near Earth's Inner Core Boundary with Seismic Body Waves

Manawaduge Susini S. de Silva, PhD

University of Connecticut, 2017

The existence of inner core boundary (ICB) topography can affect the amplitude, phase, and coda of body waves incident on the inner core. Applying pseudo spectral and boundary element methods to synthesize compressional waves interacting with the ICB, these effects are predicted and compared with waveform observations in pre-critical to diffraction ranges of the wave reflected from the inner core boundary. In the pre-critical range, data require an upper bound of 2 km at 1-20 km wavelength for any ICB topography. Higher topography sharply reduces PKiKP amplitude and produces time-extended coda not observed in PKiKP waveforms. Topography of this scale smooths over minima and zeros in the pre-critical ICB reflection coefficient predicted from standard Earth models. In the diffracted range, topography as high as 5 km attenuates the peak amplitudes of PKIKP and PKP_{Cdiff} by similar amounts, leaving the PKP_{Cdiff}/PKIKP amplitude ratio unchanged from that predicted by a smooth ICB. The observed decay of PKP_{Cdiff} into the inner core shadow and the PKIKP-PKP_{Cdiff} differential travel times are consistent with a flattening of the outer core P velocity gradient near the ICB and iron enrichment in the lowermost 100 km of the outer core.

A search for the best fitting attenuation structure was conducted with a collection of synthetic seismograms generated with Qp = [100–1000] for the upper 80 km of inner core and Qk = [300,1000,57822] for the lower 200 km of outer core. Best cross-correlation coefficients higher than 80% resulted from $Qp^{-1} \geq 0.003$ in latitude range

[45°E-180°E,180°W-90°W] and Qp^{-1}=0.001 in latitude range [90°W-45°E], with Qk^{-1}=0.001 in majority of the lowermost outer core. Since boundary element modelling of the inner core boundary shows that sinusoidal or fractal topography heights up to 5 km influences PKiKP and PKIKP minimally at post-critical distances, the observed attenuation structure solely depicts intrinsic loss of energy and volumetric scattering. Attenuations stronger than those given in the Preliminary Earth Reference Model (Dziewonski and Anderson, 1981) in the lower outer core may point towards increased viscosity resulting from iron enrichment in F-layer, which is consistent with the inner core boundary modelling of boundary element method.

Exploring Heterogeneities near Earth's Inner Core Boundary with Seismic Body Waves

Manawaduge Susini S. de Silva

B.Sc., University of Colombo – Sri Lanka, **2010**

M.S., University of Connecticut – United States of America, **2013**

A Dissertation

Submitted in Partial Fulfillment of the

Requirements for the Degree of

Doctor of Philosophy

at the

University of Connecticut

2017

Copyright by

Manawaduge Susini S. de Silva

2017

APPROVAL PAGE

Doctor of Philosophy Dissertation

Exploring Heterogeneities near Earth's Inner Core Boundary with Seismic Body Waves

Presented by

Manawaduge Susini S. de Silva, B.Sc., M.S.

Major Advisor

_____

Vernon F. Cormier

Associate Advisor

_____

Michael Bergman

Associate Advisor

_____

Winthrop Smith

University of Connecticut
2017

Acknowledgement

First and foremost, I am deeply grateful to my advisor Prof. Vernon Cormier without whose support I would not have been able to complete this work. I am indebted to him for sharing his extensive knowledge in Geophysics, as well as for offering valuable advice towards making progress in graduate school. Thank you very much being a great advisor. I also thank my thesis advisory committee Prof. Mike Bergman and Prof. Win Smith, my initial advisory committee Prof. Lanbo Liu, and Prof. Vasili Kharchenko, as well as the additional defense committee members Prof. George Rawitscher and Prof. Jonathan Trump for their invaluable feedback and support in improving my dissertation. I am extremely thankful to Prof. Lanbo Liu for his guidance and encouragement via many seminars and coursework. I thank Prof. Yingcai Zheng for his very helpful collaboration throughout my PhD project and graciously offering advise whenever I needed. I am much grateful to Dr. Januka Attanayake for his collaborations, mentoring, and advise throughout this time.

Experiments in this thesis were carried out in several High Performance Computing facilities. I especially thank the administrators of UConn HPC managed by Booth Engineering Center for Advanced Technology, and Xfrac cluster managed by Yingcai Zheng at University of Houston for granting access to their facilities and for responding to my all questions without hesitation. Calculations were also performed on the ANU Terrawulf cluster, a computational facility developed with support from the AuScope initiative. AuScope Ltd is funded under the National Collaborative Research Infrastructure Strategy (NCRIS), an Australian Commonwealth Government Programme.

The work in this thesis was funded by National Science Foundation grants. I am grateful for the NSF research support as well as the Teaching Assistantships from Department of Physics, University of Connecticut.

I am fortunate to have had the company of a great group of past/present graduate student members in our research group; amongst them are Januka, Chris, Yiteng, Michelle, and Steve. I am grateful for the friendships and supportive voices of many graduate students at UConn who are certainly a part of this journey. Moving to USA all the way across the globe from my home country Sri Lanka, and adjusting to a whole new life style has been as much a challenge as completing a research dissertation itself, which I could only accomplish thanks to many motivating individuals. Let me extend my sincere gratitude to all of them. Also, here is a shout out to Sri Lankans in Connecticut/Boston who always kept that home-feeling alive. Last but not least, I am immensely grateful to my husband Lahiru and my family for their support and encouragement all the way.

TABLE OF CONTENT

TABLE OF FIGURES

LIST OF TABLES

NOMENCLATURE

P wave	Compressional/Longitudinal seismic wave
S wave	Shear/Transverse seismic wave
Vp, Vs	Compressional wave velocity, Shear wave velocity
GCD	Great Circle Distance between station and event/ also given as a standalone degree angle
IC	Inner Core
OC	Outer Core
ICB	Inner Core Boundary
CMB	Core Mantle Boundary
PKiKP	P ray reflected from the top of inner core boundary
PKIKP or PKP_{DF}	P ray refracted through the inner core
PKPCdiff	P ray diffracting along the ICB
PKP_{BC}	P ray that turns in the outer core due to velocity gradient along the radius
PKIIKP	P ray that is reflected once at the ICB underside
PREM	Preliminary Reference Earth Model – A standard 1-D Earth model of material properties.
AK135	Another standard 1-D Earth model of material properties that are different than PREM, including near the ICB discontinuity.
QWH or WH	Quasi Western Hemisphere (~180W - 45E)
QEH or EH	Quasi Eastern Hemisphere (~45E - 180E)
Central Pacific Region	180W - 90W
Super rotation/ differential rotation	Rotation of the inner core faster than the mantle
Ray	Trajectory of the normal to the wavefront of a propagating body wave
Ray Parameter	Given by $Rsin(\theta_i)/V$ where R, θ_i, and V are radius,

	incident angle, and velocity at the point. Ray parameter is constant along a given ray.
Slowness	Given by 1/V. Ray parameter represents the slowness of a wavefront in horizontal direction.
Intrinsic/viscoelastic attenuation	Attenuation caused by energy loss due to molecule vibrations
Apparent attenuation (Q^{-1})	Total attenuation of energy due to viscoelastic and scattering effects. Q_p^{-1}, and Q_k^{-1} specifically denotes compressional wave attenuation and bulk wave attenuation, where latter is a linear combination of compressional and shear wave attenuations.

SUMMARY

The mechanism of inner core solidification drives the compositional and thermal convection in fluid outer core, sustaining the geodynamo that gives rise to Earth's magnetic field. Hence any differences in the manner of crystal growth and heat flux at the continuously growing inner core boundary (ICB) is essential in understanding secular variations of geomagnetic field around the Earth. Many previous geodynamic modeling and seismic investigations provide evidence of such differences in solidification rates. Properties of inner core needs to be well constrained in order to understand the growth and deformation mechanisms. We thoroughly investigate the possibility and dimensions of topography on ICB as well as use a cross correlation method to invert for the best fitting attenuation structure above and below this growing discontinuity, which would be beneficial for further exploring the growth mechanism.

The existence of topography of the inner core boundary (ICB) can affect the amplitude, phase, and coda of body waves incident on the inner core. Applying pseudo spectral and boundary element methods to synthesize compressional waves interacting with the ICB, these effects are predicted and compared with waveform observations in pre-critical, critical, post-critical, and diffraction ranges of the wave reflected from the inner core boundary (PKiKP). In the pre-critical range, data require an upper bound of 2 km at 1 to 20 km wavelength for any ICB topography. Higher topography sharply reduces PKiKP amplitude and produces time-extended coda not observed in PKiKP waveforms. The existence of topography of this scale smooths over minima and zeros in

the pre-critical ICB reflection coefficient predicted from standard Earth models. It is still possible that the previously predicted effects on reflected amplitudes by a higher ICB density contrast or a mosaic impedance structure could be masked by the scattering effects of very small topography heights. In the range surrounding critical incidence (117.5^o) as well as in the post-critical 130^o-140^o range, this plausible upper bound of topography does not strongly affect the amplitude and waveform behavior of PKIKP + PKiKP. In the diffracted range (>152°), both plausible and topography as high as 5 km is predicted to attenuate the peak amplitudes of PKIKP and PKP_{Cdiff} by similar amounts, leaving the PKP_{Cdiff}/PKIKP amplitude ratio unchanged from that predicted by a smooth ICB. The observed decay of PKP_{Cdiff} into the inner core shadow and the PKIKP-PKP_{Cdiff} differential travel time are consistent with a flattening of the outer core P velocity gradient near the ICB and iron enrichment in the lowermost 100 km of the outer core.

A search for best fitting attenuation structure was conducted with a collection of synthetic seismograms generated with Qp = [100 – 1000] for the upper 80 km of inner core and Qk = [300, 1000, 57822] for the lower 200 km of outer core. Waveforms PKiKP+PKIKP of event-station distances lying between 130^o – 140^o were cross-correlated with the synthetics. Best cross-correlation coefficients higher than 80% resulted from $Qp^{-1} \geq 0.003$ in latitude range [45^{o}E - 180^{o}E, 180^{o}W - 90^{o}W] and Qp^{-1} = 0.001 in latitude range [90^{o}W - 45^{o}E], with Qk^{-1} = 0.001 in majority of the lowermost outer core. Since boundary element modelling of the inner core boundary shows that sinusoidal or fractal topography heights up to 5 km influences PKiKP and PKIKP minimally at post-critical distances the observed attenuation structure solely depicts intrinsic loss of energy and volumetric scattering. Attenuations stronger than those given

in the Preliminary Earth Reference Model (Dziewonski and Anderson, 1981) in the lower outer core may point towards increased viscosity resulting from iron enrichment in F-layer, which is consistent with the inner core boundary modelling of boundary element method.

The synthesized PKiKP, PKIKP, and PKP_{CDiff} waveform results can be used as a basis to carefully probe geographical distribution of topography using careful sets of data in future. Specifically confirming the levels of topography in transfer zones between high Vp and low Vp regions such as edges around Pacific region, may be helpful to establish the detailed mechanism of inner core growth or melting plausible in each region.

Chapter I

Seismic Imaging of Earth's Core

1.1 Background

1.1.1 Seismic Imaging of the Earth

The only way to directly sense the current status of the deep interior of a telluric planet is by using seismic waves. These vibrations of elastic/acoustic material, caused either by earthquakes or explosions, penetrate through many different layers of the planet varying in velocity and attenuation depending on the material in each region. What are observed at a seismic station are the final amplitudes of seismic pulses arriving at different times after travelling through a variety of materials. Clearly it is possible that many different combinations of interior structures could mimic a certain pulse in a seismogram. This is where seismological modeling comes in, enabling the analysis of various attributes of a pulse such as their amplitude, travel time, phase and

pulse-width to understand the materials a seismic wave sampled along the way. Sometimes it is useful to collectively study two or more pulses in a seismic trace to resolve information for particular layers of the planet. Several different types of waves that are frequently used in this thesis and their nomenclature are shown in figure 1 and their approximate travel times are shown in figure 2.

A seismic event generates energy that propagates as dispersive surface waves over the crust and upper mantle and as body waves that penetrate the deeper interior of the planet. Body waves fall into two types; compressional waves (termed P waves) travelling parallel to the direction of particle vibrations and shear waves (termed S waves) travelling perpendicular to the direction of particle vibrations. While both P and S waves efficiently render information about the mantle region, P wave observations are best for resolving features of the solid inner core that lies under the liquid outer core.

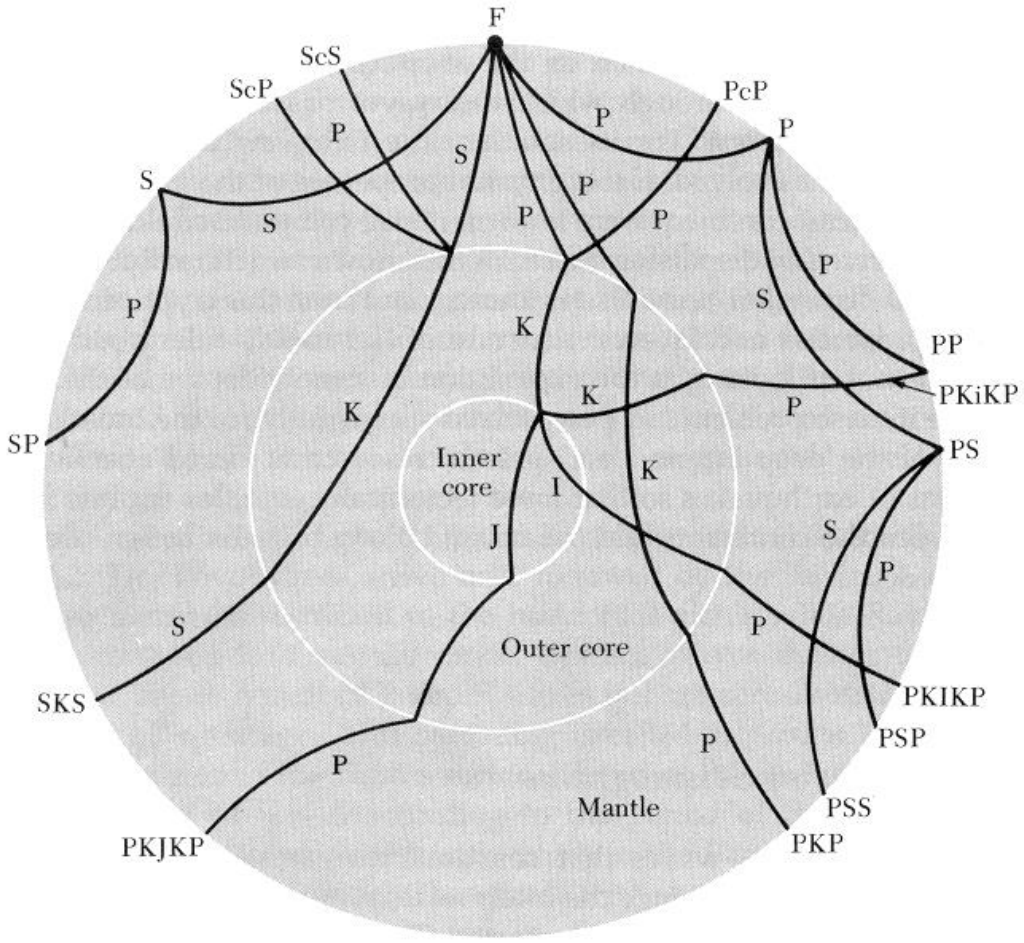

Figure 1: Seismic ray paths and their nomenclature (Bolt, 1993). F represents source. Notice that the final ray name is a combination of alphabetical letters assigned based on the basic layers passed and the particle vibration direction in each layer. For instance, the name for a ray leg in Mantle or Inner Core is P or I if they are longitudinal, while it is S or J if they are transverse. The fluid outer core only contains longitudinal rays called K. Reflections at the top of outer core and inner core are signified by 'c' and 'i' respectively, while a ray that diffracts along one of these boundaries bare the term 'diff' at the end of the name.

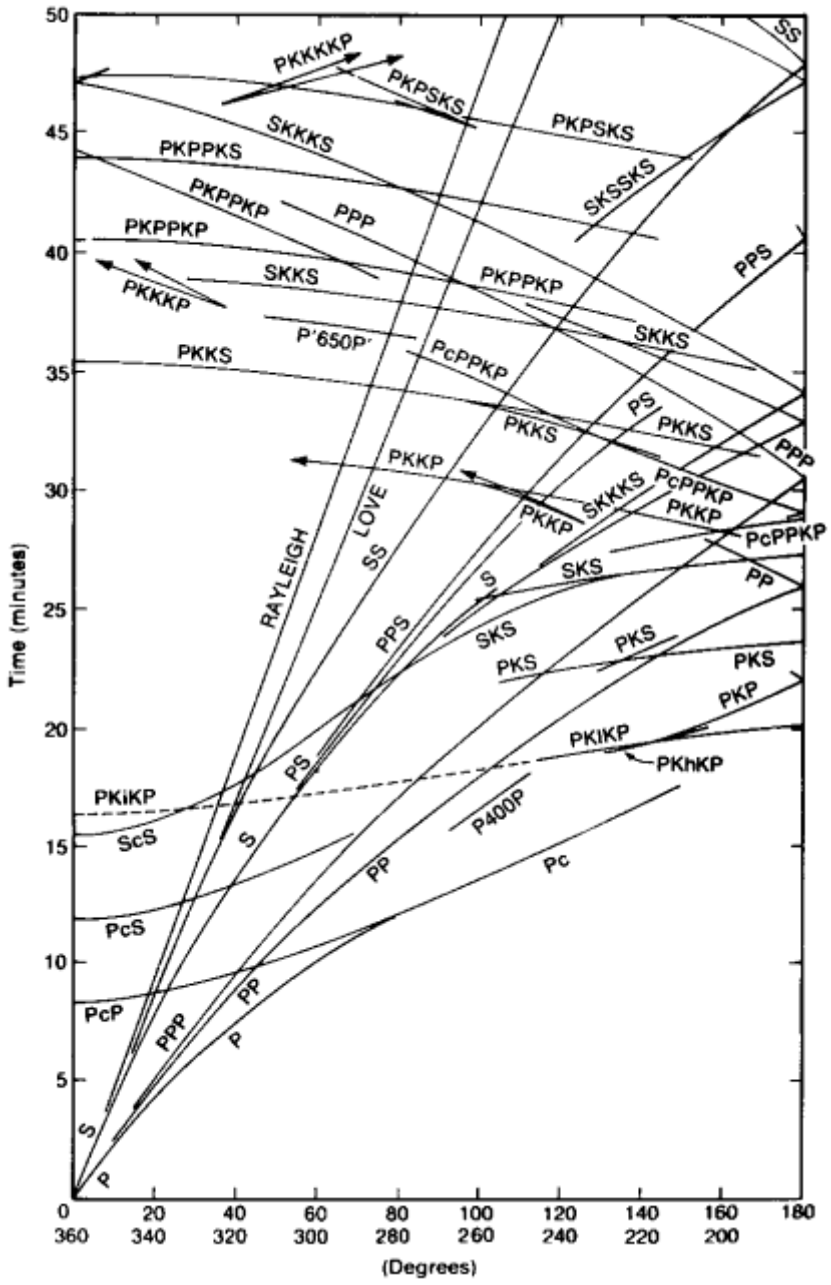

Figure 2: Travel time curves from Earthquakes (Bolt, 1976). Such graphs produced using arrival data or synthetic arrival predictions of models are useful in identifying pulses in seismographs.

With the advances in global seismic station networks, thousands of seismograms are presently available allowing a higher density of ray coverage to understand more intricate features in Earth layers. Each pulse in a seismogram, sans external noise, contains information about various regions. Seismologists use either forward or inverse modeling methods to decipher these observations and understand the interior of the planet. Our work involves forward modeling where iterative generations of synthetic seismograms with different combinations of model parameters are used to obtain the best fitting model to observations.

1.1.2 Core

The iron core of the Earth is presumed to be made by the collisions between planetesimals with sizes up to that of Mars (Chambers, 2001, 2004), some of which may have had their own cores, during the planetary accretion stage providing enough heat to melt silicates and iron while allowing the iron contents to be gravitationally pulled towards the center (Walter and Trønnes, 2004; Caro, 2011). The iron core of present day Earth is thus believed to have begun during planetary accretion.

1.1.2.1 Liquid Outer Core

The existence of a core was first confirmed by Oldham (Oldham, 1907) via observation of a discontinuity in S wave travel time seen beyond 120^{o} from an earthquake. The core was later predicted to be liquid (Jeffreys, 1926) and separated

from the solid Mantle at a depth of 2900 km (Gutenberg, 1914). In 1936 Inge Lehmann (Lehmann, 1936) predicted that an inner core should exist based on the fact that P waves of small amplitude actually do arrive within the previously estimated 'shadow zone' which assumed the entire core is liquid. It was later predicted that the inner core is solid (Bullen, 1946) and is solidifying from the outer core liquid (Birch, 1940). The outer and inner core densities are respectively 5-10% and 3-5% less than that of pure iron (McDonough, 2013), indicating mixing of lighter alloys/elements (such as Si, O and S), and possibly that lighter elements are preferentially partitioned into outer core during solidification.

1.1.2.2 Solid Inner Core

The solid inner core is comparatively more complex in heterogeneity than the well-mixed convecting liquid outer core. Since the discovery of the inner core complexities in its structure have been inferred, including lateral and vertical variations in seismic attenuation and velocity at hemispherical or smaller spatial scale (Tanaka and Hamaguchi, 1997; Niu and Wen, 2001; Irving and Deuss, 2011; Attanayake, Cormier and De Silva, 2014), elastic anisotropy (Morelli, Dziewonski and Woodhouse, 1986; Woodhouse, Giardini and Li, 1986; Tromp, 1993), structure above the inner core boundary (the F-Layer of Bullen, 1940, 1942), super rotation (Gubbins, 1981; Song and Richards, 1996a), and hints of an inner-inner core (Ishii and Dziewoński, 2002). The patterns and features in the inner core are likely to be related to its growth process which is tightly connected to the dynamics of the liquid outer core. Deeper signatures such as the existence of an inner-inner core with

different elastic properties and changes in the gradients of velocity or attenuation would reveal an older growth process or a change in mineralogical properties while shallower signatures such as the elastic structure around the ICB reveal recent patterns of heat transfer and the viscosity of the convecting outer core. Hence seismological probing of IC entails exciting clues about the mechanism that drives the geomagnetic field.

Although the manifestation of these seismic features such as velocity or attenuation heterogeneity, anisotropy, inner-inner core as well as boundary topography are evidence for the nature of IC growth, the main challenge is that there are trade-offs between each of them as to how they affect the probing seismic wave. For instance, isotropic velocity heterogeneities, velocity anisotropy, as well as ICB topography are all capable of causing ~1s perturbations to the travel time of the PKIKP wave sampling the upper inner core. This is where further understanding of how each structural parameter affects core-sensitive seismic phases are required, mainly via simulation experiments. In the following sections I discuss the structural parameters of the inner core inferred from seismic wave propagation as a prelude to the methods and results of my thesis.

1.1.2.2.1 Velocity Anisotropy

It is generally observed that compressional (P) elastic waves travel faster parallel to the Earth's spin axis than perpendicular to it within the inner core. The first suggestions of P velocity anisotropy in the inner core with a fast axis in the direction

of Earth rotation resulted from observation of a 2-3 s PKIKP travel time anomaly (Poupinet, Pillet and Souriau, 1983; Morelli, Dziewonski and Woodhouse, 1986) which was also supported by normal mode splitting observations (Masters and Gilbert, 1981; Woodhouse, Giardini and Li, 1986). Later studies predicted isotropic velocity layers of thickness less than 100 km (Song and Helmberger, 1995; Yu and Wen, 2007; Waszek and Deuss, 2011) or up to 250 km (Su and Dziewonski, 1995; Sun and Song, 2008) exist in an uppermost inner core, overlying a deeper anisotropic inner core.

1.1.2.2.2 Velocity heterogeneity

Studies of body wave arrival time measurements predict an interesting hemispherical dichotomy in the uppermost inner core separating the inner core into two hemispheres whereas the quasi-western hemisphere (approximately 180W-40E also termed QWH) shows higher anisotropy while the quasi-eastern hemisphere (approximately 40E-180E also termed QEH) shows lower or no anisotropy (Tanaka and Hamaguchi, 1997; Irving and Deuss, 2011). A similar pattern is confirmed with normal mode studies (Deuss, Irving and Woodhouse, 2010). QEH and QWH are found to have faster and slower Vp in uppermost IC respectively, with an indication of transitional hemispherical boundaries (Waszek, Irving and Deuss, 2011; Cormier and Attanayake, 2013) or in other words a hemispherical boundary that appears to move slightly eastward with depth. These boundaries on uppermost IC coincide with the division of lowermost outer core with lower Vp gradient on the west and higher Vp gradient on the east (Yu, Wen and Niu, 2005), making the faster eastern hemisphere of inner core

connect well with the faster eastern side of the F-layer. In addition there are suggestions of regional fluctuations of Vp such as the equatorial lower-than-average velocity zone beneath the Indian Ocean in QEH (Stroujkova and Cormier, 2004).

Understandably it is difficult to reconcile the tradeoffs between velocity anisotropy and differences in isotropic velocity, since the regions sampled by equatorial and non-equatorial paths are not exactly similar. Hence a suitable approach is to build composite models combining the attenuation, velocity, and density contrasts across the ICB.

1.1.2.2.3 Attenuation

Compressional waves travelling through the core generally attenuates more in the solid inner core than in the liquid outer core. Additionally, a hemispherical difference is also observed for the attenuation of P waves travelling through the inner core. The top 85 km of quasi-eastern hemisphere is currently predicted to be nearly isotropic in terms of attenuation with an average higher attenuation while that of quasi-western hemisphere is predicted to be more anisotropic with average lower attenuation (Souriau and Romanowicz, 1996; Wen and Niu, 2002; Cao and Romanowicz, 2004b; Oreshin, 2004). While the quality factor Q (attenuation is given by Q^{-1}) obtained from PKIKP/PKiKP amplitude ratios vary in a range of 160 - 250 for QEH and 335 - 600 for QWH, the studies that modeled P wave attenuation in combination with P wave velocity found a similar hemispherical pattern for both parameters. Clearly such results hint at large scale differences in heat flow and/or compositional buoyancy near

the bottom of the outer core, leaving regionally different material properties on the inner core.

1.1.2.2.4 ICB Topography

The first suggestion of an inner core that is not smoothly spherical was in 1983 (Poupinet, Pillet and Souriau, 1983) where IC was assumed prolate in shape in order to explain PKIKP travel time delays with respect to Jeffreys-Bullen tables (Jeffreys and Bullen, 1958) for core phase travel times. The origins of these observations were then debated whether to be resulting from velocity anisotropy or radius anomalies. Currently it is assumed that solidification may be a dendritic growing outwards towards outer core (Bergman, 2003) or a snowing of crystallized iron from the outer core (Lasbleis, Hernlund and Labrosse, 2015). How different topography profiles may develop due to either iron precipitation or dendritic iron crystal growth, as temperature drops below liquidus is of current interest to geodynamic modelling. More on current seismological predictions for ICB topography are discussed in 1.2.1 under the topic of previous studies that motivated the main objective of this thesis.

1.1.2.2.5 Inner-inner core

A distinct innermost region of 300 km radius has been predicted due to its difference in anisotropy compared to the rest of the inner core (Ishii and Dziewoński, 2002, 2003; Niu and Chen, 2008). More recent studies interpret travel times observations of PKIKP/PKIIKP as resulting from an inner-inner core of 600 km radius with distinctly

different anisotropy (Wang, Song and Xia, 2015). The study described in this thesis focuses on the shallower inner core where solidification is more recently occurring and the existence of an inner inner core might signify a change in the mechanism of solidification in the past or possibly a solid-solid phase change in the lattice structure.

1.1.2.2.6 Super-rotation

The fact that the inner core rotates faster than the mantle, was predicted by early geodynamic models (Glatzmaier and Roberts, 1996) and was possibly affirmed by seismology in 1996 (Song and Richards, 1996a; Su, Dziewonski and Jeanloz, 1996). A nearly 0.3 s change in the PKPBC – PKPDF differential travel times recorded for the same ray paths over 30 years lead to a super-rotation rate in the order of 1^{o} per year. Travel time analysis considering small scale heterogeneities within the inner core and mantle (Creager, 1997; Song, 2000; Vidale, Dodge and Earle, 2000; Tkalčić *et al.*, 2013) narrows down the rate to 0.1^{o}-0.6^{o}. The super rotation rate had been a baseline assumption for some of the recent predictions regarding the elastic and topographic structure at the ICB (Cao, Masson and Romanowicz, 2007). On the other hand, models of a hemispherically different upper inner core (Waszek, Irving and Deuss, 2011; Cormier and Attanayake, 2013) support no or very slow (0.1^{o}-1^{o} per million years) super-rotation, based on the fact that inner core growth combined with its rotation would erase any signatures imposed by lateral variations in growth. The slow rotation rates are in fact supported by geodynamic predictions of IC being if it is gravitationally locked to the lower mantle by the density blobs created by topographic bumps on the CMB and ICB(Buffett and Creager, 1999).

1.1.3 Challenges in IC imaging

The sparse sampling of the IC by ray paths has been a major hurdle in better understanding the current structure of the IC. This has led to some regions in the southern hemisphere of IC un-sampled, as well as a lack of overlap in IC sampled by equatorial and non-equatorial ray paths, leaving uncertainty in an overall inner core structure. Nevertheless, better simulation methods, data processing methods to resolve wave phases that usually hide within noise and an increasing geographic distribution of seismic stations are paving the way to discover a fuller picture of the 3D nature of the IC. Another obstacle has been isolating the effects of core properties in core-sensitive seismic phases that are also perturbed by structures in Earth's mantle and crust. Most of the strong lower mantle effects can be canceled by using a 'reference' phase to which to compare amplitudes and travel times of inner core sensitive waves. For instance, the timing or amplitude of PKIKP that samples the uppermost 300 km of IC can be measured with respect to those of PKiKP that has a very similar ray path except that it turns back at the ICB instead of transmitting through it as PKIKP. A concern in this method is that such reference phases can be contaminated by near boundary heterogeneities.

In this thesis, I address the issue of refining the upper inner core structure, mainly the boundary roughness, along with its implications on other properties such as the density jump and observed attenuation of compressional waves. The following

sections 1.2 – 1.4 motivate the study by a related literature review, followed by a description of the objectives and organization of the thesis.

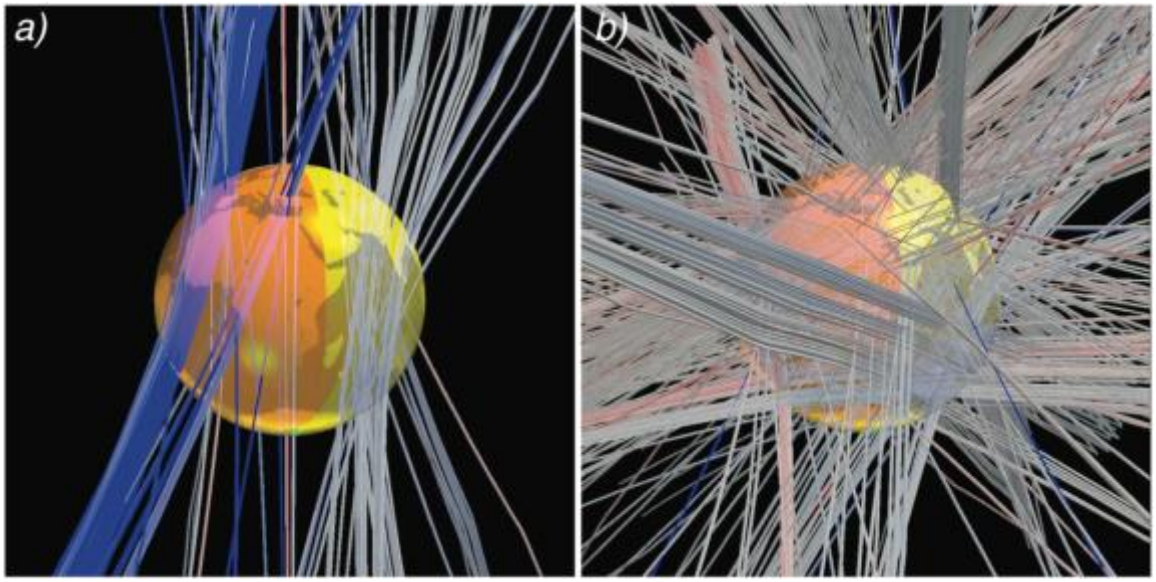

Figure 3: PKIKP raypaths traversing the IC of the Earth in 3-D from the existing data sets of PKPbc-PKIKP differential traveltimes by waveform correlation(Leykam, Tkalčić and Reading, 2010; Tkalčić, 2010). The IC is shown by the yellow-orange globe in the center. (a) Quasi-polar PKIKP raypaths, defined by an angle $\xi \leq 35^{\circ}$. Colors of raypaths correspond to different values of traveltime residuals, blue marking fast, white marking neutral, and red marking slow paths through the IC. Orange and yellow colors represent quasi western and quasi eastern hemispheres of the IC, defined by Tanaka and Hamaguchi [1997]. (b) Quasi-equatorial PKIKP ray paths, defined by an angle $\xi \geq 35^{\circ}$. Figure and caption from Tkalčić 2015.

1.2 Motivation

The inner core of Earth is continuously growing within a liquid iron outer core (Figure 4). Solidification of iron at the top of the inner core emits latent heat and lighter elements, driving thermal and compositional convection in the liquid core (Lister and Buffett, 1995; Gubbins *et al.*, 2003). The nature of this solidification hence has important implications on the behavior of Earth's geodynamo. Assuming a uniform growth rate of 1mm/year (Labrosse, Poirier and Le Mouël, 2001), the inner core might naturally be expected to have a radially smooth boundary. Many studies (Niu and Wen, 2001; Koper and Dombrovskaya, 2005; Krasnoshchekov, Kaazik and Ovtchinnikov, 2005; Cormier, 2009; Irving and Deuss, 2011; Attanayake, Cormier and De Silva, 2014), however, have revealed lateral variations of elastic structure near the inner core boundary, including variations in seismic velocity, attenuation, and anisotropy. This suggests that there may be significant lateral differences in both the mechanisms and rates of its solidification (Cormier, 2007; Deuss, Irving and Woodhouse, 2010; Cormier, Attanayake and He, 2011; Cormier and Attanayake, 2013) and melting. If the growth mechanism of the IC is in fact laterally variable it implies variations in heat extraction (Gubbins *et al.*, 2011) and convective currents (Aubert *et al.*, 2008) in the liquid outer core near the ICB, integral to the behavior of the geodynamo. Thus, mapping or characterizing the statistics of the scale lengths of ICB topography can aid in understanding the mechanisms of inner core solidification and melting, which may be linked to secular variations in Earth's magnetic field.

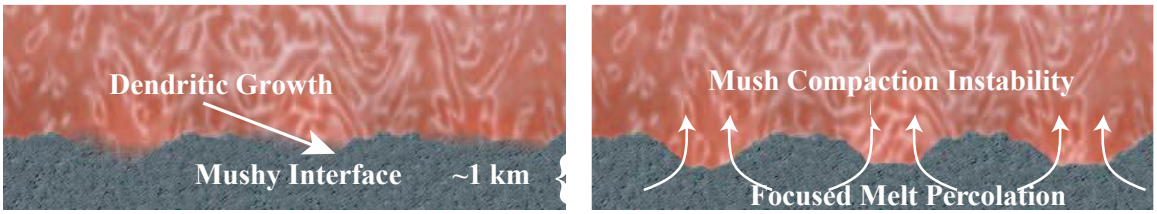

Figure 4: Possible mechanisms sustaining topography of the inner core boundary (John Hernlund, person. commun.)

1.2.1 Previous Studies of inner core boundary topography

A number of seismological observations suggest topographic features of various vertical and lateral scales from 0.01 to 10's of kilometers (Cao, Masson and Romanowicz, 2007; Dai, Wang and Wen, 2012; Tanaka and Tkalčić, 2015; Yao, Sun and Wen, 2015). The results of these studies rely on the comparison of observed travel times and amplitudes of the PKiKP waveform with those predicted from seismograms synthesized by numerical methods in models of ICB topography. Such simulations have variously suggested bumps as high as 14 km with 6 km lateral spread, sinusoidal variations with wavelengths and heights 1-1.5 km (Dai, Wang and Wen, 2012; Li, Sun and Helmberger, 2014; Tanaka and Tkalčić, 2015), and localized 0.98-1.75 km growth of inner core radius within 10 years (Wen, 2006; Yao, Sun and Wen, 2015). Such features would require small variations in temperature and composition near the top of inner core or even periodic variations of growth rates across its surface. Another observation has suggested a geographically fixed sinusoidal topography with wavelengths in the order of 10 km and heights less than 5

km (Cao, Masson and Romanowicz, 2007), based on estimates of an assumed rate of IC super rotation (Song and Richards, 1996b; Vidale, Dodge and Earle, 2000; Zhang, Richards and Schaff, 2008; Tkalčić *et al.*, 2013) of 0.1^{o} per year. Most of the previous work on ICB topography has concentrated on the PKiKP waveform observed at distance ranges where it is a small-amplitude, pre-critical reflection. Much less work exists on the effects of ICB topography through the full range of angles at which P waves are incident on the ICB, including the angles at which reflected, transmitted, and diffracted waves are observed at longer range (Figure 5). The mysterious 'm-phase' (Adam and Romanowicz, 2015), a pulse of energy appearing in the coda of PKiKP beyond the inner core shadow within 5-20 s after the main phase could possibly be due to scattering by ICB topography. Scattering caused by the roughness in ICB has been suggested to be a factor adding to attenuation (Zou, Koper and Cormier, 2008) of PKP_{Cdiff}, affecting its amplitude decay into the shadow of the inner core. The longer event-station distance ranges and high frequency band (> 1 Hz) where these observations have been made, pose special challenge to seismic waveform modeling, requiring the use of numerical methods that remain stable and accurate for 1000's of wavelengths of propagation.

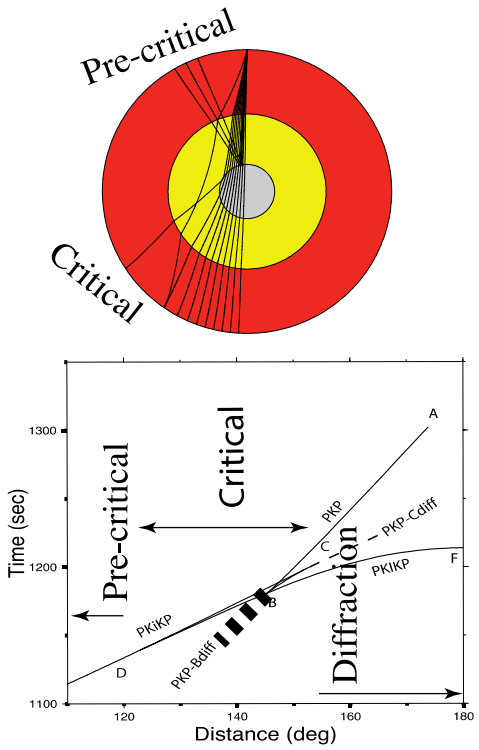

Figure 5: Rays and travel-time curve of P waves interacting with Earth's inner core.

Our study incorporates a boundary element method (BEM) that explicitly applies boundary conditions to efficiently simulate compressional waves reflected or diffracted around an ICB-like interface. The boundary element method grids only the topography associated with the boundary, making it possible to simulate just the effects of boundary topography without the need for large dense 2- or 3-D grids to overcome the grid dispersion in numerical finite difference and pseudospectral methods.

1.2.2 Density contrast

By recording the processes of gravitative differentiation of Earth and the solidification of its inner core, the density contrasts at the ICB and the CMB are important for understanding the thermal evolution of Earth's core. Better constraints on ICB topography can reduce the error bars of current estimates of the density jump across the ICB, especially whether or not the lower estimates ~0.2 – 0.5 gcm-3 (Koper and Pyle, 2004; Koper and Dombrovskaya, 2005) are artifacts of topographic scattering by a boundary with higher density jump. We know that other seismological studies set higher upper bounds such as 1.8 gcm-3 (Bolt, B. A., 1970),1.35-1.66 gcm-3 (Souriau and Souriau, 1989), 1.1-1.2 gcm-3 (Tkalčić, Kennett and Cormier, 2009), 0.64-1.0 gcm-3 (Shearer and Masters, 1990), and ~0.85 gcm-3 (Cao and Romanowicz, 2004a). It is proposed that regions with lower than average estimates of density jump (Tkalčić, Kennett and Cormier, 2009), could be caused by one or more reasons such as (1) PKiKP rays sampling a less solidified region on the inner core perhaps in a mosaic structure of laterally varying density jumps across the ICB (Krasnoshchekov, Kaazik and Ovtchinnikov, 2005); (2) PcP rays sampling a region of the CMB where the density contrast is higher than average (as per studies using PKiKP/PcP ratio),;(3) a variation in attenuation caused by upper IC texture (Cormier, 2007); (4) or attenuation of PKiKP due to ICB topography. We will systematically investigate the ability of topography in obscuring higher density contrasts at the ICB.

1.2.3 Importance of imaging ICB structure

The importance of core imaging is mainly connected to uncovering details of Earth's geodynamo. An explanation of the observed patterns of spatial and temporal variation of the geomagnetic field is still poorly understood. A prime obstacle has been the lack of knowledge regarding the mechanism driving the geodynamo, i.e. the convection of liquid in Earth's outer core. Specifically, examining the composition of outer and inner core together with the lateral growth variations at the ICB is crucial because compositional buoyancy initiated near the ICB is a key driving force of the geodynamo.

The geomagnetic field has gone through changes in intensity and reversals of its dipole component in the past according to paleo magnetic records. Currently a magnetic field intensity decrease rate of about 5% per century is observed, and it is uncertain whether the trend will continue leading to a dipole reversal in about 2000 years or whether it will begin to increase again. To exactly understand the temporal behavior of the magnetic field, it is necessary to know the fine details of outer core liquid convection that sustains the field. The dynamics of the inner core is directly related to the generation and maintenance of the Earth's magnetic field.

1.3 Objectives

Our main goal is to extend investigation of ICB topography to longer distance ranges, particularly to observe the effect on PKP_{Cdiff}. We will discuss the effect of topography on P wave reflections collected at a broad range of source-receiver distances, and also predict an upper bound to realistic heights of ICB topography. It is expected that the extent of ICB roughness would have tradeoffs with material properties such as seismic anisotropy, velocity, attenuation and density in perturbing compressional seismic waves that interact with the central core region.

In addition to the topography investigation, we introduce a structure more complex than a simple degree-one hemispherical model for the P wave attenuation pattern surrounding the growing boundary region of the IC. The end goal is to discuss the discoveries of above studies alongside similar literature and clarify the nature of inner core solidification, contributing to the groundwork of harnessing a better understanding of the Earth's convective geodynamo.

1.4 Organization

We start by presenting the methods used for the modeling of ICB topography (main study) and the cross-correlation methods used in attenuation modeling (secondary study). In section 2.1, first the BEM (Boundary Element Method) simulation is

validated for the pre-critical reflection of PKiKP by comparing our results to a pseudospectral simulation, and then a set of topographic structures are systematically tested for their influence on wave amplitude and travel time through the range at which P waves diffract around the ICB. Section 2.2 describes a procedure of inverting for the seismic attenuation structure in the lowermost outer core and uppermost inner core. Chapter 3 presents the results in detail.

The implications of the BEM simulation results and ICB topography estimates are discussed thoroughly in section 4.1. This discussion is extended in 4.2 – 4.3 by a conglomerate discussion of interpretations about the IC solidification with regard to our main and secondary studies. In chapter 5 we summarize the key findings and highlight the implications of suggested boundary heterogeneities. In chapter 6 we review avenues of continued research in understanding the inner core evolution.

Chapter II

Methods

This chapter discusses the analysis procedure and methodology used in the two studies of modeling ICB topography and attenuation in the inner core near the ICB. The first study develops a procedure to simulate the response of P waves to various types of ICB topography, incorporating a numerical method for wave propagation. The second study designs a procedure of cross-correlating synthetic waveforms with actual seismograms to invert for a suitable attenuation model in a region of the liquid outer core above the ICB (F-layer) and in the uppermost solid IC.

2.1 Modeling Topography

We use a boundary element method (BEM) to simulate the P wave field reflected off a rough inner core boundary. Since the problem in 2-D requires propagation of high frequency (0.5-1 Hz) waves over a range of 1000 or more wavelengths, finite difference methods are computationally expensive compared to boundary element methods where the discretization is limited only along the boundary of interest. BEM favors our purpose of modeling the effect of ICB surface geometry separate from the effect of volumetric heterogeneity within the inner core. At the outset, we caution that any topography on the ICB is likely to be also accompanied by volumetric heterogeneity. Volumetric heterogeneity in the inner core has been documented from the coda of pre-critical PKiKP (Leyton & Koper, 2007) and can be an additional important effect controlling the coda following PKiKP as well as the attenuation of PKIKP.

2.1.1 Numerical Simulations

The boundary element method, geared for probing interface properties, is based upon representing the displacement and traction wavefields propagated through a medium, in terms of boundary integral equations. We will utilize the direct boundary element method, which writes these equations using the displacement and traction fields near the interface. Equation 2.1 and 2.2 represent the displacement fields in two mediums across a boundary, where we refer to medium 1 as the internal domain that contains a set of body forces (f) and medium 2 as the external domain (Pointer, Liu, & Hudson, 1998; Sánchez-Sesma & Campillo, 1991).

$$cu_j^I(\xi,\omega) = \int_S \left[G_{ij}^I(x,\xi,\omega)t_i^I(x) - T_{ij}^I(x,\xi,\omega)u_i^I(x)\right]dS_x + \iint_A f_i(y,\omega)G_{ij}^I(y,\xi,\omega)\,dA_y$$

$$c = \begin{cases} 1\,; if\ \xi\ inside\ the\ boundary \\ 0\,; if\ \xi\ outside\ the\ boundary \\ 0.5\,; if\ \xi\ on\ the\ boundary \end{cases}$$

Equation (2.1)

$$c' u_j^E(\xi,\omega) = -\int_S \left[G_{ij}^E(x,\xi,\omega)t_i^E(x) - T_{ij}^E(x,\xi,\omega)u_i^E(x)\right]dS_x$$

$$c = \begin{cases} 1\,; if\ \xi\ outside\ the\ boundary \\ 0\,; if\ \xi\ inside\ the\ boundary \\ 0.5\,; if\ \xi\ on\ the\ boundary \end{cases}$$

Equation (2.2)

Here the two domains of interest are the liquid outer core and the solid inner core respectively. (See Appendix 1 for explained formulation of the boundary integral equation/matrix system). Hence the applicable boundary conditions will be the continuity of normal displacement, continuity of normal traction, and vanishing tangential traction. Applying these boundary conditions to every element on the discretized boundary will generate a system of linear equations in the order of the number of elements, which can be solved to give the reflected and refracted displacement fields near each boundary element. These fields are then propagated to any position of interest within their respective mediums using equations 2.1 and 2.2. We investigate the effect of inner core topography on the P wave segment within the outer core, by placing body force terms and receiver positions inside the outer core close to the core mantle boundary, while disregarding any reflections off the core-mantle boundary. We perform calculations in the frequency domain and obtain synthetic seismograms using a fast Fourier transform. This provides an opportunity to easily limit the signal frequency band, convolve various source-time functions, and perform single-frequency calculations.

2.1.2 Earth models

Boundary element formulations tend to generate fully populated matrices. This means that the storage requirements and computational time will grow according to the square of the problem size. To optimize memory requirements we perform an exhaustive study of topography parameters at the boundary of two homogeneous layers having the elastic constants and densities across the ICB as specified by PREM (Dziewonski & Anderson, 1981) and AK135 (Kennett, Engdahl, & Buland, 1995; Montagner & Kennett, 1996) (Figure 6). The measured slownesses of the synthetic waveforms at hypothetical receiver arrays placed in a homogeneous outer core are used to convert the receiver distances to distances appropriate for observations in a full vertically heterogeneous Earth having a solid crust and upper mantle, liquid outer core, and solid inner core.

An initial goal is to verify the method's accuracy at small epicentral distances, so that we can continue utilizing it to simulate P waves diffracted around the ICB (PKP_{Cdiff}) at longer ranges. We work with a 0.5 Hz source to agree with the frequency band of observed PKP_{Cdiff} waves (Adam & Romanowicz, 2015; Zou, Koper, & Cormier, 2008), but also conduct experiments in the 1Hz band at shorter pre-critical distances for comparison with alternate numerical gridded methods over full areas or volumes of 1-D realistic Earth models.

2.1.3 Source frequency and boundary element length

We utilize a Ricker wavelet pulse (figure 12) of a given central frequency (f_0) with uniform radiation at all directions as the source. Boundary element calculations are carried out in the frequency domain for the Fourier transformed Ricker wavelet with non-zero frequency components falling between $f_0/100$ and $3*f_0$. The contributions from frequencies outside this range are negligible in a Ricker pulse with central frequency f_0. At each frequency component the boundary is sampled by an element length of $\lambda_{min}/10$, where λ_{min} is the minimum signal wavelength sampling ICB, which we take as the shear wave velocity Vs on top of IC divided by frequency. With this criterion higher frequencies require finer sampling. We conduct the PKP_{Cdiff} simulations with a Ricker wavelet having f_0=0.5Hz, and PKiKP simulations at distances < 20^o with a Ricker wavelet having f_0=1Hz, since the frequency content of the latter observations requires a shorter boundary length to be accurately sampled.

2.1.4 Time window of simulations

The lowest calculated frequency of a discrete Fourier transformed signal is the inverse of the time window half-length. Hence keeping a shorter time window, sufficient to contain the main pulses along with some scattered coda, reduces the number of frequency components needed to compute the computationally expensive matrix inversions of BEM. For narrow angle reflections we consider a 25s window to represent

the reflected PKiKP-like pulse. For the diffraction range we consider a 50s window to represent the transmitted PKIKP pulse together with the diffracted PKP_{Cdiff}-like pulse. Fourier transforming a limited time window usually tends to fold later-arriving pulses into the considered time window. To avoid this issue we add a small imaginary frequency $\omega_i = 1.5\pi/40$ for PKiKP simulations and $\omega_i = 1.5\pi/3200$ for PKP_{Cdiff} simulations, depending on the travel times, to the radian frequency of the input signal before BEM calculation, and apply an exponential factor, $e^{\omega_i t}$, to the inverse Fourier-transformed signal in the time domain. This process attenuates lengthy coda energy and eliminates late-arrivals from wrapping into the time window that contains the main phase of interest.

2.1.5 Waveform corrections

Waveforms of 2D synthetics appropriate for 2-D line point sources are converted to the waveform appearance for 3-D point forces by multiplying by a factor of $\sqrt{\omega}e^{-i\pi/4}$ in the frequency domain where ω is radian frequency. This correction is obtained via conversion of Green's functions from 2-D to 3-D (Cerveny, 2001). To correct for effects of 3-D vs 2-D geometric spreading, the computed ratio of PKP_{Cdiff}/PKIKP amplitudes are multiplied by a factor of $\sqrt{\frac{P_{PKPCDiff}}{P_{PKIKP}}}$, where $P_{PKPCDiff}$ and P_{PKIKP} are the slownesses of waves reaching the receiver. The PKP_{Cdiff} -PKIKP differential travel times are taken with respect to a smooth ICB model with lowermost outer core (OC) velocity of PREM applied homogeneously to the exterior domain. To adjust for the actual PREM velocity gradient at the lowermost 200 km of OC, we applied the following correction to

differential travel time T_{diff}. Note that non-smooth ICB topography has been tested with AK135 velocity above ICB, which is nearly constant in the lowermost 200 km of OC.

$$T_{diff}^{corrected} = T_{diff}^{measured} - \left\{\left(T_{bc\_mid\_vp}^{200km} - T_{bc\_bottom\_vp}^{200km}\right) - \left(T_{df\_mid\_vp}^{200km} - T_{df\_bottom\_vp}^{200km}\right)\right\}$$

Here T^{200km} terms represent the full travel times within the first 200 km above ICB. Their subscripts represent the PKP ray phase (BC or DF) and whether Vp is used to calculate travel time is from the mid-point or bottom 200 km of the PREM outer core. This correction is applied to all differential travel times of PKP_{Cdiff}-PKIKP measured with respect to PREM.

2.1.6 Propagation to the surface

For computational efficiency, our BEM calculations record the wavefield at an array of receivers 1000 km above the ICB. To avoid the use of approximate Green's functions and the need for matrix inversions at multiple elastic discontinuities, we assume an inner core and a homogeneous core extending to the surface of the Earth. Thus, to compare with observations at the surface of a realistic vertically inhomogeneous Earth having and inner and outer core and mantle, we need to include the effects of propagation from our array of receivers near the ICB boundary to receivers placed at the surface. For pre-critical reflections, the ICB incident angle of simulated reflected rays is matched to the great circle distance (g.c.d.) of PKiKP with an equal incident angle on the ICB ($\theta_{inc} = \sin^{-1}\left(\frac{V_{oc}\times P}{R_{ICB}}\right)$, where p is the ray parameter in sec/radian of PKiKP at a given g.c.d. For a receiver at the distance at which the arriving P wave is tangent to the ICB , we assign the

g.c.d. corresponding to the distance of the ICB grazing ray at the point C (PKP-C distance) predicted by PREM or AK135. For receivers beyond the ICB grazing ray, we increment the PKP-C point g.c.d. (155.9^o in AK135 and 152.7^o in PREM) by adding the difference in angular distance measured from the center of the Earth to each receiver and to the receiver at the grazing ray distance.

2.1.7 Validation

To validate the accuracy of BEM for predicting the effects of ICB topography, we compare its simulations of ICB reflections (Figure 7) to pseudospectral simulations (Figure 8). The pseudospectral simulations used the code described in (Cormier, 2000), including the method of densifying the vertical grid spacing near elastic discontinuities described by (Furumura, Kennett, & Furumura, 1999) . At vertical and horizontal grid increments of 0.4 km near the ICB, we were able to reach a peak frequency of 0.25 Hz for a simulation of particle velocity before some grid dispersion (Figure 8) became visible. This made possible a qualitative comparison with the results of a BEM simulation at frequencies approaching 0.5 Hz. Computation times of both methods lasted less than a day with less than 100 processors. The results of both methods demonstrate that 10 km scale topography severely attenuates the first arriving PKiKP pulse and generates significant, time-extended, high frequency coda following the pulse. Compared to the pseudospectral synthetics, we do not see coda arriving beyond a 25 s time window in the BEM synthetics (Figure 7). This is because later-arriving scattered coda in the BEM synthetics have been removed by economizing the number of frequencies, and hence time samples, by the use of complex frequencies described in 2.1.2.

2.2 Modeling Attenuation

The intention here is to investigate an attenuation structure near ICB, that fits the observed PKIKP and PKiKP amplitudes. When a seismic wave propagates through a medium its energy is lost, hence the signal is attenuated, due to friction and viscosity which is referred to as "intrinsic attenuation" of the medium. Additionally, a signal propagating in a certain ray path may also loose energy due to scattering. Total "apparent attenuation" of seismic waves, caused by both intrinsic energy loss and scattering, are quantified by 1/Q (or Q^{-1}), which appears in the term $\exp(-\pi fT/Q)$ defining the exponential decay of a signal amplitude with time and frequency. The term Q is often referred to as the "quality factor". In this study, we are interested in the P wave attenuation (Qp^{-1}) which is a linear combination of Qk^{-1} and Qs^{-1} that are functions of bulk and shear moduli. However, in a liquid domain such as the outer core Qp^{-1} equals Qk^{-1}.

2.2.1 Data

A seismic data set with high signal-to-noise ratio PKIKP and PKiKP were assembled and processed in Attanayake et al, 2014 and Attanayake, 2012 for the distance range of 130^{o}-140^{o} corresponding to earthquakes of Richter magnitudes 5.5-7.0. The set of 326 seismograms were removed of instrument noise and broadband filtered at a dominant frequency of 0.5Hz. Removal of instrument response here is basically the spectral-domain application of a Transfer Function with poles and zeroes defined for the specific

recording instrument. Since seismometer response must be zero at zero or very low frequencies, we account for that by also applying a high pass filter (response 0 below 0.01 Hz and 1 above 0.02 Hz). These filtering is applied to particle velocity seismograms.

Seismograms of chosen event-station distance range that have event depths 80-700 km, contain PKIKP sampling the uppermost 80 km of the inner core (Figure 9). To conveniently study possible lateral variations of elastic properties that are more complex than a simple hemispherical structure, the data traces were divided into 8 bins according to the longitudinal location of the PKIKP ray bottoming point. Figure 10 shows the bottoming points of ray paths within the inner core for PKIKP, as well as data distribution in each bin.

In order to remove earthquake source complexities, waveforms were deconvolved of the effective source time functions (ESTFs) (Li & Cormier, 2002) in the frequency domain. ESTF is an empirical measurement of the far-field earthquake source-time functions obtained via inverting P waveforms collected in the 30^{o}-90^{o} distance range from an event.

2.2.2 Modeling

The first part of Attanayake et al., 2014 identifies best fitting velocities and velocity gradients within the considered 8 bins for uppermost 80 km of IC and lowermost 200 km of OC, by perturbing standard Earth models' values until their resultant PKIKP-PKiKP travel time differences best fits the data. This velocity model is used along with variable Qp in the F-Layer region and IC, in generating synthetic PKIKP and PKiKP using the

existing Reflectivity algorithm (Kennet, 1988). Waveforms were generated using a delta source function filtered between 0.01-1Hz, for a range of Qp values in the IC and Qk values in the F-Layer. These synthetics were cross correlated with data waveforms to find the Q-factors that produce highest average cross correlation coefficient in each bin. PKIKP and PKiKP waveforms were bracketed in an 8s time window in order to avoid contributions of noise or other scattered arrivals into the cross-correlation coefficient.

Altogether 60 attenuation models were tested against the data in each bin. Qp in inner core was allowed to vary in the range 100-1000, while Qk in F-layer was assigned three possible values 57822 (Dziewonski & Anderson, 1981),1000 (Wookey & Helffrich, 2008),300 (Zou et al., 2008) suggested by earlier studies.

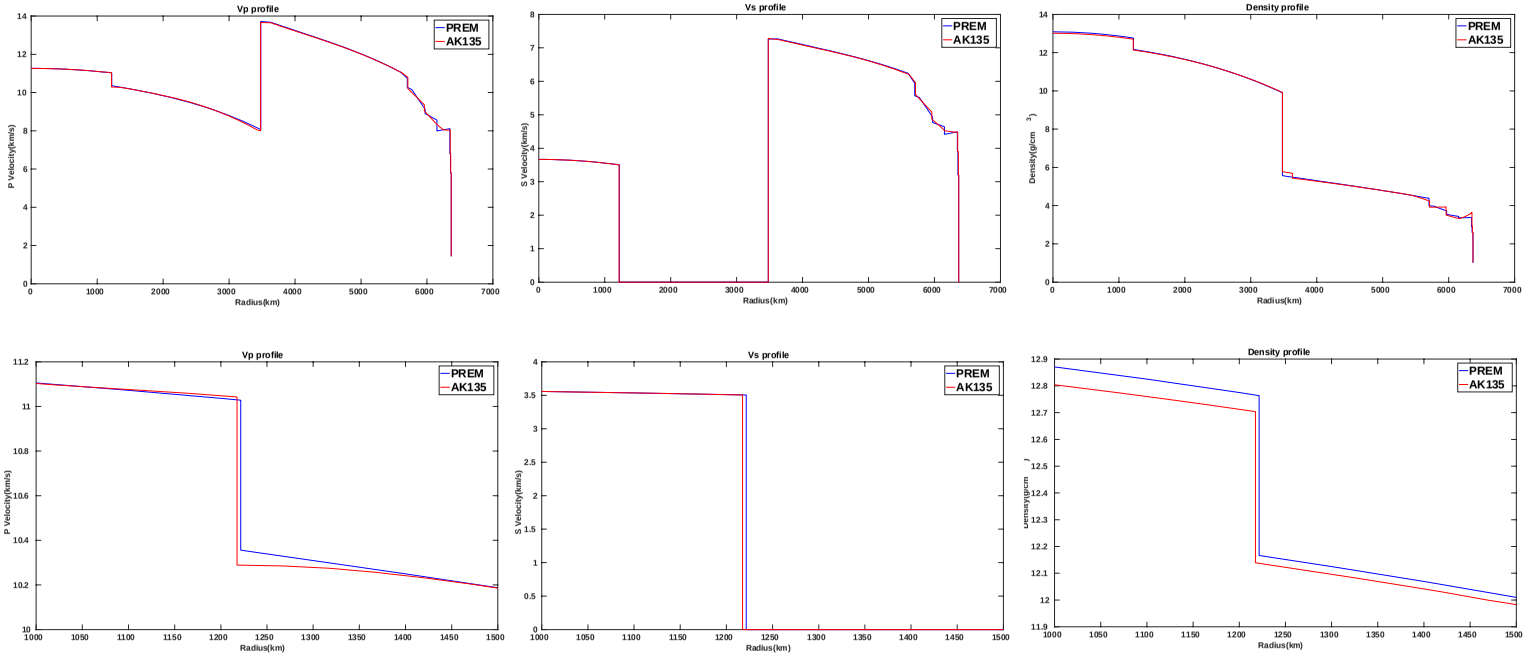

Figure 6: Seismic velocities and densities for the 1D models PREM and AK135 of whole Earth (above) and near the ICB (below).

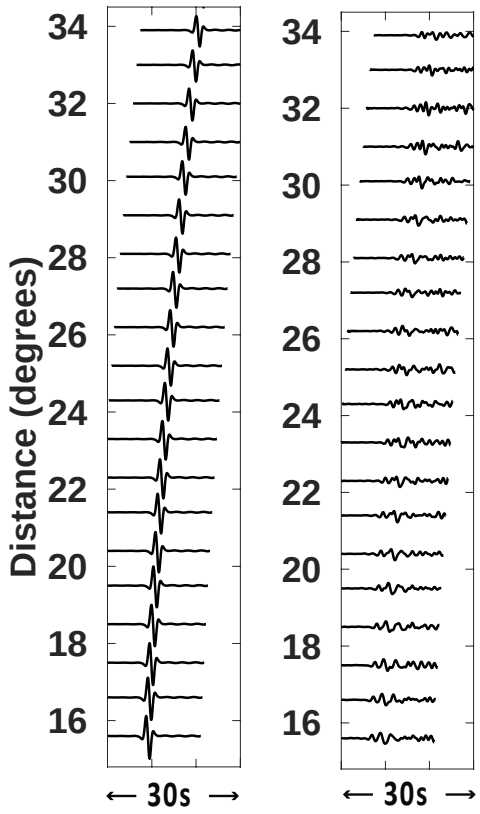

Figure 7: BEM simulations of pre-critical PKiKP using a Ricker wavelet with central frequency 0.5 Hz reflected from a PREM ICB with the source and receivers placed 1000 km above the boundary. Left: smooth boundary. Right: boundary with sinusoidal topography having peak-to-peak height of

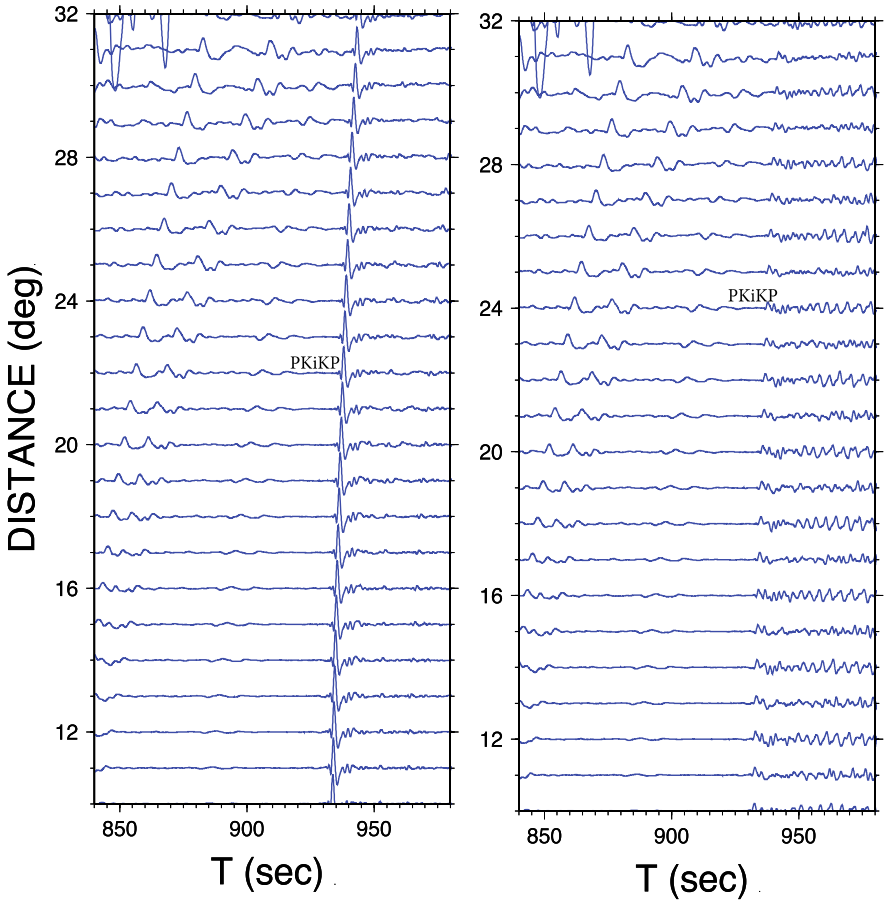

Figure 8: Pseudospectral simulations of particle velocity in PREM for PKiKP using a Gaussian displacement pulse for an explosive source. Left: smooth boundary. Right: boundary with sinusoidal topography having peak-to-peak height of 10 km and wavelength 20 km.

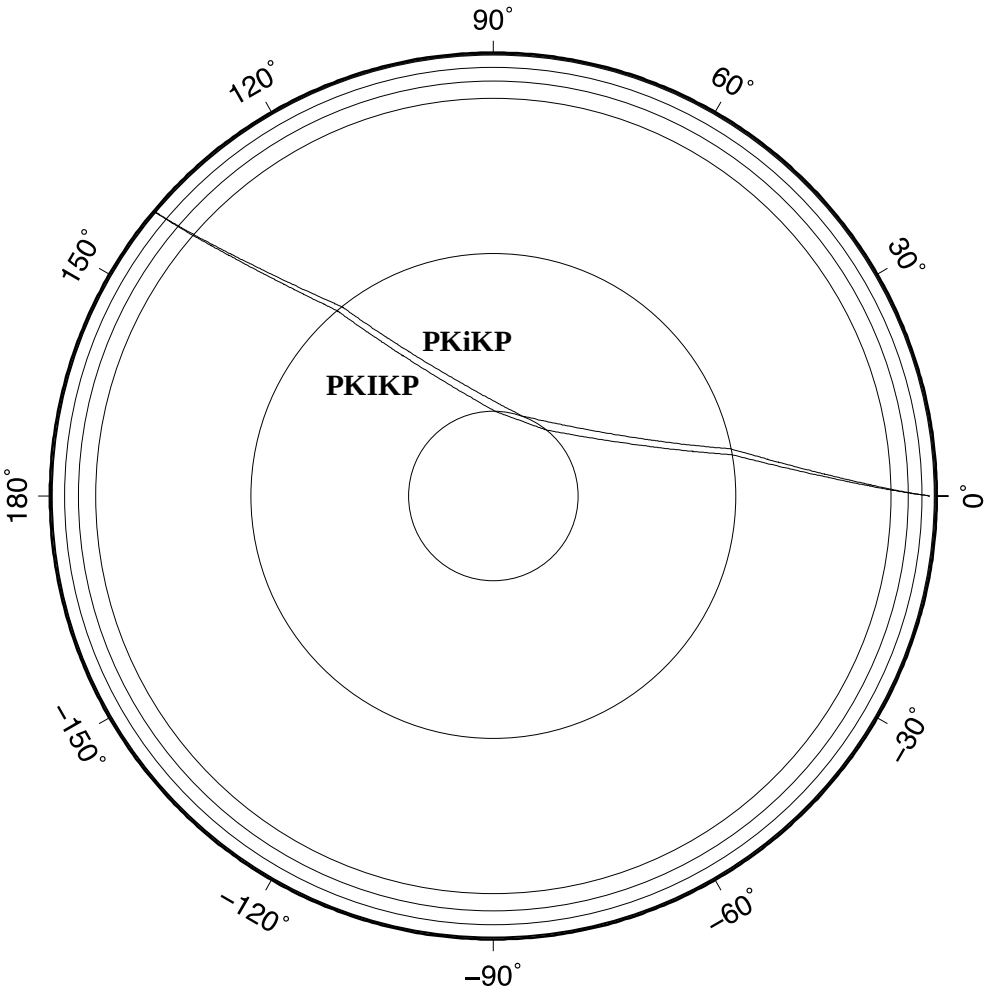

Figure 9: Paths of PKIKP and PKiKP rays received 140^{o} from an event of depth 100 km, in the 1D layer model AK135, plotted with TauP tool kit (Crotwell, Owens, & Ritsema, 1999). PKiKP reflects from ICB while PKIKP samples upto about 70 km below ICB.

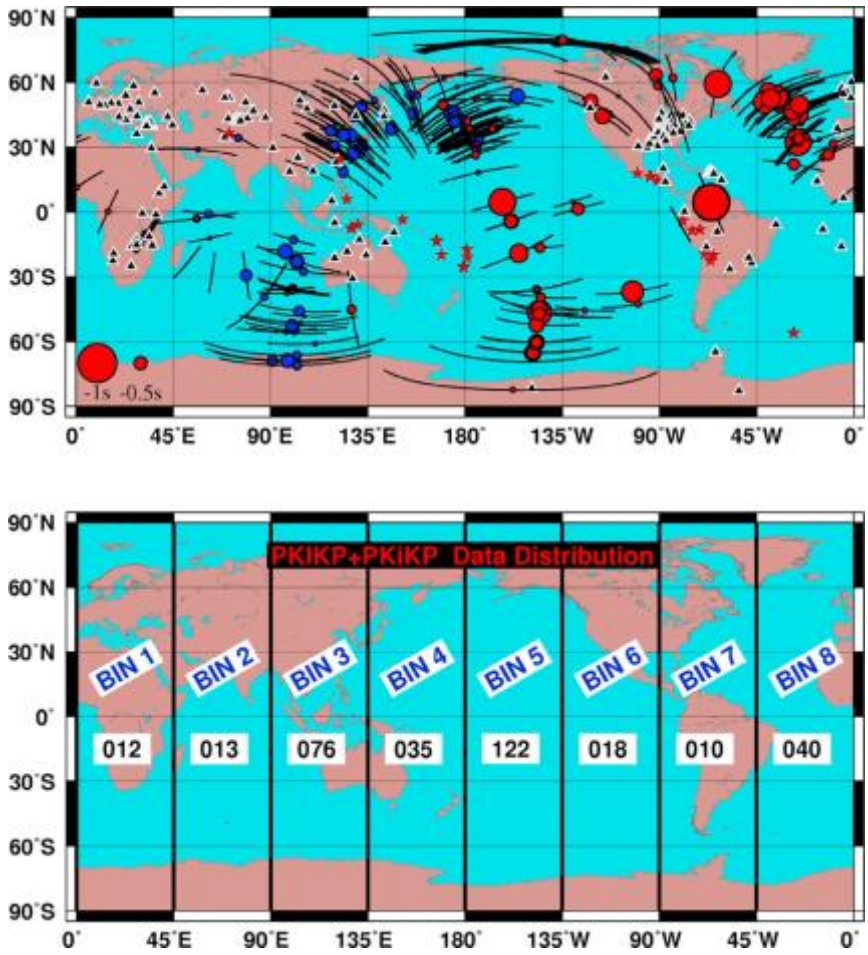

Figure 10: (a) Ray coverage and differential travel time residuals with respect to AK135-F model. Black heavy line segments show PKIKP ray leg in the inner core projected on to the Earth's surface and the circles whose radii are proportional to the time residual are centered at the ray bottoming point. Blue and red circles show positive and negative residuals respectively. Earthquakes (stars) and stations (triangles) are also shown. (b) Bin configuration and the number of data points in each bin. (Figure and caption from Attanayake et al., 2014)

Chapter III

Analysis of Results

3.1 ICB Models

We use BEM to simulate the effects on PKiKP waveforms induced by simple sinusoidal and randomly shaped topography (Figure 11). The randomly shaped, or *fractal-type* topography that contain bands of wavelengths, may more realistically model the ICB shapes resulting from dendritic freezing. Unlike the majority of previous studies of PKiKP topography, which have concentrated on the pre-critical incidence range of PKiKP, we perform simulations from the pre-critical through diffracted range.

3.1.1 Pre-critical PKiKP 0^{o} to 30^{o}

As shown in sub-section 2.1.3, ICB topography as high as 10 km scale with 10-20 km wavelength generates a complex PKiKP waveform with a time-extended coda equal in amplitude to the first several cycles of PKiKP, inconsistent with observations, e.g.,

(Figure 13). Although any peak topography height less than 5 km at 10-20 km wavelength is consistent with the observed coda of pre-critical PKiKP, an even lower upper-bound of perhaps 1 to 2 km is suggested by observations between 0^o to 20^o range, e.g., (Tkalčić, Kennett, & Cormier, 2009), which closely match the amplitudes predicted of the smooth ICB of standard Earth models. Topography higher than 3.5 km in this wavelength band begins to have significant effects on the amplitude of very short-range pre-critical PKiKP (Figure 14).

3.1.2 Pre-critical PKiKP 60^o to 100^o

In standard Earth models the ICB P reflection coefficient exhibits minima or zeroes for infinite frequency waves between 60^o to 100^o range (Figure 15). For our 0.5 Hz wave simulations, we find that ICB topography smooths over the amplitude variations predicted by standard Earth models. This effect is observable for 10 km wavelength topography with heights as small as 1 km.

Typical seismic observations used to estimate ICB properties, however, are at higher dominant frequency (1.5 Hz). To roughly extrapolate the effects of topographies calculated at lower frequencies to higher frequencies, one can assume that the effects scale according to the ratio of the signal wavelength and size a of a ICB bump. This is equivalent to the common observation that magnitude of scattering effects scale as the product of the wavenumber k and scatterer size a. For example, at 0.5 Hz. the effects for 10 km high topography at 10 km wavelength can be expected to be equivalent to that at 1.5 Hz for 3 km topography at 3 km wavelength. From this assumption and our modeling

results at 0.5 Hz, we can reexamine the important longer pre-critical PKiKP amplitudes reported by Kranoshchekov et al. (Krasnoshchekov, Kaazik, & Ovtchinnikov, 2005) from Soviet nuclear test sources of known or well-estimated yield. Their 1.5 Hz PKiKP amplitudes, plotted in Figure 15 agree with the effects of ICB topography of 3 to 5 km height at 0.5 Hz. Thus, we estimate that their observations can be explained by topography having heights on the order of 1 to 2 km. If verified by further observations, this shows that it is not necessary to require either a mosaic of inner core impedance contrasts as suggested by Kranoscheskov et al. or a zone of rigidity in the lowermost outer core (Cormier, 2009) to explain observations of pulse-like PKiKP in this longer pre-critical range. Topography having heights on the order of 1 to 2 km and wavelengths on the order of 1 to 10 km is sufficient to explain these observations.

3.1.3 Post-critical PKiKP 130º to 140º

Simulations for a wavelet of 0.5 Hz central frequency predict weak effects from ICB topography on PKIKP and PKiKP observed at 130º-140º (Figure 16). A lack of sensitivity to ICB for P waves at similar post-critical distances has also been predicted by Li et al. (Li, Sun, & Helmberger, 2014). A previous study by Cao at al. (Cao, Masson, & Romanowicz, 2007) predicts an ICB topography wavelength of 10 km with an upper bound height of 5 km to explain a large amplitude variation (a factor of 1.5 for PKIKP and a factor of 7.2 for PKIKP) observed in an earthquake doublet at 137.8º. The minimal amplitude effects seen in our simulation with the sinusoidal topography of wavelength 20 km and height 10 km at 0.5 Hz, is expected to be similar for a sinusoidal topography of wavelength 5-10 km and height 2.5-5 km at 1-2 Hz. Perhaps another mechanism in

concert with differential rotation of the IC, such scattering by volumetric IC heterogeneities (Leyton & Koper, 2007), can explain the large amplitude variations in PKiKP noted in their doublet observation.

3.1.4 PKP_{Cdiff}

For the simulations of diffracting P-waves a Ricker wavelet source (Figure 12) is placed 1000 km above the ICB. Then diffracted waveforms are collected by receivers 1000 km above the ICB on the ray paths of PKP_{Cdiff} corresponding to epicentral distances 155.9° - 161° which is beyond the PKP-C point for PREM (Dziewonski & Anderson, 1981) as well as AK135 (Kennett, Engdahl, & Buland, 1995; Montagner & Kennett, 1996) Earth models. In each case, we assign the material properties (velocity, density, Q) on either side of the ICB from a standard earth model for the exterior and interior of the two-layer model, along with boundary topography. With this configuration, we do not consider other anomalies that affect the appearance of PKIKP and PKP_{Cdiff} in seismograms such as IC volumetric heterogeneities, CMB topography, and crust-mantle heterogeneities. The contribution of all of these scattered or signal-generated noise effects, however, tend to hide the PKP_{Cdiff} signal beyond 160° (Figure 17).

3.1.4.1 Error bars

Some numerical noise still exists in the BEM simulations, largely due to loss of precision in the inversion of large matrices required by the method. In measuring amplitudes and amplitude ratios, we quantify the effect of this noise by taking the

average envelope of noise preceding or following pulses of interest in a 8s time window from the smooth boundary simulation. Figure 18 shows how the noise in the trace before the arrival is considered for the error of PKIKP amplitude and that after the arrival is considered for the error of PKP_{Cdiff}.

3.1.4.2 PKP_{Cdiff} and PKIKP amplitude ratios

The effects of either sinusoidal or fractal type topography of 10 km wavelengths with peak-to-peak heights as large as 5 km are quite insignificant (Figure 19, Figure 20) in signals having a dominant frequency of 0.5 Hz. At 10 km height, however, the effect of topography on PKP_{Cdiff} increases dramatically. The significant up/down shifts of PKIKP amplitude caused by the latter boundary type would in part be due to the amount of low Q inner core material sampled by the transmitted ray being different depending on its incident point ICB. The amplitude of PKP_{Cdiff} is expected to be governed by a combination of the upper IC length sampled by the grazing rays and the scattering caused due to tilt of the boundary.

It is seen that the natural log of PKP_{Cdiff}/PKIKP ratio obtained from our experiments do not strongly change for ICB topographic heights up to 5 km (Figure 22). One type of structure that would explain the scatter in PKP_{Cdiff}/PKIKP amplitude ratios observed by Zou et al. (Zou, Koper, & Cormier, 2008) is a sinusoidal ICB topography with wavelength and peak-to-peak height equal to 10 km, but topography of this scale does not agree with the evidence from PKiKP at pre-critical distances. We also note that the numerical simulations using the near-ICB parameters (velocity, attenuation, density)

of AK135 better fit both observed amplitude and travel-time data set than those of the ICB parameters of PREM (Figure 21).

The differential travel time of PKP_{Cdiff} - PKIKP of each simulation is calculated with respect to the simulation of a smooth boundary with PREM parameters. A correction is applied to the differential travel time measured directly from the simulated waveforms, in order to account for the lower outer core velocity gradient in PREM (see 2.1.2).

We find, in agreement with Zou et al. that the travel time data fits our smooth boundary AK135 simulation better than the smooth boundary PREM simulation. Similar to the amplitudes, the differential travel times resulting from topographies up to a height of 5 km are not sufficient to explain the distribution of observed data. Sinusoidal or fractal topographies of wavelengths and heights in the order of 10 km result in a larger variation of differential times but do not match the full extent of scatter observed in data (Figure 23).

3.2 Attenuation Models in Top IC and Bottom OC

Note that the velocity model at the top 80 km of IC is fixed as a fast QEH (between longitudes ~40E – 180E) and a slow QWH (between longitudes ~180WE – 40E) with respect to AK135, according to the prediction in the first part of Attanayake et al., 2014. Columns 3,5, and 7 of Table 1 shows the inner core Q that best correlates with data in each bin, when used in combination with each F-layer Q model of interest (columns 2,5, and 8). Out of this best fitting result set, the Q_{IC} - $Q_{F\text{-}layer}$ combination is chosen to

represent the final attenuation model. The 7 s windows containing best-correlated PKIKP-PKiKP synthetic and data waveforms are illustrated in figure 24. A good transition is observed in the lateral variation of attenuation ranging from Q^{-1} = 0.001 - 0.0067. F-layer attenuation is persistently lower (< 0.001) in majority of the areas.

An interesting observation of the attenuation pattern is that the average attenuation is high in QEH (bins 2-4) and also in bins 5 & 6 that is part of classic QWH. Many studies have confirmed that average velocity is high in QEH and low in QWH. Our results indicate that considering P wave attenuation and velocity together would divide the top layer of inner core into three regions; a low velocity – low attenuation region (90^{o}W-45^{o}E), a high velocity – high attenuation region (45^{o}E-180^{o}E), and a low velocity – high attenuation region (180^{o}W-90^{o}W) (figure 25). For the 200 km above ICB, i.e. F-Layer, a Q^{-1} of 0.001 which is higher than PREM appears generally better although the cross-correlation coefficients resulting from an F-layer attenuation of 0.001 and that of PREM (0.000017) is less than 2% from each other.

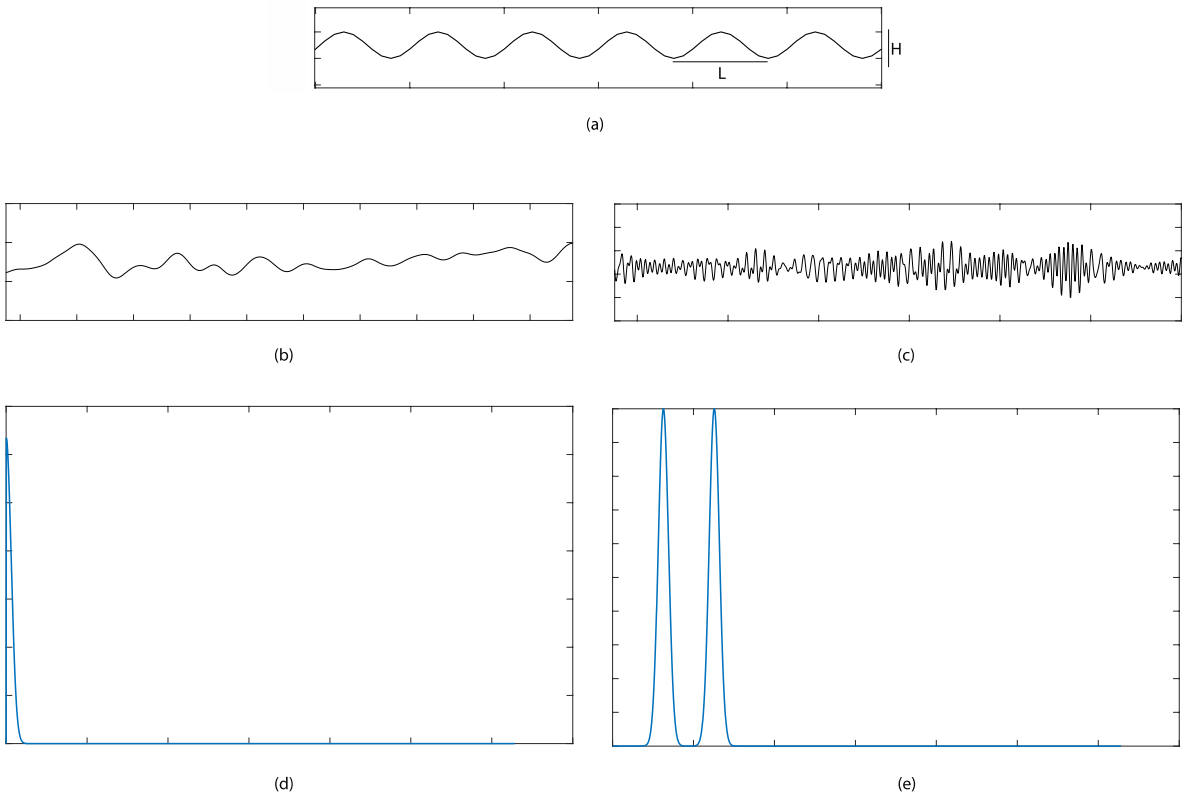

Figure 11: (a) sine topography shape, (b) fractal shaped topography with broadband wavelengths higher than 10 km, (c)) fractal shaped topography with broadband wavelengths centered near 10 km and 20 km. Wavelength bands for (b) and (c) are illustrated in the wavenumber spectra in (d) and (e).

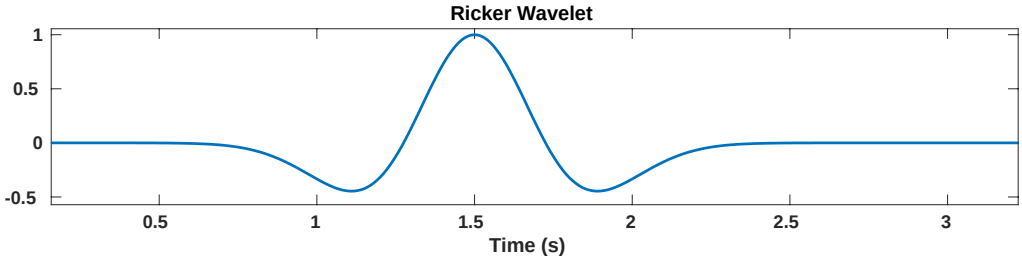

Figure 12: Ricker wavelet shaped source time function used in BEM simulations.

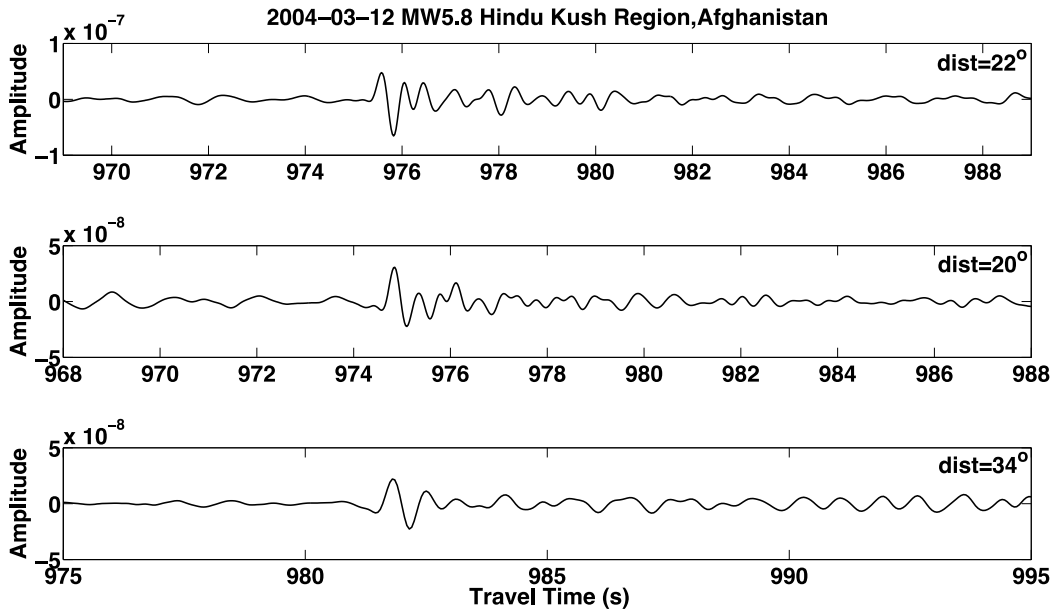

Figure 13: PKiKP waveforms from vertical component of velocity seismograms collected at pre-critical distances filtered between 0.7 to 3 Hz. Network-Station codes are XE-ES21, XE-ES36, and XG-ELSH starting from top seismogram.

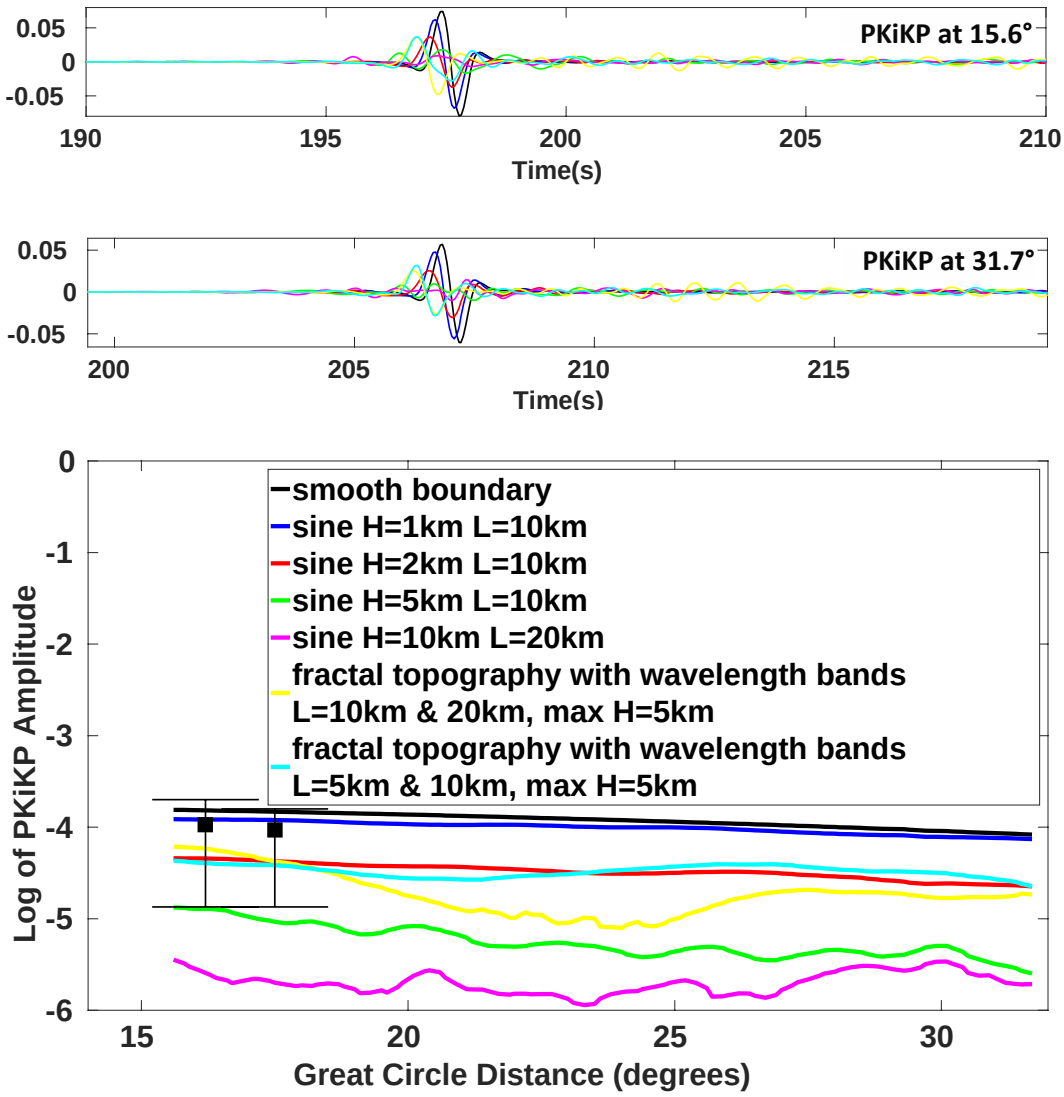

Figure 14: Simulated boundary reflections (1 Hz) particle velocity as seen 1000 km above the ICB for various assumed ICB topography. For each sinusoidal topography results are averaged over 5 initial phases between 0 and 2 π, and for each fractal topography results are averages over 5 different realizations. Top and Middle: waveforms for 15.6^o and 31.7^o respectively. Bottom: comparison of PKiKP amplitudes resulting from different topogra- phies for a range of pre-critical distances. Black data points with error bars show PKiKP amplitudes from Tkal˘ci`c et al.,2009 PKiKP/PcP ratios corrected for PcP amplitude and normalized with respect to PKiKP amplitude of a PREM smooth ICB.

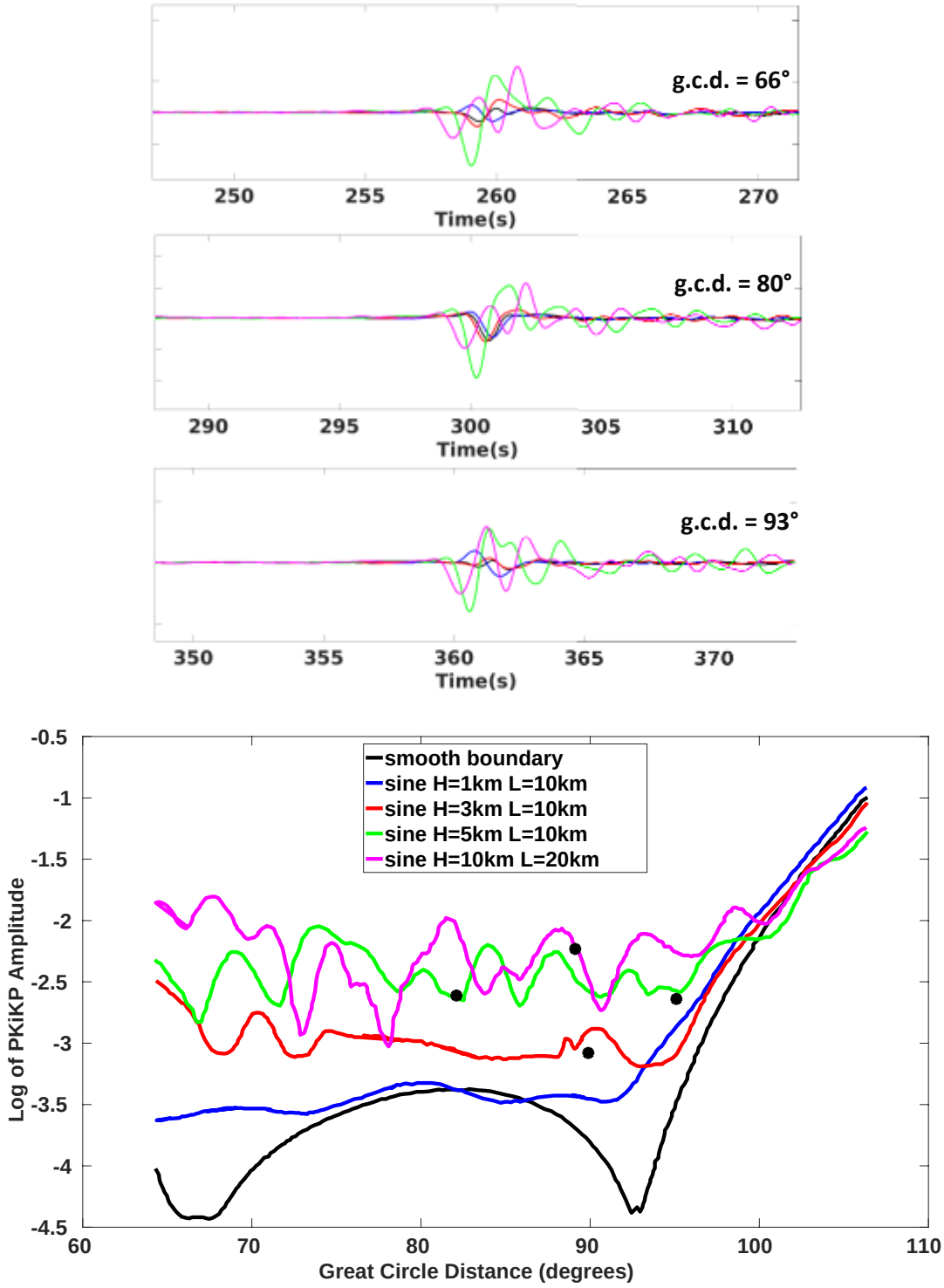

Figure 15: Bottom: Comparison of PKiKP amplitudes resulting from different topographies for the range of pre-critical distances where reflection coefficient reaches minima in standard Earth models. Black data points are PKiKP measurements from Kranoscheskov et. al [5] normalized with respect to the PKiKP amplitude of PREM smooth ICB at 82º. Above: Synthetic waveforms for 66º, 80º and 93º respectively.

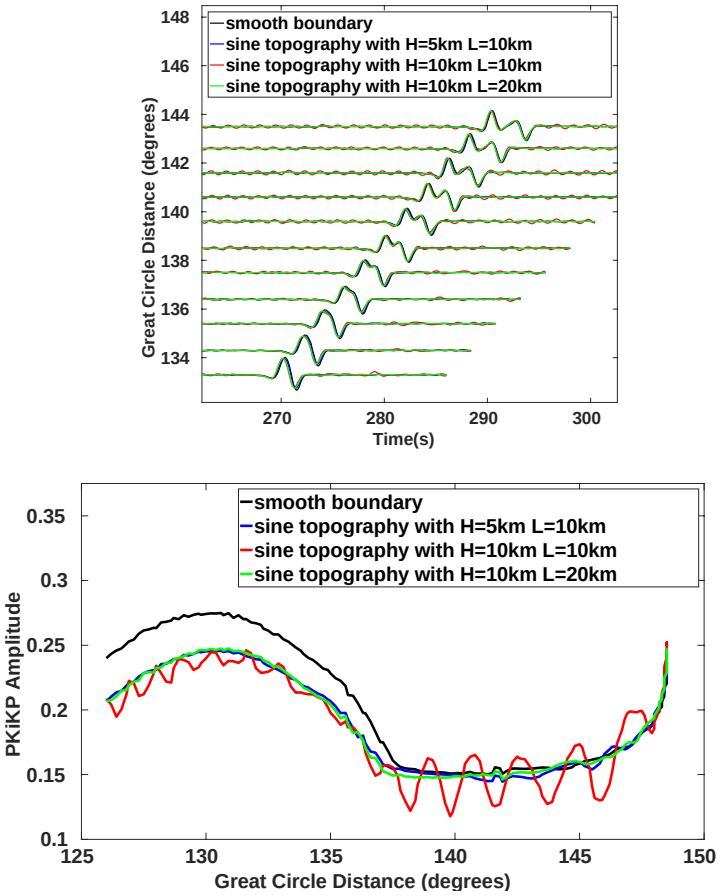

Figure 16: Above: Simulated waveforms of boundary reflections/refractions (0.5Hz) for rays incident on the ICB-like interface at post-critical angles. The separation of refracted (PKIKP-like) and reflected (PKiKP-like) phases begins around 133^o for the tested low frequency signal. Below: Amplitude variation with distance for post-critical reflections.

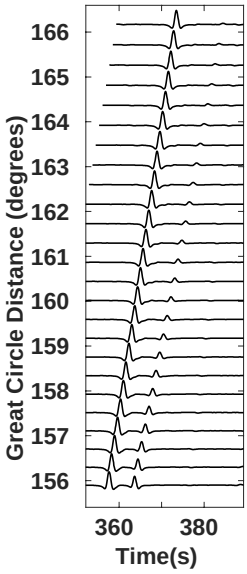

Figure 17: Waveforms of PKIKP and PKP_{Cdiff} computed from BEM with a 0.5 Hz. Ricker wavelet source and receivers placed 1000 km above the ICB for assumed AK135 ICB model parameters.

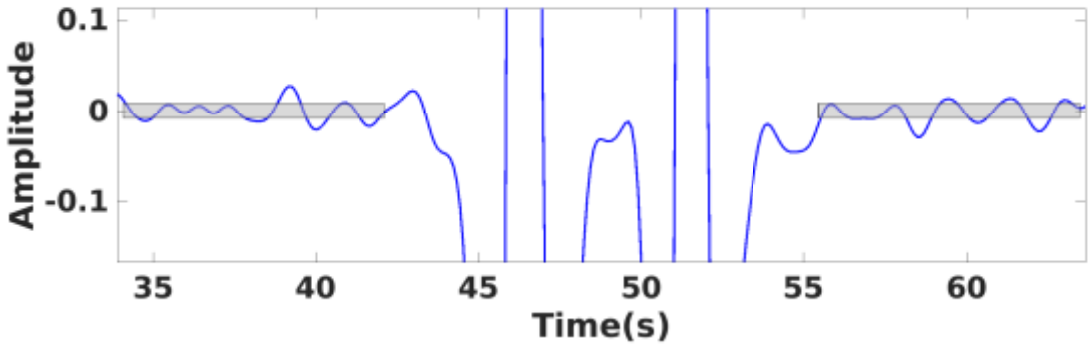

Figure 18: Shadowed regions represent +/- the estimated error in amplitude of the main pulse nearest them. Each window starts 4s from the peak of the main pulse.

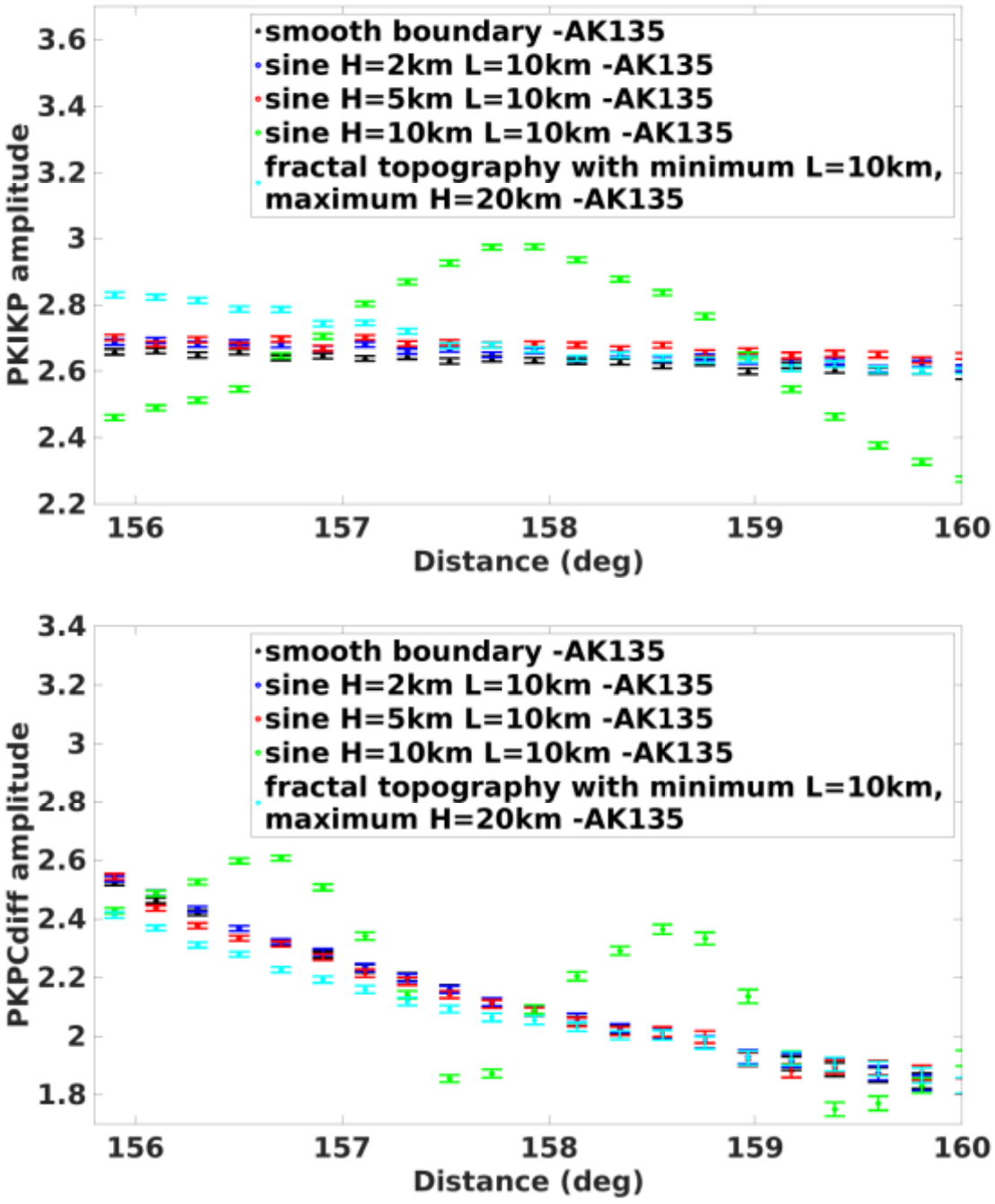

Figure 19: Amplitudes measured from BEM synthesized PKIKP (top) and PKP_{Cdiff} bottom) for different ICB models.

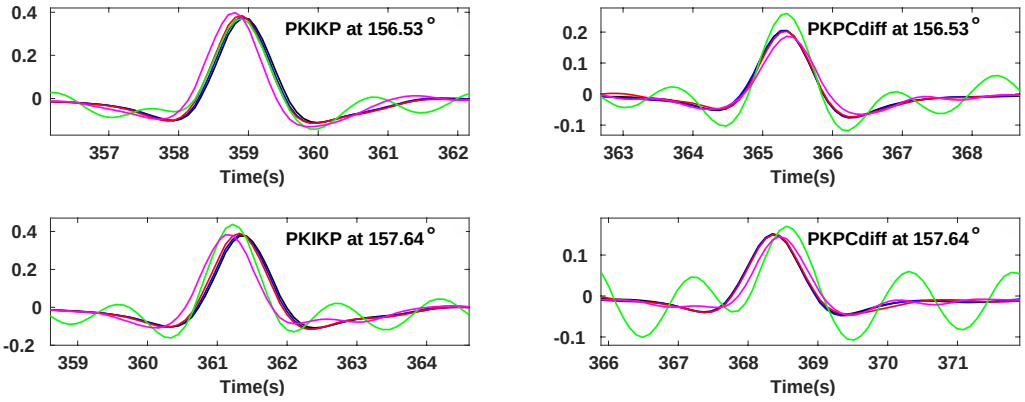

Figure 20: Synthesized PKIKP (left) and PKP$_{Cdiff}$ (right) waveforms for different ICB models at two distances. Colored waveforms are obtained with a smooth boundary (black), a sinusoidal boundary of H = 2 km and λ = 10 km (blue), a sinusoidal boundary of H = 5 km and λ=10 km (red), and a sinusoidal boundary of H = 10 km and λ=10 km (green), and a fractal boundary of maximum H=20 km and minimum λ =10 km (magenta).

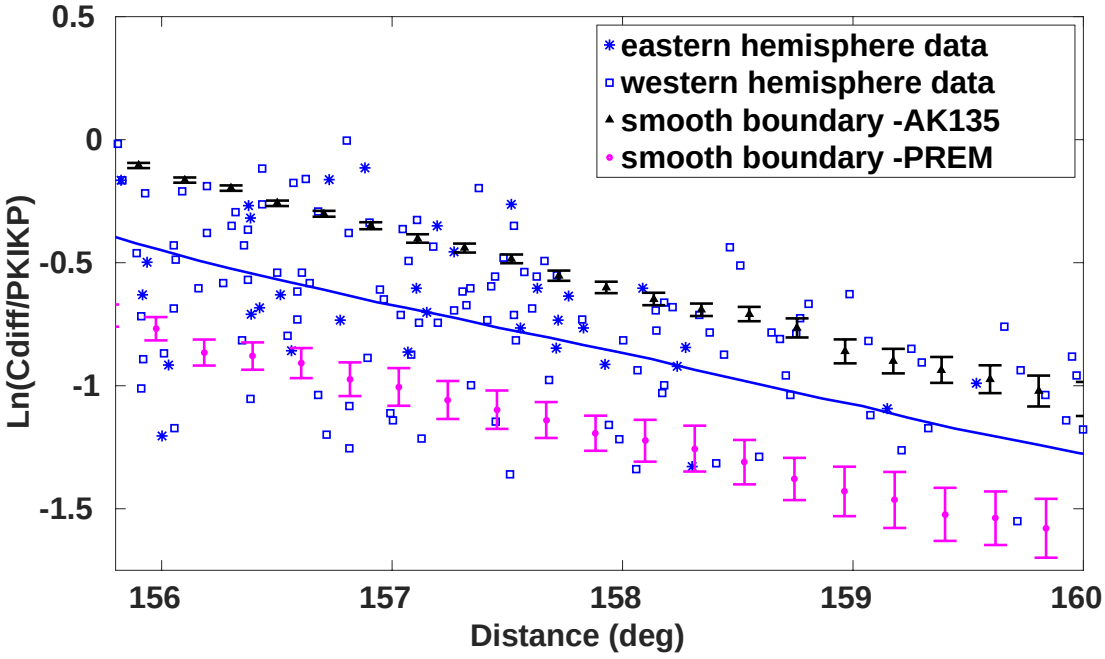

Figure 21: Simulated PKP$_{Cdiff}$/PKIKP amplitude ratios for AK135 and PREM for a smooth ICB compared to measurements byf Zou et al. [27]. Solid blue line is the least-squares best fit line to the observed amplitude ratio.

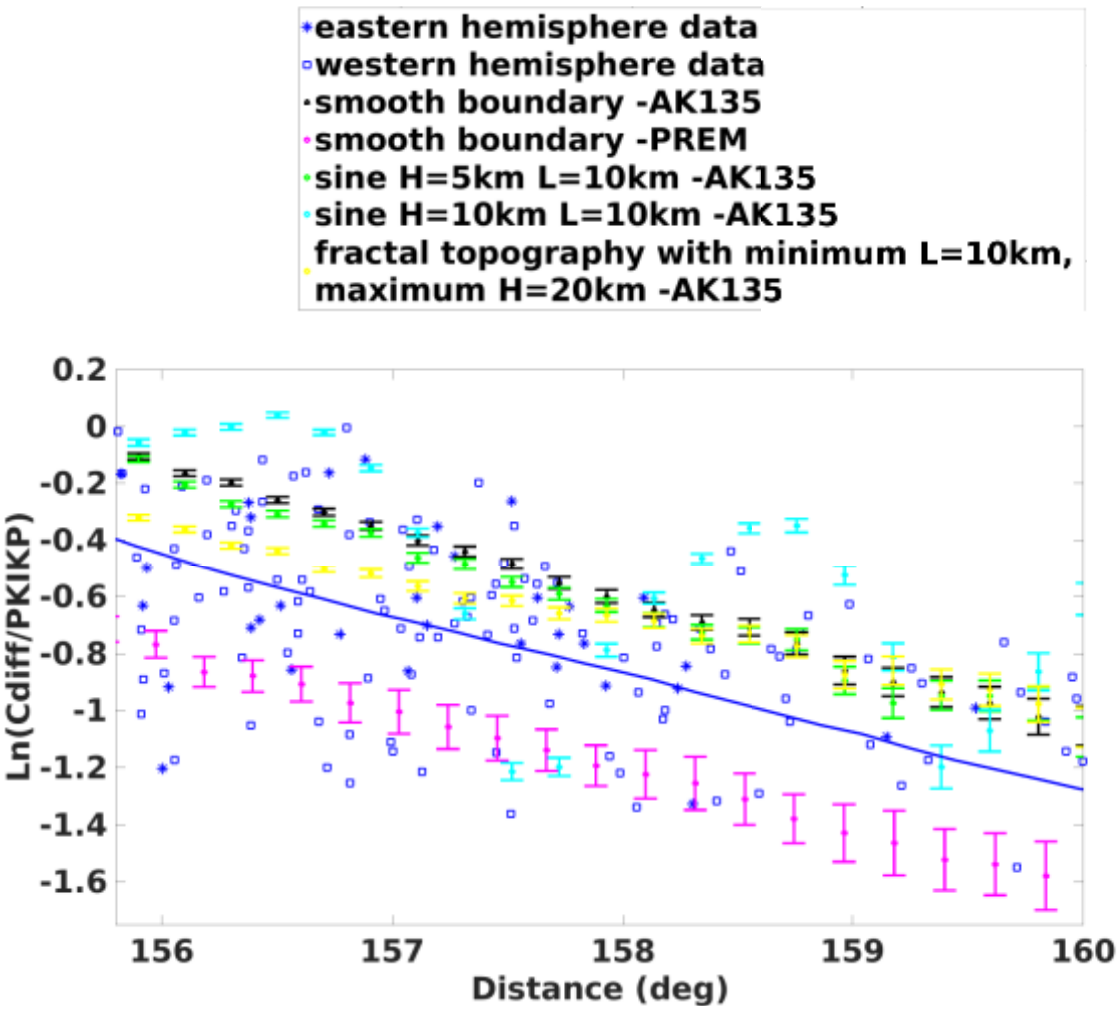

Figure 22: Simulated PKP_{Cdiff}/PKIKP amplitude ratios for models of ICB topography models compared to measurements by Zou et al. [27]. Solid blue line is the least-squares linear fit line to the observed amplitude ratios.

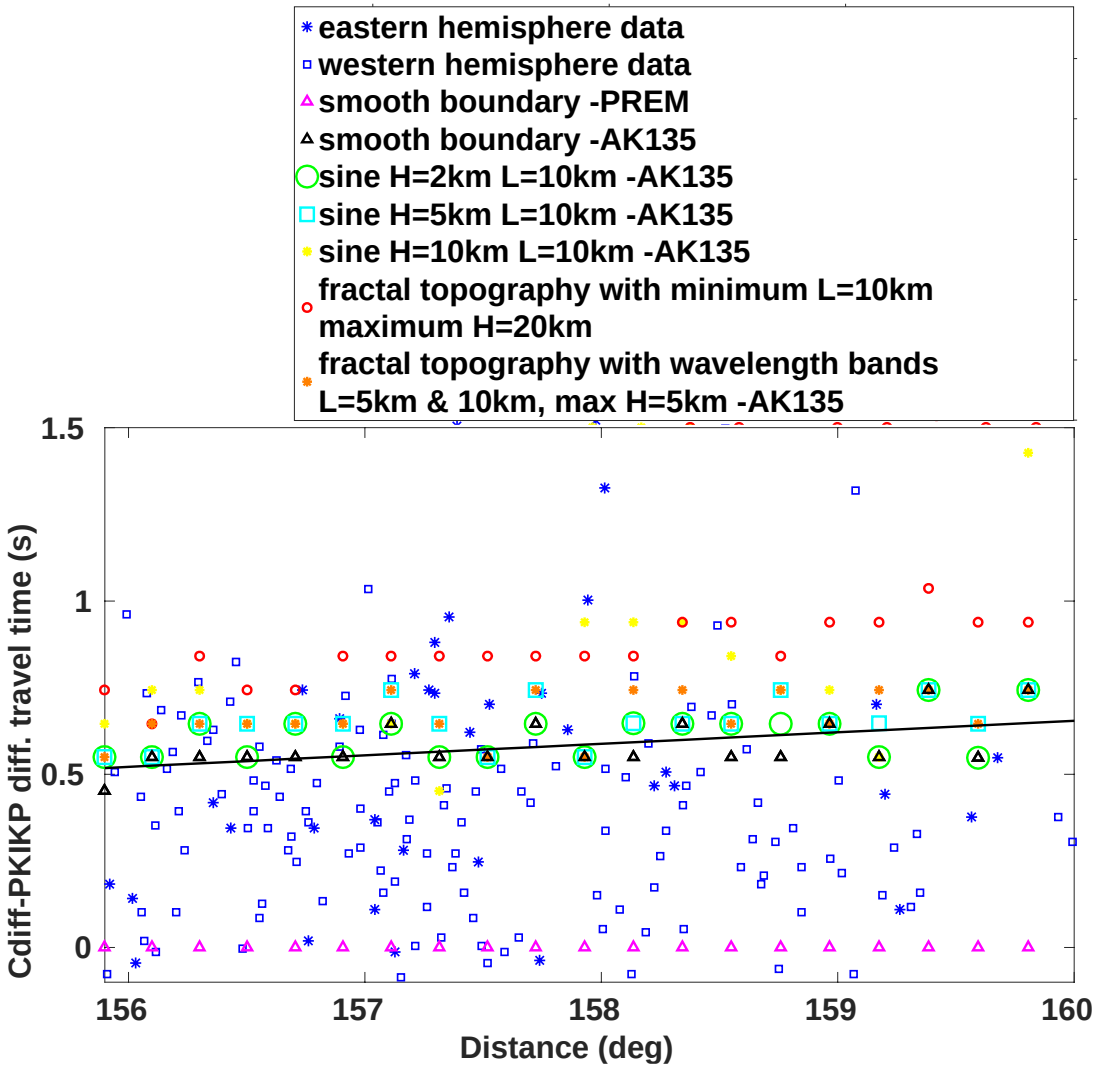

Figure 23: Differential travel times of PKP_{Cdiff}–PKIKP predicted by ICB topography models compared to observed measurements by Zou et al., 2008. Solid blue line is the least-squares linear fit line to the observed differential travel times.

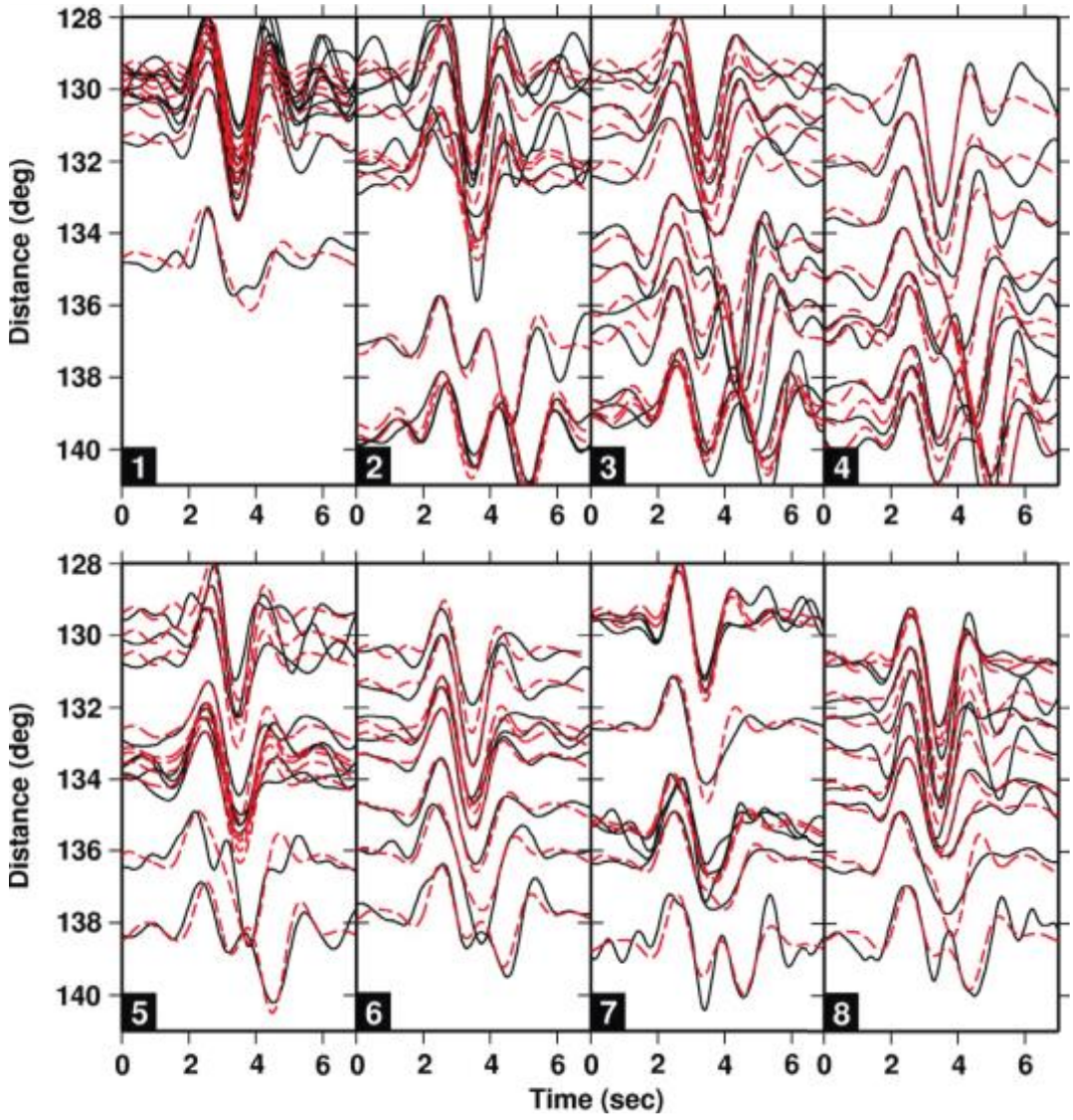

Figure 24: Data (black lines) and synthetic (dashed red lines) waveforms for the best fitting models, with bin number on the bottom left hand side of each box.

Bin_no	F1_coef	Q	Q^{-1}	F2_coef	Q	Q^{-1}	F3_coef	Q	Q^{-1}
1	83.613727	1000	0.001	83.802974	1000	0.001	70.967732	1000	0.001
2	85.560441	250	0.004	85.276604	250	0.004	72.611333	1000	0.001
3	82.509153	250	0.004	82.915265	250	0.004	76.029581	1000	0.001
4	84.496829	150	0.0067	85.298999	150	0.0067	80.766312	400	0.0025
5	82.858247	150	0.0067	83.924455	150	0.0067	83.447972	500	0.002
6	87.049504	350	0.0029	87.482262	350	0.0029	79.511963	1000	0.001
7	87.351888	1000	0.001	87.591308	1000	0.001	76.211646	1000	0.001
8	80.325922	1000	0.001	80.254185	1000	0.001	71.047361	1000	0.001

Table 1: Shows average cross correlation coefficient for data in each bin when synthetics were generated using F-layer values 57822, 1000, 300 (columns F1_coef, F2_coef, F3_coef) with inner core Q (and respective Q-1) values in adjacent columns. Highlighted signify the best fitting F-layer and top inner core Q combinations for each bin region.

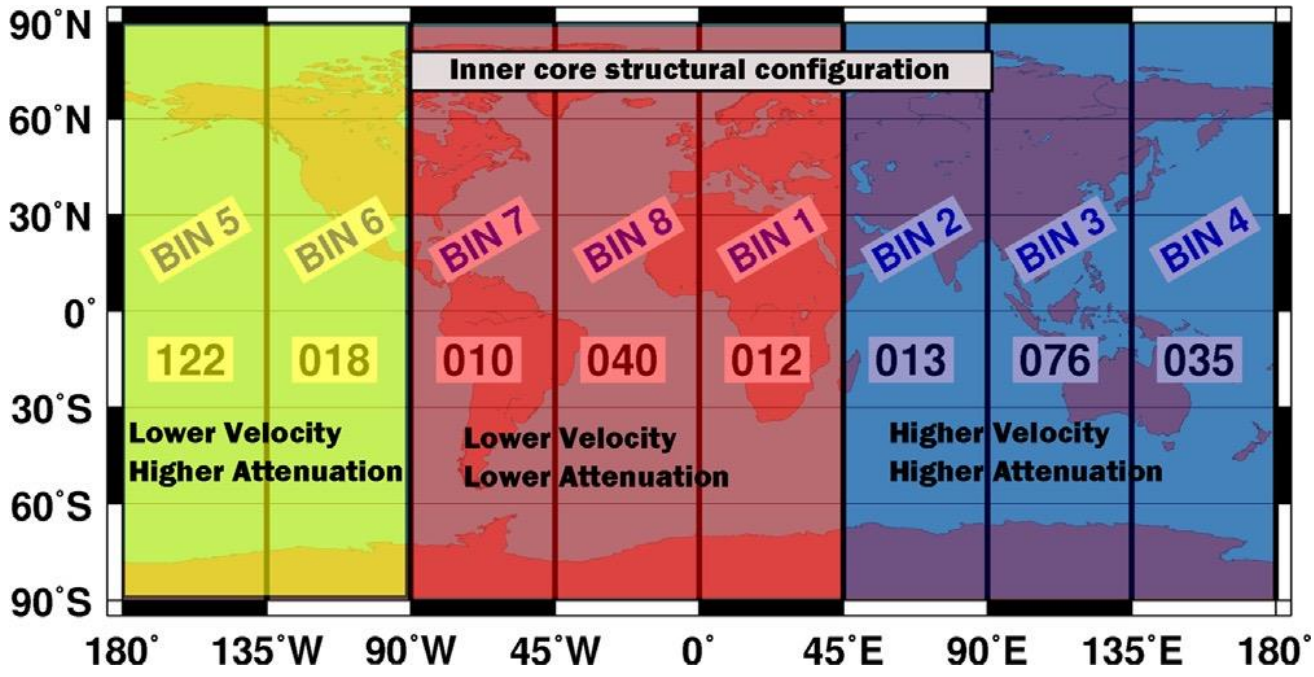

Figure 25: Division of distinct regions based on Velocity and Attenuation behavior on the topmost 80 km of IC (Figure courtesy – Attanayake et al.,2014).

Chapter IV

Interpretations

The goal of this section is discussing implications of the results produced by our two studies related to the ICB topography and apparent attenuation model near ICB. Each study has important indications on constraining best approaches to investigate properties such as topography, density contrast, and attenuation as well as on fine tuning the core structure to understand its dynamics. We intend on relating the two studies via the effect of ICB scattering to P wave attenuation in the vicinity of inner core.

4.1 Interpretations for ICB Models

4.1.1 Best Probes of ICB Topography

At epicentral distances beyond 100^{O} we have demonstrated that ICB topography (H < 5 km) does not create observable effects on 0.5 Hz P waves transmitted through and

diffracted around the inner core. Shorter range, pre-critical, PKiKP waveforms are better for probing the probable scales of ICB topography than either post-critical PKiKP or PKP_{Cdiff}, but in many cases the effects of focusing and defocusing by heterogeneous structure beneath receivers need to be carefully estimated to obtain confident bounds on topography.

4.1.2 Sampling of the ICB

Pre-critical PKiKP has been best sampled from stations and paths along the circum-Pacific belt, where available earthquake sources and stations are most likely to be concentrated at shorter range (Tkalčić et al. 2009; Waszek and Deuss 2015). The availability of data from underground nuclear tests and peaceful nuclear explosions in Eurasia and North America has also provided high-quality observations of both pre-critical PKiKP and PcP (Krasnoshchekov et al. 2005). The ICB sampling of longer-range post-critical PKiKP and PKP_{Cdiff}, shown in figures by Zou et al. (Zou et al. 2008) has the best overlap with PKiKP sampling of the ICB in the circum-Pacific region and the Eurasian, North American, and Australian continents. Large regions of the ICB, however, remain relatively unsampled by P waves incident on the ICB at combined narrow and grazing angles of incidence. These include regions beneath the Indian and Pacific Oceans and the poles. Of special interest to future investigations is the region beneath the eastern Indian Ocean, coincident with a predicted region of stronger inner core solidification in the dynamo model of Aubert et al. (2008).

4.1.3 Implications on Shallow IC

PKP_{Cdiff}/PKIKP amplitude ratios synthesized in models with ICB topography can be used to constrain the tradeoffs between viscoelastic attenuation of the upper inner core and scattering from its boundary roughness. The explanation for the scatter observed by Zou et al. (2008) in both amplitude ratios and differential travel times of these two phases require the existence of heterogeneous structures within Earth in addition to ICB topography. Since spatially extensive ICB topography of scales as high as 10 km are excluded from observations of pre-critical PKiKP, we suggest that the effects of scattering by small-scale heterogeneities in the mantle and scattering and lateral variations in intrinsic attenuation in the uppermost inner core may explain the typical fluctuation in the amplitudes of pre- and post-critical PKiKP as well as in the amplitude ratio PKP_{Cdiff}/PKIKP. Geodynamic calculations containing estimates of the upper IC viscosity (Buffett, 1997) and small scale lateral variations in temperatures in the region (Stevenson, 1987) are needed to determine the viability of any ICB topographic structures. BEM makes it feasible to conduct 2D boundary simulations at observable high frequencies, and at ranges of ICB incidences from pre-critical to diffraction. For a true inversion, we suggest minimizing the L1 norm of PKP_{Cdiff}/PKIKP amplitude ratios between high quality waveform observations and BEM predictions. An ideal data set would be stacked PKP_{Cdiff} and PKIKP waveforms recorded in a seismic array from different earthquakes located in varying azimuths, which will reduce the effects of small-scale heterogeneities in the crust and mantle.

4.1.4 Implications on F-layer Velocity

Our numerical results indicate that a velocity model that is in between AK135 and PREM for the lowermost outer core, such as the South Polar Region model (Ohtaki et al. 2012) or F-layer velocity model for western hemisphere (Ohtaki and Kaneshima, 2015), would be more suitable. Such models agree with observed amplitude ratios as well as observed differential travel times of PKP_{Cdiff} and PKIKP. These models have a flattened gradient in P velocity in the lowermost 150-250 km of the outer core, which may be the effect of a relative depletion in lighter elements (i.e. iron enriched) at the bottom of the outer core (Gubbins et al. 2008). Our result differs from results of the Zou et al. (2008) study, who found that a PREM-like model, without an anomalous F-region of reduced P velocity gradient at the base of the outer core, better fits the PKP_{Cdiff}/PKIKP amplitude ratio, while an AK135-like model with an F region, better fits differential travel times of PKIKP-PKP_{Cdiff}. With our BEM modeling, we prefer a F region model mid-way between AK135 and PREM to fit both the travel time and amplitude of PKP_{Cdiff}, although our results merit further tests with numerical methods capable exploring the effects of velocity gradients in the F region. Additionally it would be suitable to consider the extent of topographic effects on differential travel times of PKIKP-PKiKP when determining the velocity jump at the ICB and the structure of the upper 300 km of the IC, and the effect on differential travel times of PKIKP-PKP_{Cdiff} when determining the velocity structure below that (Souriau and Poupinet, 1991; Kaneshima *et al.*, 1994; Song and Helmberger, 1995; Tkalčić, 2015).

4.1.5 . Implications on ICB Density Contrast

In epicentral distances less than 15° our simulations show that a topography in the shape of a sine wave with wavelength ~10 km and a peak to peak height ~2 km can cause a 1/3rd of amplitude reduction. A similar shaped topography with a height 5 km, which is an upper bound predicted for a region under South American continent (Cao, Masson and Romanowicz, 2007), may reduce PKiKP amplitude by a factor of as much as 0.6. It is possible that a mosaic structure (Krasnoshchekov, Kaazik and Ovtchinnikov, 2005) may explain the wide range of density contrasts proposed including the normal mode predictions ~0.6-0.8 gcm^{-3} (Dziewonski and Anderson, 1981; Gubbins, Masters and Nimmo, 2008). However, we must note that reflected phases would reveal a more accurate picture than normal mode studies that vertically average elastic properties over broader scale lengths.

4.2 Interpretations for Top IC and Bottom OC Attenuation Model

This study resolves an important seismic characteristic in the top 80 km of the inner core. The high attenuation in 45E-180E and low attenuation in 90W-45E is quite in line with previous reports. However, the high attenuation seen in 45E-180E in quasi-eastern hemisphere continues to the 180W-90W portion of quasi-western hemisphere according to our data. This gives us a positive correlation of Qp^{-1} with Vp in the fast quasi-eastern hemisphere and in the slow quasi-western hemisphere, except for the

180W-90W section, which encompasses the inner core underneath the central Pacific region. This inverse relationship of low velocity and high attenuation is commonly observed in the mantle due to the presence of small amounts of melt, and is observed similarly for the upper most inner core by Iritani et al (2014) and Pejić et al (2017). Authors of both these studies observe a high attenuation in the central Pacific where velocity is confirmed to be low by a series of past papers.

Iritani et al.,2014 (Iritani, Takeuchi and Kawakatsu, 2014b) confirms a high attenuating (Qp^{-1} ~0.0065) eastern hemisphere (43E-177E) and a low attenuating western hemisphere (183W-43E) where the region under South America shows an increasing attenuation with depth down to about 250 km from the ICB. So the attenuation under western Africa is generally lower ~0.003 while under North America/central Pacific it gradually increases within 0.0025 - 0.005 from the ICB to 300 km below (Figure 26).

Pejic et al.,2017 (Pejić *et al.*, 2017) also reports similar pattern whereas high attenuating regions exist in a 400 km thick top layer of IC beneath Asia and Pacific (figure 27). Their finding of a Q ~150 in the Pacific region agrees well with our bin 5 (figure 25) best model. We should keep in mind that both above recent studies sample a region of the inner core 2-4 times thicker than our sampling of the IC.

Our result clearly implies that the upper inner core material as well as dynamics is probably more complex than a lateral degree-one spherical harmonic structure. A picture of an upper inner core with a more complex structure rather than a simple degree-one structure has also been suggested by suggested by Irving and Deuss, 2015 for velocity anisotropy and by Pejic et al.,2017 and Iritani et al., 2014 for velocity and attenuation.

Geodynamic studies predict that heterogeneities in the physical properties of the uppermost inner core may be created due to variations in chemistry and heat transport as it is freezing or melting. The regions that are melting or freezing are not clear, and there exist two main contradicting hypotheses on this matter. One is that the western hemisphere is freezing while the eastern hemisphere is melting (Alboussiere et al. 2010; Monnereau et al. 2010), so that the observed hemispherical heterogeneity is caused by differences in the material texture of the two hemispheres due to the convective translation of the inner core material from the western to the eastern hemisphere. Another is that the inner core growth is thermally coupled to the core-mantle boundary, promoting an eastern hemisphere cooler than the western hemisphere (Aubert *et al.*, 2008; Gubbins *et al.*, 2011) (figures 28 and 29). In the second scenario, the eastern hemisphere would grow faster causing less texturing of growing Fe dendrites, allowing for P waves to travel faster but lose more energy to scattering from smaller scale heterogeneities, compared to the possibly more textured slowly growing western hemisphere (Tkalčić, 2015).

The case for a convecting inner core is difficult to confirm from seismic data. First, a pattern that is more than a degree-one heterogeneity cannot easily be reproduced with a convective process (Alboussiere, Deguen and Melzani, 2010; Deguen, 2012). Second, a large grain size difference to explain a scattering interpretation of the observed body wave attenuation is not well supported by thermodynamic calculations (Yoshida, Sumita and Kumazawa, 1996; Buffett, 1997; Bergman, 1998; Deguen, Alboussiere and Brito, 2007; Bergman *et al.*, 2010). Additionally, there is evidence of degree-one heterogeneity (Deuss, Irving and Woodhouse, 2010; Waszek and Deuss, 2011; Blom *et al.*, 2015) disappearing after ~200 km depth from the ICB (Cao and Romanowicz, 2004b;

Waszek, Irving and Deuss, 2011; Tanaka, 2012; Iritani, Takeuchi and Kawakatsu, 2014b; Pejić *et al.*, 2017) which may not be possible if the inner core material were convecting from WH to EH internally.

In our viewpoint, the seismic picture of IC can be more directly explained if the temperatures at IC are coupled directly with the CMB (figures 28 and 29), where the growing front in the eastern hemisphere is, on average, colder than the western hemisphere. Along this line, the positive correlation of Vp and Qp^{-1} may be explained with a combination of grain size and impurity concentration.

$$Q_p^{-1} = AT_w^{\alpha} d^{-3\alpha} e^{-\alpha E/RT} \qquad \text{Equation (4.1)}$$

Equation 4.1 (Gribb and Cooper, 1998; Jackson *et al.*, 2002) gives the relationship between grain size (d) and attenuation (Qp^{-1}) in terms of wave time period (T_w), Temperature (T), activation energy (E) and other constants for ICB (A, α, and R). According to this a larger grain size for western hemisphere and a smaller grain size for eastern hemisphere are expected. These grain sizes are estimated to be 10-20 m for ICB temperature 6050K and pressure 330GPa (Attanayake, 2012; Attanayake, Cormier and De Silva, 2014), which is comparable with current geodynamic calculations(Yoshida, Sumita and Kumazawa, 1996; Buffett, 1997; Bergman, 1998; Deguen, Alboussiere and Brito, 2007).

$$V_p = \sqrt{\frac{K + \frac{4}{3}\mu}{\rho}} \qquad \text{Equation (4.2)}$$

$$V_s = \sqrt{\frac{\mu}{\rho}}$$ Equation (4.3)

In addition to the grain size, the other component that we assume to affect the attenuation as well as velocity of wave propagation is the impurity concentration within the predominantly Fe inner core. Melting of the inner core can produce a refined denser layer of material that is depleted of lighter elements (Alboussiere, Deguen and Melzani, 2010). Hence the increase in density due to melting would lead to a slower velocity (equations 4.2 and 4.3). At the same time, a lower concentration of lighter elements (impurities in this case) implies less defect concentration and less mobility of grain boundaries (Jackson and Anderson, 1970), leading to less attenuation of wave energy. Hence a warmer western hemisphere of upper IC that is coupled to the high temperature CMB regions, such as underneath the western African super-plume, can reasonably have lower velocities and attenuations. Similarly, a cooler eastern hemisphere that is mainly underneath Asia can have higher velocities and attenuations.

We make a note that cold and hot areas of the CMB are derived starting from velocity tomographic images in the lower mantle. Many tomographic models (Houser et al. 2008; Koelemeijer et al. 2016; Kustowski, Ekström, and Dziewoński 2008; Panning and Romanowicz 2006; Ritsema et al. 2011; Simmons et al. 2009) of Vs and Vp in the lower mantle agree on lower seismic velocities beneath western Africa and central Pacific as seen in Figure 30. Since derivative of velocity with respect to temperature is known to be negative (dV/dT < 0) for dominant (Mg, Fe)SiO3 (Jackson, 1998), the low velocities

are interpreted to be hotter and the high velocities are interpreted to be cooler. This is how we assume hotter areas of CMB beneath the Africa and Pacific.

However, if the central Pacific region (Bins 5 and 6) that belongs to western hemisphere has higher than average temperatures, it is possible for the velocities to be lower with increased attenuation according to Equation 4.1. Therefore, the simplest way to explain our result of attenuation model is that the degree-one velocity structure results mainly from a differential impurity concentration while the central Pacific region has higher than average homologous temperature (i.e. Temperature divided by Melting Temperature). We may interpret this as the Pacific region is either melting faster than the rest of the WH, or as Pacific region is currently melting while the rest of the WH was subjected to melting in the past and is now growing slower than the EH. In the case that the average positive growing rate of IC is implying a freezing/growing across full surface of the ICB, the Pacific region may also be just closer to melting temperature (without really melting) than the rest of the warmer WH.

4.3 Combined Implications

The first study described in this thesis explored the effects of boundary roughness on P waves interacting with the ICB at a range of different incident angles, and an interpretation of fair upper bounds to sinusoidal or fractal shaped topography at a few regions sampled by seismic data. This study helps to quantify the scattering contribution

to the attenuation of PKiKP, PKP_{Cdiff} and PKIKP purely due to inner core boundary topography.

The second study is a data-based exploration of the observed attenuation of P waves (intrinsic + boundary scattering + volumetric scattering) (Cormier, Xu and Choy, 1998) on the top 80 km of the IC as well as the bottom 200 km of OC. Here we derived attenuations positively correlated with P velocity structure in the eastern hemisphere and the 90W-45E part of the western hemisphere, while the pacific region shows attenuation negatively correlated with its lower velocity.

Clearly a hemispherical or a low order spherical harmonic structure of inner core properties is suggested from seismic velocity and attenuation of the uppermost inner core. It is, however, unclear whether the attenuation specifically is intrinsic or caused by scattering. While it is quite possible to be a combination of both types, it has long been difficult to quantify their effects separately. The reason that it is important to reconcile these effects is because of their implication for the exact texture of the inner core near its boundary, which is related to the mechanism of inner core growth. For example, is the inner core growing from precipitating solid iron in the outer core above its boundary or from a solidification front of iron at its boundary? Minimally an understanding of seismic attenuation mechanisms sets the stage to reconcile between the two hypotheses for the freezing-melting geographic patterns currently suggested; the translating IC or the ICB temperatures coupled to CMB via heat flow.

We attempt to fuse the results of our two studies in order to understand the contribution of scattering from ICB topography towards the observed attenuation in those regions. We can look at the waveform change made by topography in PKiKP and PKIKP

observed at the same 130°-140° event-station distance range in which the data set in study #2 was collected in. The dominant frequency of this data set and the dominant frequency used for the source pulse in BEM is the same at 0.5Hz. Hence it is acceptable to directly compare and integrate the results of them regarding the inner core boundary area, without additional approximations.

Note that the P wave attenuation that we denoted as Qp^{-1} (or quality factor Qp) comes from the following equation 4.4 (Schubert, G., 2007), where ΔE is the energy lost per cycle and E_{max} is maximum energy contained in a cycle. The dependence of 3D elastic wave amplitude on Q is as shown in equation 4.5. Here k corrects for geometric spreading and reflection/transmission coefficients.

$$Q^{-1} = \frac{\Delta E}{2\pi E_{max}} \qquad \text{Equation (4.4)}$$

$$A = k * \exp\left(\frac{-\pi f t_{IC}}{Q_p}\right) \qquad \text{Equation (4.5)}$$

According to figure 16, a sinusoidal topography of wavelength 10 km and heights as much as 20 km, does not make a considerable effect on the PKIKP/PKiKP amplitudes. Hence we can safely assume minimal effect of ICB topography on the apparent attenuation (Qp^{-1}) obtained with 130°-140° waveforms.

The structure on figure 23 and Table 1 is likely to reveal a combination of intrinsic and volumetric scattering attenuations in the upper most inner core. Therefore,

the differential grain size and/or impurity concentrations implying a freezing eastern hemisphere, slowly freezing (or melting) western hemisphere, and a currently melting (or melting rapidly than average WH) central-Pacific is a valid hypothesis for the observed attenuation structure, in the light of our understanding of topographic effect. In fact being able to identify which event-station distances are less affected by boundary scattering is one of the compelling results of our study #1, that is evidenced in this combining attempt. We are able to securely investigate purely volumetric properties near ICB at post-critical distances (extending past the C-cusp point) using PKIKP/PKiKP amplitude ratios.

However even if we eliminate topography as a cause of attenuation of P waves observed at the 130^{o}-140^{o}, we have not investigated the scattering from volumetric heterogeneity beneath the ICB. Fluctuations of volumetric properties in the path of a seismic ray essentially scatters the wave, and removes energy from the front of the main reflection/refraction pulse. The scattered energy gets redistributed to later arrival times, generating increased amplitudes in the coda of main pulse. Noticeable PKiKP coda amplitudes are associated for IC scattering, for observations made at <100^{o} (Vidale and Earle, 2000; Koper, Franks and Dombrovskaya, 2004; Leyton and Koper, 2007; Peng *et al.*, 2008; Wu and Irving, 2017). These observations are compatible for 1-10 km size order of scatterers within the top few hundred kilometers of IC. The effect of volumetric scattering on PKiKP beyond 100^{o} has not been studied at present and changes in coda would be difficult to observe in the 130^{o}-140^{o} distance due to the high reflection coefficient of post-critical PKiKP in this post-critical range. Wu and Irving 2017 present three different possible mechanisms for upper IC scattering; partial melt, misalignment of

crystals, and grain sizes, that could produce the small-scale inhomogeneities in elastic velocities.

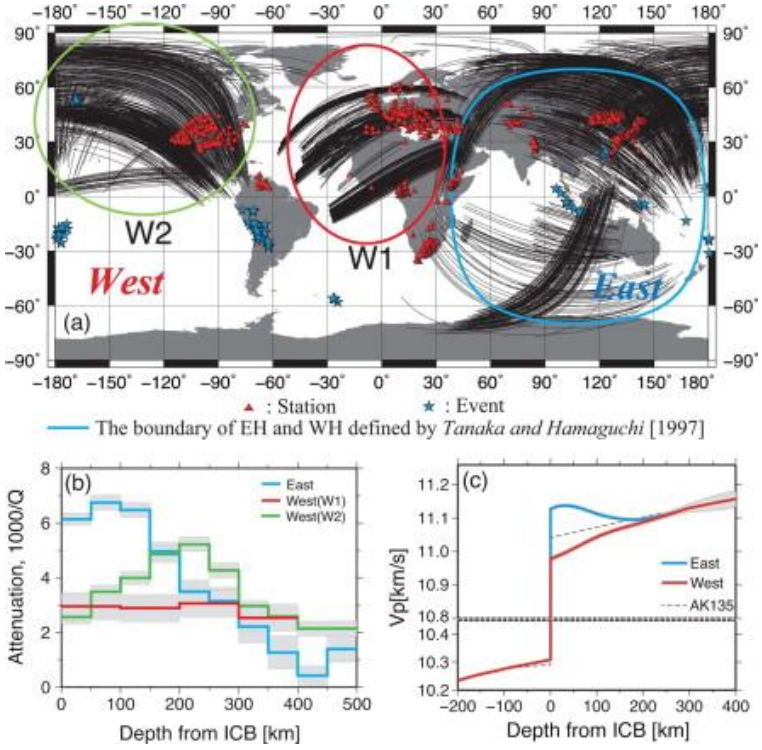

Figure 26: (a) The distribution of stations (red triangle), events (blue star) and ray paths of core phases (black line) that are used in this study. The blue line indicates the boundary between the eastern and western hemispheres defined by Tanaka and Hamaguchi (1997), and the inside of the blue circle corresponds to the eastern hemisphere; the red and green circles indicate two areas (W1 and W2) in the western hemisphere that show different attenuation structures as in (b). (b) Attenuation profiles for the top 500 km and (c) velocity profiles for the top 400 km of the inner core obtained by analyzing short period data (the dominant frequency of 1 Hz) – Image and caption from (Iritani, Takeuchi and Kawakatsu, 2014a)

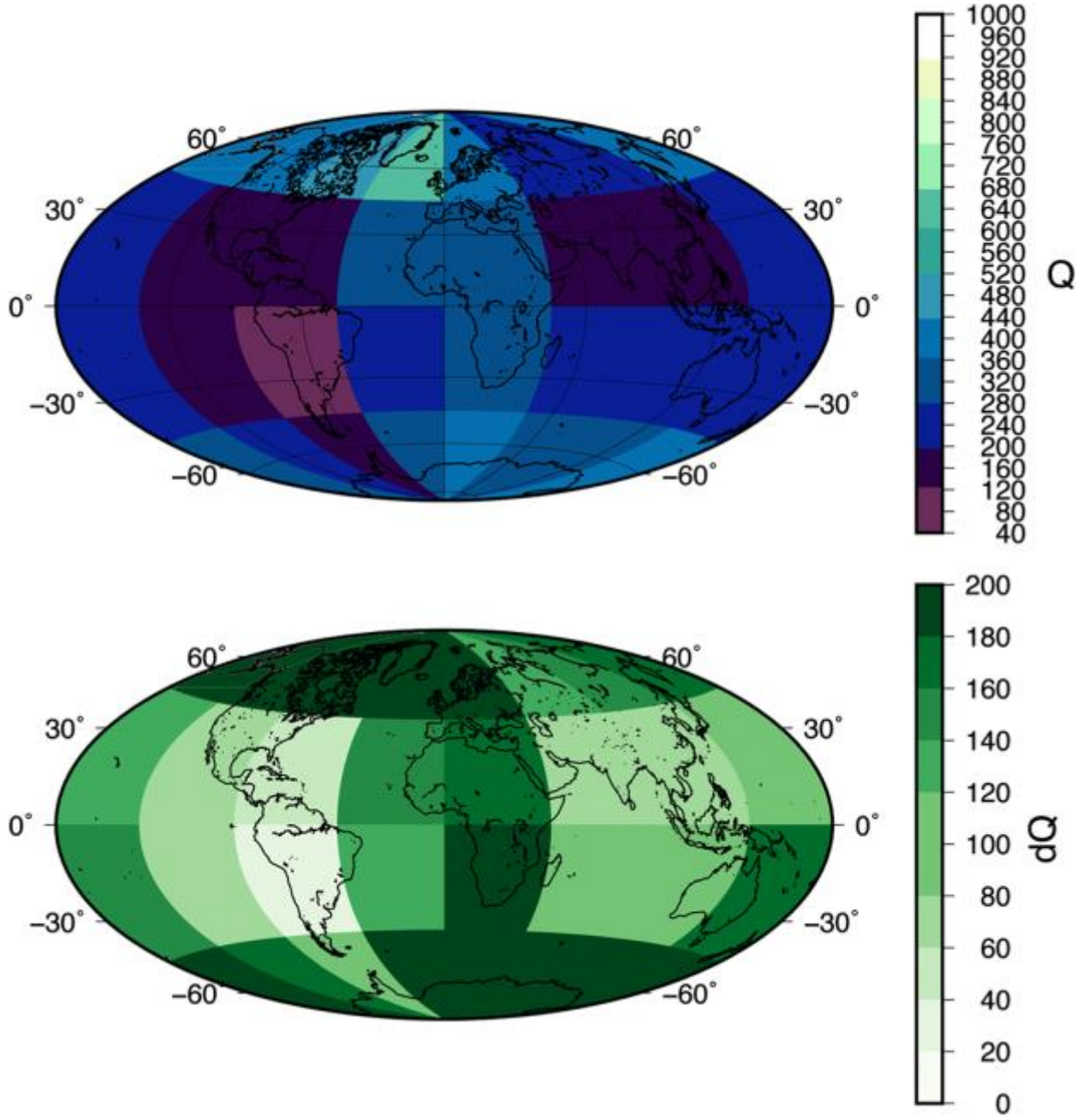

Figure 27: Preferred tomographic model of Q values obtained for the 400 km thick layer at the top of the inner core. (top) Shown in these images are the absolute values of estimated Qp and their confidence intervals.- Image and caption from (Pejić et al., 2017)

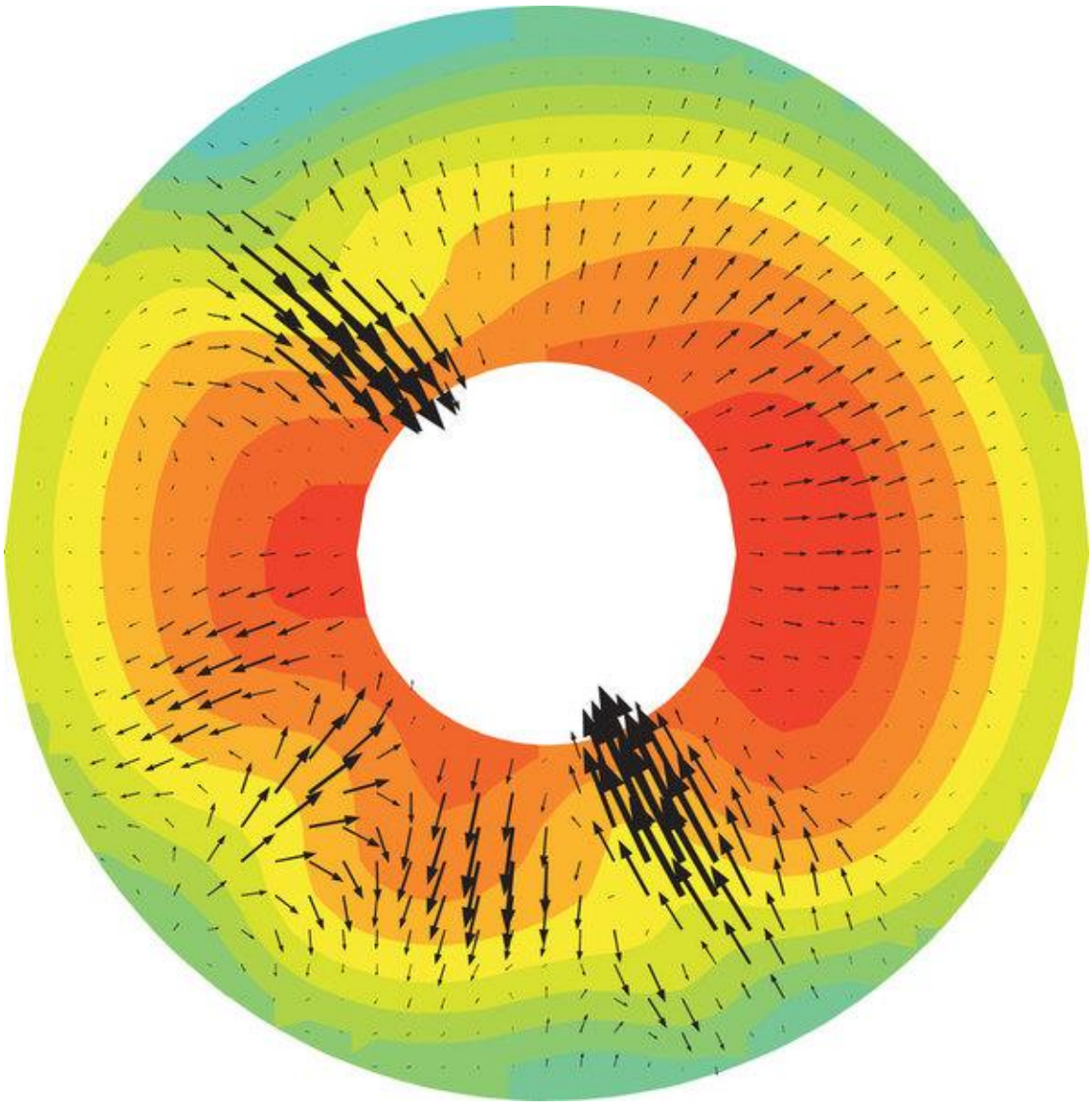

Figure 28: Temperature (colour contours) and fluid flow (arrows) on the equatorial section. The lowest temperature is blue and the highest temperature is deep red. We note the narrow down wellings beneath cold regions (the two major ones coinciding with the 'ring of fire' around the Pacific) and broad up wellings (corresponding to the mid-Pacific and African super plume). This leads to relatively large areas of negative (melting) and low-positive heat flux on the ICB and relatively small areas of strong-positive heat flux (freezing). – Image and Caption from (Gubbins et al., 2011)

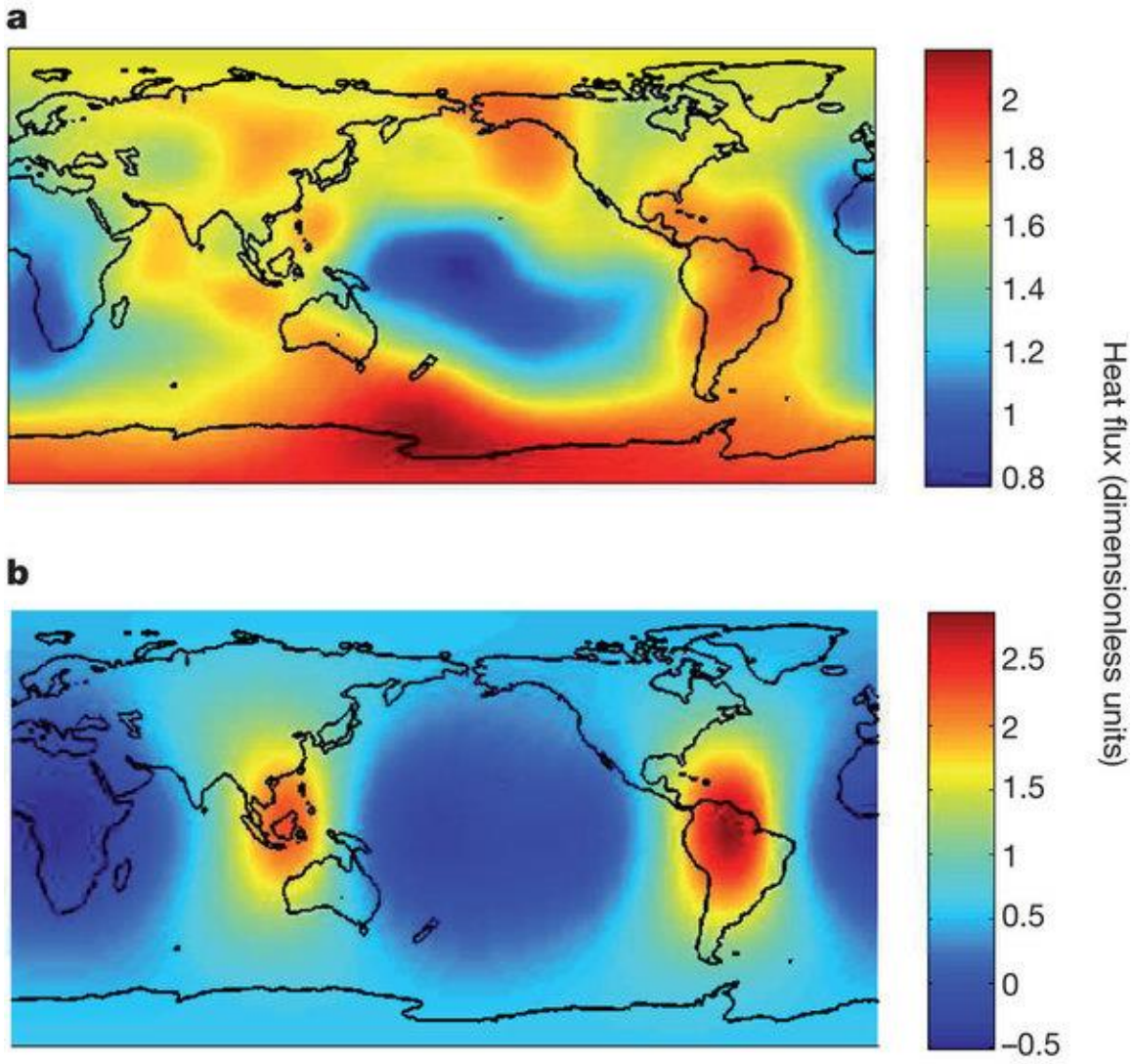

Figure 29: Effect of mantle inhomogeneity on heat flux distribution at the inner core surface. Heat fluxes are applied to the upper boundary (a) and calculated on the constant-temperature lower boundary (b) in a geodynamo simulation where the flow is strongly coupled to the boundary thermal anomalies. The range of heat flux across the upper boundary ranges from 0.77 to 2.16 dimensionless units outwards and across the lower boundary ranges from 20.51 to 2.89 dimensionless units (negative values indicate heat flux into the inner core). – Image and Caption from (Gubbins et al., 2011)

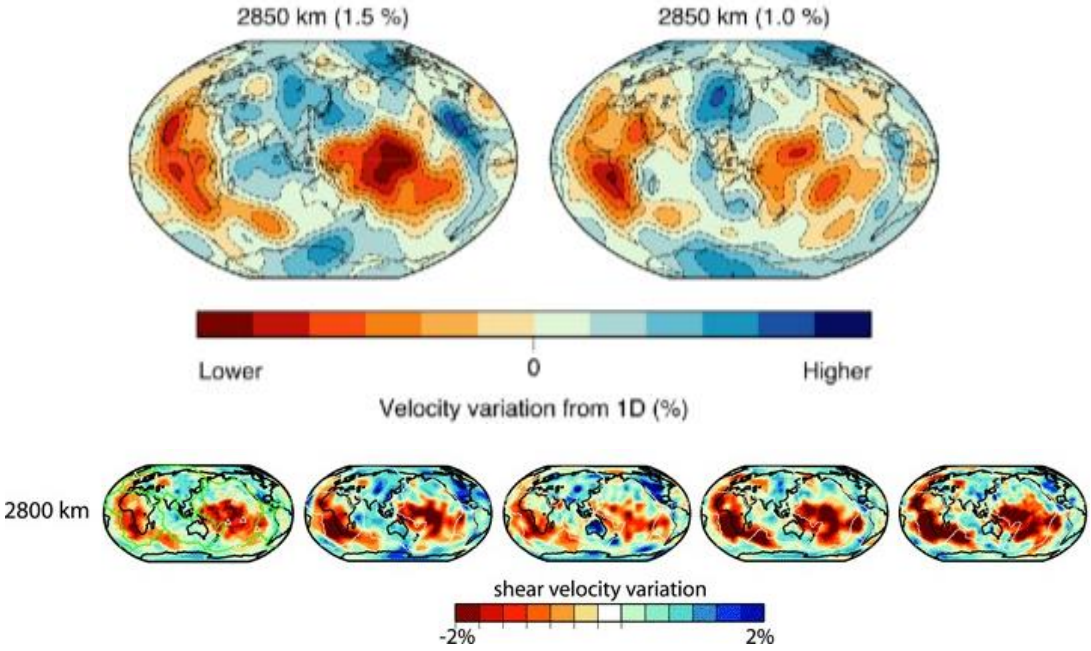

Figure 30: Velocity topography models of mantle at CMB depths (2800 – 2850 km). Upper panel:Shear velocity variations dln(Vs) on left and Compressional velocity variations dln(Vp) on right from SP12RTS (Koelemeijer et al., 2016). Lower panel: From left to right, shows shear velocity variations from S40RTS (Ritsema et al., 2011), S362ANI (Kustowski, Ekström and Dziewoński, 2008), SAW642AN (Panning and Romanowicz, 2006), TX2008 (Simmons, Forte and Grand, 2009), HMSL-S (Houser et al., 2008). Note the low velocity regions under Africa and Pacific independently observed by all models.

Chapter V

Conclusions

In this thesis we demonstrate two approaches in understanding the nature of the inner core boundary region. First, we explore the topography that may exist at the ICB by using a boundary-specific numerical method. Second, we use a seismic data set to invert for the attenuation just above and below the ICB. We arrive at the following main conclusions based on these studies:

Study of Inner Core boundary topography:

1) A boundary element method is used to synthesize seismic body waves interacting with an ICB-like interface in a 2-layer configuration. For inner core regions sampled, amplitudes and coda of pre-critical PKiKP 1.5 Hz reflections set an upper bound height of 1 to 2 km for ICB topography in the shape of sinusoids or fractals with lateral wavelengths 1 to 20 km.

2) In this wavelength band of ICB topography, post-critical PKiKP is relatively insensitive to ICB topography approaching 5 km height. Hence any higher variations seen in post critically reflected P waves and their associated IC refractions, for earthquake doublets would likely be due to the focusing/defocusing and scattering effects of other heterogeneities such as volumetric velocity heterogeneities in the upper mantle and crust beneath receiver arrays or in the uppermost inner core.

3) The existence of ICB topography on this order leads to an underestimate by several percent of the magnitude of the density discontinuity at the ICB, which is important for driving the geodynamo by compositional convection. It can also smooth over minimums and zeros in the inner core boundary reflection coefficient in the pre-critical range (65° - 95°), providing a mechanism to explain pre-critical PKiKP amplitudes alternative to a mosaic structure of impedance contrasts across the ICB. Resolving the nature of density contrasts at the ICB are key in understanding the component of OC convection driven by buoyancy of light elements.

4) Although insensitive to topographic height variations up to 5 km, the post-critical data we have chosen, have a strong overlap in ICB sampling with the pre-critical PKiKP data that limit topography height to 1 to 2 km.

5) Body waves diffracted around the ICB are relatively insensitive to topography approaching heights of 10 km and wavelengths 10-20 km. Unless PKP_{Cdiff} observations are occasionally sampling localized ICB regions with topography higher than 10 km, the large scatter in PKP_{Cdiff} / PKIKP amplitude ratios and their differential travel times in the 0.3 to 0.5 Hz band (Zou et al. 2008) might be explained by the focusing and defocusing effects of small-scale heterogeneity in the crust and upper mantle together with small-scale lateral variations of attenuation in the mantle and upper IC.

6) Combined amplitude ratio and differential travel time data of PKIKP-PKP_{CDiff} are best matched by a flattened velocity gradient in the lowermost outer core, with vertical gradients in Vp that is in between AK135 and PREM values near the ICB. This is consistent with an iron enrichment near a solidifying and melting ICB.

Study of attenuation structure in the Inner Core boundary region:

1) A cross-correlation between synthetic and observed PKiKP-PKIKP combined waveforms is used to find the best Qp^{-1} (the attenuation parameter for elastic P waves) for the uppermost 80 km of the inner core and lowermost 200 km of the outer core. Dividing data into eight 45° wide longitudinal bins allowed to

determine best-fitting models of attenuation for different areas in the uppermost inner core.

2) In uppermost 80 km of the inner core, the regions within longitudinal borders 45E-180E and 180W-90W show generally lower Qp^{-1} than the rest. The latter region has lower Qp^{-1} than the former, but higher than in the longitudinal sector 90W-45E.

3) When this attenuation model is compared with known large-scale P velocity models of the inner core, we notice that the attenuation structure in the uppermost inner core is more complex than a hemispherical, spherical harmonic degree-one pattern. We see a negative correlation between Vp and Qp^{-1} in the inner core beneath the central Pacific in WH, and a positive correlation in the rest of WH and in EH, where WH and EH denote a quasi-western and quasi-eastern hemispherical region respectively.

4) The negative correlation between attenuation and P velocity beneath the western Pacific portion of the WH can be a result of active partial melting or high homologous temperature ($T/T_{melting}$) in this region.

5) The positively correlated higher Vp and Qp^{-1} beneath the remainder of the inner core may be explained by faster solidification in a relatively colder environment in the EH and slower solidification in a relatively warmer environment in the WH. It is possible that a faster growth rate in EH prompts dendrites to be less uniformly oriented, attenuating energy strongly by scattering high frequency energy away from the earliest arrival time of the main transmitted wave pulse. A higher solid fraction in this cooler, more rapidly solidifying, region could result in a faster P velocity, given a negative temperature derivative of P velocity. On the other hand, a slower growth rate in the WH may permit the Fe crystals to be more aligned and hence low attenuations and low velocities resulting from relatively high temperatures. Also better alignment of anisotropic single crystals (Deguen, 2012) in the WH would result in the sort of higher anisotropy in the region compared to the EH observed by many previous studies.

6) The Qp^{-1} for the lowermost 200 km of the liquid outer core, that gives best cross-correlation between observed and predicted transmitted P wave waveforms is 0.001. This is a higher attenuation than that of the Preliminary Reference Earth Model (0.000017). This higher attenuation in the lowermost outer core might indicate a possible increase in viscosity in an iron enriched region above the solidifying/melting boundary of inner core.

Unified conclusions from structure near ICB:

1) The attenuation structure measured from P waveforms sampling the inner core is not likely to be strongly biased by any effects of scattering by inner core boundary topography. We predict that plausible upper bounds of ICB topography will only weakly affect the PKIKP and PKiKP amplitudes in the 130^{o}-155^{o} great circle range where inner core attenuation measurements are conducted.

2) The observed attenuation is likely a combination of intrinsic and volumetric scattering attenuations in the uppermost inner core. The lack of strong codas following the PKIKP+ PKiKP waveforms from which we measured inner core attenuation suggest that the effects of volumetric scattering in the uppermost 80 km only minimally contribute to the measured attenuation. Hence the high attenuation will primarily be caused by viscoelastic attenuation in accord with (Cormier and Attanayake, 2013).

3) Both our inner core attenuation study and the study of inner core topography support the existence of an iron-enriched layer near the bottom of the liquid outer core near the inner core boundary.

4) Inner core-related geodynamical predictions of topography less than a few hundred meters of height (Buffett 1997; Monnereau et al. 2010; Alboussiere et al. 2010; Deguen 2012) are still under the upper bounds we predict. More PKiKP observations as well as PKP_{CDiff} are required to better constrain the

question of topography and density contrast at the ICB. Current estimates of ICB density jump are possibly obscured by the topography that was not taken into account hitherto in seismological studies that inverted PKiKP data for density contrasts. This consideration is suggested in Chapter 6.

Our upper limits on topography supports both hypotheses on the IC growth mechanism – internally convecting and boundary temperatures coupled to CMB. In fact, the synthesized PKiKP, PKIKP, and PKPCdiff waveform results presented in Chapter 3 can be used as basis to carefully probe geographical distribution of topography using careful sets of data in future. Specifically confirming the levels of topography in transfer zones between high Vp and low Vp regions such as edges around Pacific region, may be helpful to establish which growth procedure is more plausible. The attenuation model we derived is definitely more supportive of an IC surface temperatures being coupled to conductive heat transport across the CMB, due to the existence of Pacific area of being inversely related Vp and Qp^{-1}. However more experimental evidence of Fe-Ni + light element (Si, S, C) alloy behavior in the inner core conditions are also needed to for a complete understanding of the structure.

Chapter VI

Future Directions

Here I discuss several avenues in which the current study can be extended to improve existing knowledge about the inner core. These include implementing the BEM code on computational facilities having more nodes and cores to reach higher signal frequencies, simulating the upper inner core volumetric heterogeneities to understand possible tradeoffs of it with boundary topography and seismic attenuation, and assembling denser data sets to better constrain the heterogeneous structure of the growing inner core.

- Currently we are able to reach a dominant signal frequency of 1Hz for simulating small angle incidences ($< 30^{o}$) and 0.5 Hz for higher incident angles. Reaching 1-2 Hz for the full distance range would be ideal for observing the behavior of PKiKP coda and waveform broadening of PKIKP. However higher signal frequencies require the use of smaller size and a larger number of boundary

elements (see Chapter 2), which will result in larger matrices to invert for during the solution of the boundary integral equations. This will require the adoption of techniques to reduce storage during matrix inversion (Bogiatzis, Ishii, & Davis, 2016) as well as the access to a computer cluster facility with more nodes and longer permitted run times.

- I suggest simulating post-critically reflected PKiKP at 1-2 Hz dominant frequency with a series of ICB topography models to explore the appearance of a consistent scattered phases in coda, such as the 'm-phase' observed by (Adam & Romanowicz, 2015) in the 149^{o} – 178^{o} range (see Chapter 1). Another point will be to validate the effect of topography on PKiKP and PKIKP at distances larger than 130^{o}. This is done in the current study by extrapolating 0.5 Hz results to 1-2 Hz by assuming that the magnitude of scattering effects scale as the product of signal wavelength (k) and scatterer size (a). However simulating in higher frequency would validate whether or not the origins of large amplitude fluctuations such as those seen in the 137.8^{o} earthquake doublet PKIKP-PKiKP (Cao, Masson, & Romanowicz, 2007) and PKP_{Cdiff}/PKIKP amplitude ratios beyond 150^{o} (Zou, Koper, & Cormier, 2008) are due to topography.

- The answer to the question of which mechanisms are responsible for attenuating compressional waves at the top few hundred kilometers of inner core is important to understanding the processes of inner core solidification. There are a few factors

obstructing a clear-cut answer. One leading factor is the difficulty to separate the attenuation caused by intrinsic energy loss to heat and random molecular motion and the apparent pulse attenuation due to the redistribution of energy in time and space by scattering of the wave field by partial melt lenses and grain sizes on the order of wavelength, including the effects of grain misalignments (V. F. Cormier & Li, 2002; X. Li & Cormier, 2002; Hrvoje Tkalčić, 2010). To aid in this separation we suggest a simulation study of volumetric heterogeneities placed in the upper inner core with a numerical integration of the elastic equations of motion by a pseudospectral method (Cormier, 2000) and to compare with observation of PKiKP waveforms up to diffraction distances. This may be an extension of Cormier, 2007 which simulated 120^{o} - 140^{o} PKiKP forward and back scattered through horizontally and vertically stretched heterogeneities of wavelengths less than 20 km with a 10% P velocity perturbation. It would be interesting to test if large variations in amplitude or amplitude ratios seen in previous post-critical observations are in fact due to volumetric heterogeneities, and if so of what scales. With our established method for invoking ICB topography we could now attempt to quantify and compare the high frequency PKiKP coda resulting from ICB roughness and upper IC volume scattering.

- Another persistent issue in resolving upper or even deeper inner core structure is the difficulty to discriminate between boundary effects with deeper effects. We usually employ a 'reference' phase along with the wave phase that samples the region of interest. The reason is to suppress or cancel the effects added to the

wave front by propagation through shallower structure, by comparing two waves whose paths sample shallower structure nearly identically except for the inner core. For example, PKiKP is used for distances below 155.5^{o} along with PKIKP that samples down to first 352.5 km of inner core, while PKP_{Cdiff} can be used with PKIKP that samples deeper than that. The idea is that the path of the reference phase is very similar except that it does not sample the inner core, so that the differential travel time or the amplitude ratio of that with PKIKP are caused purely by the IC region sampled by PKIKP. Unfortunately, these reference phases are contaminated by heterogeneous structure near ICB such as topography. Until this study we did not have a good idea of how PKP_{Cdiff} reacts to topography. With our results we can now go forward with these types of studies assuming minimal effects of ICB topography.

- PKP_{Cdiff} is usually difficult to detect within noise. However stacking of array traces is an excellent method of resolving such phases as random noise tends to get negated during the process (D. Li, Sun, & Helmberger, 2014). With the advances in recent array deployments (USArray in North American continent, HiNet near Japan) PKIKP- PKP_{Cdiff} can be used for imaging the deep IC. In addition, we suggest performing array processing of PKP_{Cdiff} collected from a number of events distributed evenly in event azimuth at stations of about 2^{o} spread. Such a study may corroborate whether the high variation of PKP_{Cdiff} /PKIKP is a result of lower mantle small-scale inhomogeneity.

- Clearly there is a tradeoff between the ICB density contrast, which is important to driving the geodynamo by compositional convection, and topography (see 60^o - 100^o result of Chapter 3). It is still possible that the effects on reflected amplitudes by a higher ICB density contrast (above 1 gcm^{-3}) or a mosaic impedance structure could be masked by the scattering effects of very small (~1 km) topography heights. Hence, continued modeling experiments will be required in establishing upper bounds in the ICB density contrast.

- In any case, many studies and reviews up to this point (Tkalčić, 2015) agree that the sparse sampling of the inner core by from seismic waves recorded by the current spatial coverage of seismic networks with respect to seismically active regions is a major obstacle in fine tuning the picture of inner core. There are areas of the inner core under the Pacific and Atlantic oceans that are hardly sampled due to lack of seismic stations in ocean regions. Station placement suggestions for the southern parts of the Indian, Atlantic, and Pacific oceans highlighted in Tkalčić, 2015 would address some of the missing IC samplings. These areas are crucial for a constructing a detailed picture of transitions around hotter and colder (high $T/T_{melting}$) IC surface areas if it is thermally coupled to core-mantle boundary.

Appendix I

Formulation of Boundary Integral Equation

In seismic waves, either elastic or acoustic, the essential quantities we solve for are displacement and pressure. Let us consider the case of acoustic waves first.

The basic underlying principles for the derivation of wave equation are the Hooke's Law (equation 1) and Newton's Second Law (equation 2).

$$\bar{p}(\bar{x},t) = -k\nabla.\bar{u}(\bar{x},t) \qquad \text{Equation 1}$$

$$\rho\ddot{\bar{u}}(\bar{x},t) = -\nabla\bar{p}(\bar{x},t) \qquad \text{Equation 2}$$

Here k is bulk modulus, ρ is density and $\bar{u}$ is displacement vector at point $\bar{x}$ in position and t in time.

In frequency domain equations 1 and 2 can be written as equations 3 and 4.

$$\tilde{P}(\bar{x},\omega) = -k\nabla.\tilde{u}(\bar{x},\omega) \qquad \text{Equation 3}$$

$$(-i\omega)^2 \rho \tilde{u}(\bar{x}, \omega) = -\nabla \tilde{P}(\bar{x}, \omega) \quad \text{Equation 4}$$

Taking the divergence of equation 4,

$$(-i\omega)^2 \rho \nabla . \tilde{u}(\bar{x}, \omega) = -\nabla^2 . P(\bar{x}, \omega) \quad \text{Equation 5}$$

From substituting displacement term in equation 5, from equation 3

$$\frac{\omega^2 \rho}{k} \tilde{P}(\bar{x}, \omega) = -\nabla^2 . \tilde{P}(\bar{x}, \omega)$$

$$\nabla^2 . \tilde{P}(\bar{x}, \omega) + \frac{\omega^2 \rho}{k} \tilde{P}(\bar{x}, \omega) = 0 \quad \text{Equation 6}$$

Wave velocity $c = \sqrt{k/\rho}$ and wave number constant $K = \omega/c$. Hence,

$$\nabla^2 . \tilde{P}(\bar{x}, \omega) + K^2 \tilde{P}(\bar{x}, \omega) = 0 \quad \text{Equation 7}$$

Equation 7 is acoustic wave equation in frequency domain, and it solves for pressure.

We now concentrate on solving for particle velocity (which gives us displacement) due to an applied pressure. Equation 4 which is the frequency domain representation of Newton's Second Law can be re-written in terms of particle velocity $\tilde{v}(\bar{x},\omega) = \dot{\tilde{u}}(\bar{x},\omega)$.

$$(-i\omega)\rho\tilde{v}(\bar{x},\omega) = -\nabla\tilde{P}(\bar{x},\omega)$$

$$\tilde{v}(\bar{x},\omega) = \frac{1}{i\omega\rho}\nabla\tilde{P}(\bar{x},\omega) \qquad \text{Equation 8}$$

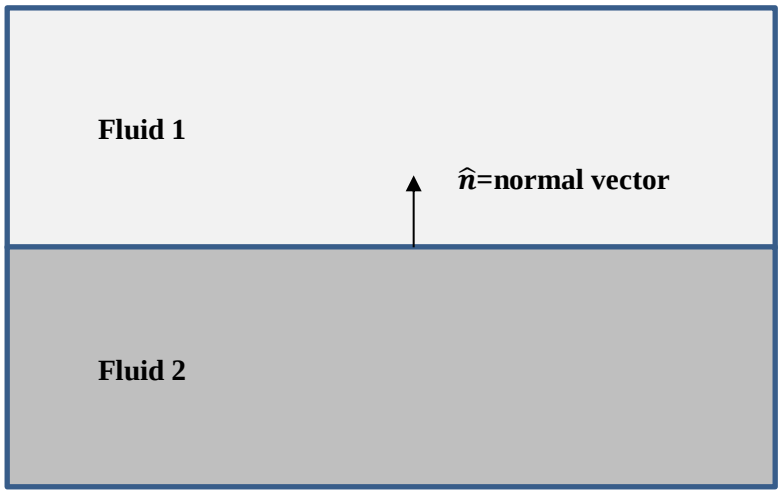

Figure 31: Boundary between two fluid domains.

Consider figure S1,

$$\hat{n}.\tilde{v}(\bar{x},\omega) = \frac{1}{i\omega\rho}\hat{n}.\nabla\tilde{P}(\bar{x},\omega)$$

$$\widetilde{v_n}(\bar{x},\omega) = \frac{1}{i\omega\rho}\frac{\partial\tilde{P}(\bar{x},\omega)}{\partial n} \qquad \text{Equation 9}$$

Now we are interested in solving the acoustic wave equation (7).

Consider the Green's function differential equation in frequency domain.

$$\nabla^2\tilde{G}(x,x_s,\omega) + K^2\tilde{G}(x,x_s,\omega) = -\delta(x-x_s) \qquad \text{Equation 10}$$

$\tilde{G} \times (7) - \tilde{p} \times (10)$:

$$\tilde{G}(x,x_s,\omega)\nabla^2\tilde{P}(x,\omega) - \tilde{P}(x,\omega)\nabla^2\tilde{G}(x,x_s,\omega) = \delta(x-x_s)\tilde{P}(x,\omega) \qquad \text{Equation 11}$$

$$\iiint (\tilde{G}(x,x_s,\omega)\nabla^2\tilde{P}(x,\omega) - \tilde{P}(x,\omega)\nabla^2\tilde{G}(x,x_s,\omega))d^3x = \iiint (\delta(x-x_s)\tilde{P}(x,\omega))d^3x$$

$$\iiint (\tilde{G}(x,x_s,\omega)\nabla^2\tilde{P}(x,\omega) - \tilde{P}(x,\omega)\nabla^2\tilde{G}(x,x_s,\omega))d^3x = \tilde{P}(x_s,\omega) \qquad \text{Equation 12}$$

Gauss's Law states that total flux of a vector A through a closed surface is equals to the volume integral of the divergence of vector A.

$$\iiint \nabla . A(x) d^3x = \oiint A(x) ds$$

Equation 12 can be re-written as,

$$\nabla . [\tilde{G}(x, x_s, \omega) . \nabla \tilde{P}(x, \omega) - \tilde{P}(x, \omega) . \nabla G(x, x_s, \omega)] d^3x = \tilde{P}(x_s, \omega)$$

Using Gauss's Law

$$\oiint \left[\tilde{G}(x, x_s, \omega) . \nabla \tilde{P}(x, \omega) - \tilde{P}(x, \omega) . \nabla G(x, x_s, \omega)\right] ds = \tilde{P}(x_s, \omega)$$

Taking the component in the direction of normal vector,

$$\oiint \left[\tilde{G}(x, x_s, \omega) \hat{n} . \nabla \tilde{P}(x, \omega) - \tilde{P}(x, \omega) \hat{n} . \nabla G(x, x_s, \omega)\right] ds = \tilde{P}(x_s, \omega)$$

$$\oiint \left[\tilde{G}(x, x_s, \omega) \frac{\partial \tilde{P}(x, \omega)}{\partial n} - \tilde{P}(x, \omega) \frac{\partial \tilde{G}(x, \omega)}{\partial n}\right] ds = \tilde{P}(x_s, \omega) \qquad \text{Equation 13}$$

Let's consider taking the integral along the boundary surface. Note that 2D Green's function (~ ln(kr)) goes to infinity as r goes to zero, or as x goes to x_s. This is at the section very close to x_s (i.e. on the self-element in discrete integration). Here, $\frac{\partial \tilde{P}}{\partial n}$ and $\tilde{P}$ are considered constant per element.

So for the self-element, the second term $\tilde{P}(x,\omega)\oiint \frac{\partial \tilde{G}(x,\omega)}{\partial n} ds$ in equation 13, must take a Cauchy principle integral, which gives $\oiint \frac{\partial \tilde{G}(x,\omega)}{\partial n} ds = -\frac{1}{2}$.

Now equation 13 becomes,

$$\oiint_{C.P.} \left[\widetilde{G}(x, x_s, \omega) \frac{\partial \widetilde{P}(x,\omega)}{\partial n} - \widetilde{P}(x,\omega) \frac{\partial \widetilde{G}(x,\omega)}{\partial n} \right] ds = \frac{1}{2} \widetilde{P}(x_s, \omega) \qquad \text{Equation 14}$$

Let us call $\frac{\partial \widetilde{P}(x,\omega)}{\partial n} = q(x,\omega)$. According to equation 9, $\widetilde{v_n}(x,\omega) = \frac{1}{i\omega\rho} q(x,\omega)$.

Considering discrete integration, we write equation 14 in matrix form.

$$Gq - pB = \frac{1}{2} pI$$

$$Gq = \left[B + \frac{1}{2} I \right] p \qquad \text{Equation 15}$$

Here I is identity matrix and B is the vector of $\frac{\partial \tilde{G}(x,\omega)}{\partial n}$ terms.

Now, if there is a body force in the volume a term $\iiint f(x_o)\tilde{G}(x, x_o, \omega)dv$ adds to the left hand side of equation 13. Denoting the vector of these terms as U_0, equation 15 takes the form,

$$Gq + U_0 = \left[B + \frac{1}{2}I\right]p \qquad \text{Equation 16}$$

In the case of outer core and inner core, we have a fluid-solid interface as in figure S2.

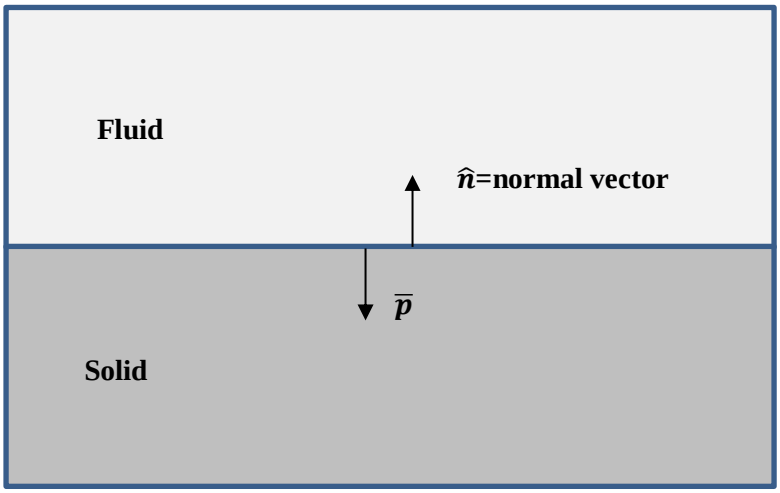

Figure 32: Boundary between a fluid and a solid.

The boundary conditions for fluid-solid interface are;

1) Continuity of normal displacement – say u_n.
2) Continuity of tangential displacement – say u_t.
3) Continuity of normal traction – t_n.
4) Tangential traction is zero - t_t=0.

In fluid domain, from equation 15 we have

$$\frac{1}{2}p = P_0 + G_a q - pB_a \qquad \text{Equation 17}$$

Here P_0 is the body force term. Terms G and B in equation 16 are renamed as G_a and B_a, but still represents the pressure Green's function matrix and velocity-related Green's function matrix.

For solid domain, following gives elastic wave equation for displacement.

$$\nabla^2 . \tilde{u}(\bar{x}, \omega) + K^2 \tilde{u}(\bar{x}, \omega) = 0 \qquad \text{Equation 18}$$

By following a similar process as in steps that derived equations 10 -17, we can write

$$\frac{1}{2}u = U_0 + Gt - uT \qquad \text{Equation 19}$$

Let us assume an M number of discrete boundary elements on the figure x2 fluid-solid interface. Then equation 19 for normal displacement (u_n) and tangential displacement (u_t) gives 2xM equations with 3xM unknowns (i.e. u_n, u_t, and t_n vectors. Here t_t vector is zero).

Now since t_n=-p, equation 17 in fluid domain can be written as

$$-\frac{1}{2}t_n = P_0 + G_a q + t_n B_a \qquad \text{Equation 20}$$

where $\widetilde{v_n}(x,\omega) = \frac{1}{i\omega\rho} q(x,\omega)$. i.e. $\widetilde{u_n}(x,\omega) = \frac{1}{\omega^2\rho} q(x,\omega)$.

With equation 19 and 20 we can obtain 3xM equations with 3xM unknowns.

The same end result matrix system which we need to solve in the boundary element method, is compositely shown in equations (1) and (2) in chapter 2.

REFERENCES

Adam, J. M.-C. and Romanowicz, B. (2015) 'Global scale observations of scattered energy near the inner-core boundary: Seismic constraints on the base of the outer-core', *Physics of the Earth and Planetary Interiors*. Elsevier B.V., 245, pp. 103–116. doi: 10.1016/j.pepi.2015.06.005.

Alboussiere, T., Deguen, R. and Melzani, M. (2010) 'Melting-induced stratification above the Earth's inner core due to convective translation', 466(August). doi: 10.1038/nature09257.

Attanayake, J. (2012) *Seismic Structure and Geodynamics of Earth's Upper Inner Core and the F Region*. University of Connecticut.

Attanayake, J., Cormier, V. F. and De Silva, S. M. (2014) 'Uppermost inner core seismic structure - new insights from body waveform inversion', *Earth and Planetary Science Letters*. doi: 10.1016/j.epsl.2013.10.025.

Aubert, J. *et al.* (2008) 'Thermochemical flows couple the Earth's inner core growth to mantle heterogeneity.', *Nature*, 454(7205), pp. 758–761. doi: 10.1038/nature07109.

Bergman, M. I. (1998) 'Estimates of the Earth's inner core grain size', *Geophysical Research Letters*, 25(10), pp. 1593–1596. doi: 10.1029/98GL01239.

Bergman, M. I. (2003) 'Solidification of the Earth's core', in *Dehant V., Creager K., Zatman S. & Karato S-I. eds. Earth's Core: Dynamics, Structure, Rotation*. 31st edn. American Geophysical Union Geodynamics Series, pp. 105 – 127.

Bergman, M. I. *et al.* (2010) 'Grain growth and loss of texture during annealing of alloys, and the translation of Earths inner core', *Geophysical Research Letters*, 37(22). doi: 10.1029/2010GL045103.

Birch, F. (1940) 'The alpha – gamma transformation of iron at high pressures, and the problem of the Earth's magnetism', *American Journal of Science*, (238), pp. 192 – 211.

Blom, N. A. *et al.* (2015) 'Inner core structure behind the PKP core phase triplication', *Geophysical Journal International*, 201(3), pp. 1657–1665. doi: 10.1093/gji/ggv103.

Bogiatzis, P., Ishii, M. and Davis, T. A. (2016) 'Towards using direct methods in seismic tomography: Computation of the full resolution matrix using high-performance computing and sparse QR factorization', *Geophysical Journal International*, 205(2), pp. 830–836. doi: 10.1093/gji/ggw052.

Bolt, B. A., and A. Q. (1970) 'Upper bound to the density jump at the boundary of the Earth's inner core', *Nature*, 228, pp. 148–150.

Bolt, B. A. (1976) *Nuclear explosions and earthquakes. The parted vail.* United States: W. H. Freeman and Co.,San Francisco.

Bolt, B. A. (1993) *Earthquakes and geological discovery*, *Scientific American library series*,.

Buffett, B. A. (1997) 'Geodynamic estimates of the viscosity of the Earth's inner core', *Nature*, 388(6642), pp. 571–573. doi: 10.1038/41534.

Buffett, B. A. and Creager, K. C. (1999) 'A comparison of geodetic and seismic estimates of inner-core rotation', *Geophysical Research Letters*, 26(10), pp. 1509–1512. doi:

10.1029/1999GL900271.

Bullen, K. E. (1940) ‘The problem of the Earth’s density variation’, *Bull, of the Seismo. Soc. of Am.*, 30, pp. 235–250.

Bullen, K. E. (1942) ‘The Density Variation of the Earths Central Core’, *Bull. Seismol. Soc. Amer*, 32, pp. 19–29.

Bullen, K. E. (1946) ‘A hypothesis on compressibility at pressures of the order of a million atmospheres’, *Nature*, 157, p. 405.

Cao, A., Masson, Y. and Romanowicz, B. (2007) ‘Short wavelength topography on the inner-core boundary.’, *Proceedings of the National Academy of Sciences of the United States of America*. doi: 10.1073/pnas.0609810104.

Cao, A. and Romanowicz, B. (2004a) ‘Constraints on density and shear velocity contrasts at the inner core boundary’, *Geophysical Journal International*, 157(3), pp. 1146–1151. doi: 10.1111/j.1365-246X.2004.02330.x.

Cao, A. and Romanowicz, B. (2004b) ‘Hemispherical transition of seismic attenuation at the top of the earth’s inner core’, *Earth and Planetary Science Letters*, 228(3–4), pp. 243–253. doi: 10.1016/j.epsl.2004.09.032.

Caro, G. (2011) ‘Early Silicate Earth Differentiation’, *Annual Review of Earth and Planetary Sciences*, 39(1), pp. 31–58. doi: 10.1146/annurev-earth-040610-133400.

Cerveny, V. (2001). Seismic ray theory. *Cambridge University Press*.

Chambers, J. E. (2001) ‘Making More Terrestrial Planets’, *Icarus*, 152, p. 205. doi: 10.1006/icar.2001.6639.

Chambers, J. E. (2004) 'Planetary accretion in the inner Solar System', *Earth and Planetary Science Letters*, 223(3–4), pp. 241–252. doi: 10.1016/j.epsl.2004.04.031.

Chapman, C. (2004). *Fundamentals of Seismic Wave Propagation*. *Books* (Vol. XXXIII). https://doi.org/10.1017/CBO9780511616877

Cormier, F., Xu, L. and Choy, G. L. (1998) 'Seismic attenuation of the inner core: Viscoelastic or stratigraphic?', 25(21), pp. 4019–4022.

Cormier, V. F. (2000) 'D'' as a transition in the heterogeneity spectrum of the lowermost mantle', *Journal of Geophysical Research*, 105, pp. 16193–16205. doi: 10.1029/2000JB900141.

Cormier, V. F. (2007) 'Texture of the uppermost inner core from forward- and back-scattered seismic waves', *Earth and Planetary Science Letters*, 258(3–4), pp. 442–453. doi: http://dx.doi.org/10.1016/j.epsl.2007.04.003.

Cormier, V. F. (2009) 'A glassy lowermost outer core', *Geophysical Journal International*, 179(1), pp. 374–380. doi: 10.1111/j.1365-246X.2009.04283.x.

Cormier, V. F. and Attanayake, J. (2013) 'Earth's solid inner core: Seismic implications of freezing and melting', *Journal of Earth Science*, 24(5), pp. 683–698. doi: 10.1007/s12583-013-0363-9.

Cormier, V. F., Attanayake, J. and He, K. (2011) 'Inner core freezing and melting: Constraints from seismic body waves', *Physics of the Earth and Planetary Interiors*. Elsevier B.V., 188(3–4, SI), pp. 163–172. doi: 10.1016/j.pepi.2011.07.007.

Cormier, V. F. and Li, X. (2002) 'Frequency-dependent seismic attenuation in the inner

core 2. A scattering and fabric interpretation', *Journal of Geophysical Research*, 107, p. 2362.

Creager, K. C. (1997) 'Inner Core Rotation Rate from Small-Scale Heterogeneity and Time-Varying Travel Times', *Science*, 278(5341), pp. 1284–1288. doi: 10.1126/science.278.5341.1284.

Crotwell, H. P., Owens, T. J. and Ritsema, J. (1999) 'The TauP Toolkit: Flexible Seismic Travel-time and Ray-path Utilities', *Seismological Research Letters*, 70(2), pp. 154–160. doi: 10.1785/gssrl.70.2.154.

Dai, Z., Wang, W. and Wen, L. (2012) 'Irregular topography at the Earth's inner core boundary', *Proceedings of the National Academy of Sciences*. doi: 10.1073/pnas.1116342109.

Deguen, R. (2012) 'Structure and dynamics of Earth's inner core', *Earth and Planetary Science Letters*, 333–334, pp. 211–225. doi: 10.1016/j.epsl.2012.04.038.

Deguen, R., Alboussiere, T. and Brito, D. (2007) 'On the existence and structure of a mush at the inner core boundary of the Earth', *Physics of the Earth and Planetary Interiors*, 164(1–2), pp. 36–49. doi: 10.1016/j.pepi.2007.05.003.

Deuss, A., Irving, J. C. E. and Woodhouse, J. H. (2010) 'Regional variation of inner core anisotropy from seismic normal mode observations.', *Science (New York, N.Y.)*. doi: 10.1126/science.1188596.

Dziewonski, A. M. and Anderson, D. L. (1981) 'Preliminary reference Earth model', *Physics of the Earth and Planetary Interiors*, 25(4), pp. 297–356. doi: 10.1016/0031-

9201(81)90046-7.

Furumura, M., Kennett, B. L. N. and Furumura, T. (1999) 'Seismic wavefield calculation for laterally heterogeneous earth models-II. The influence of upper mantle heterogeneity', *Geophysical Journal International*, 139(3), pp. 623–644. doi: 10.1046/j.1365-246X.1999.00962.x.

Glatzmaier, G. A. and Roberts, P. H. (1996) 'Rotation and magnetism of earth's inner core', *Science*, 274(5294), pp. 1887–1891. doi: 10.1126/science.274.5294.1887.

Gribb, T. T. and Cooper, R. F. (1998) 'Low-frequency shear attenuation in polycrystalline olivine: Grain boundary diffusion and the physical significance of the Andrade model for viscoelastic rheology', *JOURNAL OF GEOPHYSICAL RESEARCH*, 103, pp. 27267–27279.

Gubbins, D. (1981) 'Rotation of the inner core - Gubbins - 2012 - Journal of Geophysical Research: Solid Earth (1978–2012) - Wiley Online Library', *Journal of Geophysical …*. Available at: http://www.agu.org/pubs/crossref/1981/JB086iB12p11695.shtml%5Cnfile:///Articles/1981/Gubbins/J. Geophys. Res. 1981 Gubbins.pdf.

Gubbins, D. *et al.* (2003) 'Can the Earth's dynamo run on heat alone?', *Geophysical Journal Of The Royal Astronomical Society*, 155(2), pp. 609–622. doi: 10.1046/j.1365-246X.2003.02064.x.

Gubbins, D. *et al.* (2011) 'Melting of the Earth's inner core.', *Nature*, 473(7347), pp. 361–363. doi: 10.1038/nature10068.

Gubbins, D., Masters, G. and Nimmo, F. (2008) ‘A thermochemical boundary layer at the base of Earth’s outer core and independent estimate of core heat flux’, *Geophysical Journal International*, 174(3), pp. 1007–1018. doi: 10.1111/j.1365-246X.2008.03879.x.

Gutenberg, B. (1914) ‘Ueber Erdbebenwellen. VII A. Beobachtungen an Registrierungen von Fernbeben in Göttingen und Folgerung über die Konstitution des Erdkörpers (mit Tafel).’, *Nachrichten von der Gesellschaft der Wissenschaften zu Göttingen, Mathematisch-Physikalische Klasse*, 1914, p. 125–176.

Houser, C. *et al.* (2008) ‘Shear and compressional velocity models of the mantle from cluster analysis of long-period waveforms’, *Geophysical Journal International*, 174(1), pp. 195–212. doi: 10.1111/j.1365-246X.2008.03763.x.

Iritani, R., Takeuchi, N. and Kawakatsu, H. (2014a) ‘Intricate heterogeneous structures of the top 300 km of the Earth’s inner core inferred from global array data: II. Frequency dependence of inner core attenuation and its implication’, *Earth and Planetary Science Letters*, 405, pp. 231–243. doi: 10.1016/j.epsl.2014.08.038.

Iritani, R., Takeuchi, N. and Kawakatsu, H. (2014b) ‘Intricate heterogeneous structures of the top 300km of the Earth’s inner core inferred from global array data: I. Regional 1D attenuation and velocity profiles’, *Physics of the Earth and Planetary Interiors*, 230, pp. 15–27. doi: 10.1016/j.pepi.2014.02.002.

Irving, J. C. E. and Deuss, A. (2011) ‘Hemispherical structure in inner core velocity anisotropy’, *Journal of Geophysical Research: Solid Earth*. doi: 10.1029/2010JB007942.

Irving, J. C. E. and Deuss, A. (2015) ‘Regional seismic variations in the inner core under the North Pacific’, *Geophysical Journal International*, 203(3), pp. 2189–2199. doi:

10.1093/gji/ggv435.

Ishii, M. and Dziewoński, A. M. (2002) 'The innermost inner core of the earth: evidence for a change in anisotropic behavior at the radius of about 300 km.', *Proceedings of the National Academy of Sciences of the United States of America*, 99, pp. 14026–14030. doi: 10.1073/pnas.172508499.

Ishii, M. and Dziewoński, A. M. (2003) 'Distinct seismic anisotropy at the centre of the Earth', *Physics of the Earth and Planetary Interiors*, 140(1–3), pp. 203–217. doi: 10.1016/j.pepi.2003.07.015.

Jackson, D. D. and Anderson, D. L. (1970) 'Physical mechanisms of seismic-wave attenuation', *Reviews of Geophysics*, 8(1), pp. 1–63. doi: 10.1029/RG008i001p00001.

Jackson, I. (1998) 'Elasticity, composition and temperature of the Earth's lower mantle: a reappraisal', *Geophysical Journal International*, 134(1), pp. 291–311. doi: 10.1046/j.1365-246X.1998.00560.x.

Jackson, I. *et al.* (2002) 'Grain-size-sensitive seismic wave attenuation in polycrystalline olivine', *Journal of Geophysical Research: Solid Earth*, 107(B12), p. ECV 5-1-ECV 5-16. doi: 10.1029/2001JB001225.

Jeffreys, H. (1926) 'The rigidity of the Earth's central core', *Monthly Notices of the Royal Astronomical Society of London, Geophysical Supplements*, 1, pp. 371 – 383.

Jeffreys, H. and Bullen, K. E. (1958) *Seismological tables*. Office of the British Association.

Kaneshima, S. *et al.* (1994) 'Seismic structure near the inner core-outer core boundary',

21(2), pp. 157–160.

Kennet, B. L. N. (1988) ‘Systematic approximations to the seismic wavefield’, in Doornbos, D. J. (ed.) *Seismological Algorithms: Computational Methods and Computer Programs*. Academic Press, London, pp. 237–259.

Kennett, B. L. N., Engdahl, E. R. and Buland, R. (1995) ‘Constraints on seismic velocities in the Earth from travel times’, *Geophysical Journal International*, 122, pp. 108–124. doi: 10.1111/j.1365-246X.1995.tb03540.x.

Koelemeijer, P. *et al.* (2016) ‘SP12RTS: A degree-12 model of shear- and compressional-wave velocity for Earth’s mantle’, *Geophysical Journal International*, 204(2), pp. 1024–1039. doi: 10.1093/gji/ggv481.

Koper, K. D. and Dombrovskaya, M. (2005) ‘Seismic properties of the inner core boundary from PKiKP/P amplitude ratios’, *Earth and Planetary Science Letters*, 237(3–4), pp. 680–694. doi: 10.1016/j.epsl.2005.07.013.

Koper, K. D., Franks, J. M. and Dombrovskaya, M. (2004) ‘Evidence for small-scale heterogeneity in Earth’s inner core from a global study of PKiKP coda waves’, *Earth and Planetary Science Letters*, 228(3–4), pp. 227–241. doi: 10.1016/j.epsl.2004.10.027.

Koper, K. D. and Pyle, M. L. (2004) ‘Observations of PKiKP / PcP amplitude ratios and implications for Earth structure at the boundaries of the liquid core’, *Journal of Geophysical Research*, 109(B3), pp. 1–13. doi: 10.1029/2003JB002750.

Krasnoshchekov, D. N., Kaazik, P. B. and Ovtchinnikov, V. M. (2005) ‘Seismological evidence for mosaic structure of the surface of the Earth’s inner core.’, *Nature*,

435(7041), pp. 483–487. doi: 10.1038/nature03613.

Kustowski, B., Ekström, G. and Dziewoński, A. M. (2008) 'Anisotropic shear-wave velocity structure of the earth's mantle: A global model', *Journal of Geophysical Research: Solid Earth*, 113(6). doi: 10.1029/2007JB005169.

Labrosse, S., Poirier, J. P. and Le Mouël, J. L. (2001) 'The age of the inner core', *Earth and Planetary Science Letters*, 190(3–4), pp. 111–123. doi: 10.1016/S0012-821X(01)00387-9.

Lasbleis, M., Hernlund, J. W. and Labrosse, S. (2015) 'Snow Model for the F-Layer', in *AGU Fall Meeting Abstracts*.

Lehmann, I. (1936) 'P'', *Bureau Central Séismologique International Strasbourg: Publications du Bureau Central Scientifiques*, A14(3), pp. 87–115.

Leykam, D., Tkalčić, H. and Reading, A. M. (2010) 'Core structure re-examined using new teleseismic data recorded in Antarctica: Evidence for, at most, weak cylindrical seismic anisotropy in the inner core', *Geophysical Journal International*, 180(3), pp. 1329–1343. doi: 10.1111/j.1365-246X.2010.04488.x.

Leyton, F. and Koper, K. D. (2007) 'Using PKiKP coda to determine inner core structure: 1. Synthesis of coda envelopes using single-scattering theories', *Journal of Geophysical Research: Solid Earth*, 112(5). doi: 10.1029/2006JB004369.

Li, D., Sun, D. and Helmberger, D. (2014) 'Notes on the variability of reflected inner core phases', *Earthquake Science*, 27(4), pp. 441–468. doi: 10.1007/s11589-014-0093-9.

Li, X. and Cormier, V. F. (2002) 'Frequency-dependent seismic attenuation in the inner

core, 1. A viscoelastic interpretation', *Journal of Geophysical Research*, 107, p. 2361. doi: 10.1029/2002JB001795.

Lister, J. R. and Buffett, B. A. (1995) 'The strength and efficiency of thermal and compositional convection in the geodynamo', *Physics of the Earth and Planetary Interiors*, 91(1–3), pp. 17–30. doi: 10.1016/0031-9201(95)03042-U.

Masters, G. and GIlbert, F. (1981) 'Structure of the inner core inferred from observations of its spheroidal shear modes', *Geophys. Res. Lett*, 8(6), pp. 569–571.

McDonough, W. F. (2013) 'Compositional Model for the Earth's Core', in *Treatise on Geochemistry: Second Edition*, pp. 559–577. doi: 10.1016/B978-0-08-095975-7.00215-1.

Monnereau, M. *et al.* (2010) 'Lopsided Growth of Earth's Inner Core', *Science*, 328(5981), pp. 1014–1017. doi: 10.1126/science.1186212.

Montagner, J.-P. and Kennett, B. L. N. (1996) 'How to reconcile body-wave and normal-mode reference earth models', *Geophysical Journal International*, 125, pp. 229–248. doi: 10.1111/j.1365-246X.1996.tb06548.x.

Morelli, A., Dziewonski, A. M. and Woodhouse, J. H. (1986) 'Anisotropy of the inner core inferred from PKIKP travel times', *Geophysical Research Letters*, 13(13), pp. 1545–1548. doi: 10.1029/GL013i013p01545.

Niu, F. and Chen, Q.-F. (2008) 'Seismic evidence for distinct anisotropy in the innermost inner core', *Nature Geoscience*, 1(October), pp. 692–696. Available at: http://dx.doi.org/10.1038/ngeo314.

Niu, F. L. and Wen, L. X. (2001) 'Hemispherical variations in seismic velocity at the top

of the Earth's inner core', *Nature*, 410(6832), pp. 1081–1084. doi: 10.1038/35074073.

Ohtaki, T. and Kaneshima, S. (2015) 'Independent estimate of velocity structure of Earth's lowermost outer core beneath the northeast Pacific from PKiKP - PKPbc differential traveltime and dispersion in PKPbc', *Journal of Geophysical Research B: Solid Earth*, 120(11), pp. 7572–7586. doi: 10.1002/2015JB012140.

Ohtaki, T., Kaneshima, S. and Kanjo, K. (2012) 'Seismic structure near the inner core boundary in the south polar region', *Journal of Geophysical Research: Solid Earth*, 117(3), pp. 1–15. doi: 10.1029/2011JB008717.

Oldham, R. D. (1907) 'The Constitution of the Interior of the Earth, as revealed by Earthquakes: (Second Communication). Some New Light on the Origin of the Oceans', *Quarterly Journal of the Geological Society*, 63(1–4), pp. 344–350. doi: 10.1144/GSL.JGS.1907.063.01-04.24.

Oreshin, S. I. (2004) 'Heterogeneity and anisotropy of seismic attenuation in the inner core', *Geophysical Research Letters*, 31(2), p. L02613. doi: 10.1029/2003GL018591.

Panning, M. and Romanowicz, B. (2006) 'A three-dimensional radially anisotropic model of shear velocity in the whole mantle', *Geophysical Journal International*, 167(1), pp. 361–379. doi: 10.1111/j.1365-246X.2006.03100.x.

Pejić, T. *et al.* (2017) 'Attenuation tomography of the upper inner core', *Journal of Geophysical Research: Solid Earth*. doi: 10.1002/2016JB013692.

Peng, Z. *et al.* (2008) 'Inner-core fine-scale structure from scattered waves recorded by LASA', *Journal of Geophysical Research: Solid Earth*, 113(9). doi:

10.1029/2007JB005412.

Pointer, T., Liu, E. and Hudson, J. A. (1998) ‘Modelling Seismic Waves Scattered by Hydrofractures Using the Boundary Element Method’, in *60th Mtg.*

Poupinet, G., Pillet, R. and Souriau, A. (1983) ‘Possible heterogeneity of the Earth’s core deduced from PKIKP travel times’, *Nature*, 305(5931), pp. 204–206. doi: 10.1038/305204a0.

Ritsema, J. *et al.* (2011) ‘S40RTS: A degree-40 shear-velocity model for the mantle from new Rayleigh wave dispersion, teleseismic traveltime and normal-mode splitting function measurements’, *Geophysical Journal International*, 184(3), pp. 1223–1236. doi: 10.1111/j.1365-246X.2010.04884.x.

Sánchez-Sesma, F. and Campillo, M. (1991) ‘Diffraction of P, SV, and Rayleigh waves by topographic features: A boundary integral formulation’, *Bulletin of the Seismological Society of America*, 81(6), pp. 2234–2253. Available at: http://www.bssaonline.org/content/81/6/2234.short.

Schubert, G. (2007). *Treatise on Geophysics*. *Treatise on Geophysics* (Vol. 1–10). https://doi.org/10.1016/C2009-1-28330-4

Shearer, P. M. and Masters, G. G. (1990) ‘The density and shear velocity contrast at the inner core boundary’, *Geophysical Journal International*, 102(2), pp. 491–498. doi: 10.1111/j.1365-246X.1990.tb04481.x.

Shearer, P. (2009). *Introduction to Seismology*.

Simmons, N. A., Forte, A. M. and Grand, S. P. (2009) 'Joint seismic, geodynamic and mineral physical constraints on three-dimensional mantle heterogeneity: Implications for the relative importance of thermal versus compositional heterogeneity', *Geophysical Journal International*, 177(3), pp. 1284–1304. doi: 10.1111/j.1365-246X.2009.04133.x.

Song, X. (2000) 'Joint inversion for inner core rotation, inner core anisotropy, and mantle heterogeneity', *Journal of Geophysical …*, 105(B4), p. 7931. doi: 10.1029/1999JB900436.

Song, X. and Helmberger, D. V. (1995) 'A P wave velocity model of Earth's core', *Journal of Geophysical Research*, 100(B6), p. 9817. doi: 10.1029/94JB03135.

Song, X. and Richards, P. G. (1996a) 'Seismological evidence for differential rotation of the Earth's inner core', *Nature*, pp. 221–224. doi: 10.1038/382221a0.

Song, X. and Richards, P. G. (1996b) 'Seismological evidence for differential rotation of the Earth's inner core', *Nature*. doi: 10.1038/382221a0.

Souriau, A. and Poupinet, G. (1991) 'The Velocity Profile At the Base of the Liquid Core From Pkp(Bc+Cdiff) Data - an Argument in Favor of Radial Inhomogeneity', *Geophysical Research Letters*, 18(11), pp. 2023–2026. doi: 10.1029/91gl02417.

Souriau, A. and Romanowicz, B. (1996) 'Anisotropy in inner core attenuation: A new type of data to constrain the nature of the solid core', *Geophysical Research Letters*, 23(1), p. 1. doi: 10.1029/95GL03583.

Souriau, A. and Souriau, M. (1989) 'Ellipticity and density at the inner core boundary from subcritical PKiKP and PcP data', *Geophysical Journal International*, 98(1), pp. 39–

54. doi: 10.1111/j.1365-246X.1989.tb05512.x.

Stevenson, D. J. (1987) ‘Limits on lateral density and velocity variations in the Earth’s outer core’, *Geophysical Journal International*, 88(1), pp. 311–319.

Stroujkova, A. and Cormier, V. F. (2004) ‘Regional variations in the uppermost 100 km of the Earth’s inner core’, *Journal of Geophysical Research B: Solid Earth*, 109, pp. 1–8. doi: 10.1029/2004JB002976.

Su, W., Dziewonski, A. and Jeanloz, R. (1996) ‘Planet Within a Planet: Rotation of the Inner Core of Earth’, *Science (New York, N.Y.)*, 274(5294), pp. 1883–7. doi: 10.1126/science.274.5294.1883.

Su, W. J. and Dziewonski, A. M. (1995) ‘INNER-CORE ANISOTROPY IN 3 DIMENSIONS’, *Journal of Geophysical Research-Solid Earth*, 100(B6), pp. 9831–9852.

Sun, X. and Song, X. (2008) ‘The inner inner core of the Earth: Texturing of iron crystals from three-dimensional seismic anisotropy’, *Earth and Planetary Science Letters*, 269(1–2), pp. 56–65. doi: 10.1016/j.epsl.2008.01.049.

Tanaka, S. (2012) ‘Depth extent of hemispherical inner core from PKP(DF) and PKP(Cdiff) for equatorial paths’, *Physics of the Earth and Planetary Interiors*, 210–211, pp. 50–62. doi: 10.1016/j.pepi.2012.08.001.

Tanaka, S. and Hamaguchi, H. (1997) ‘Degree one heterogeneity and hemispherical variation of anisotropy in the inner core from PKP(BC)–PKP(DF) times’, *J. Geophys. Res.*, 102(B2), pp. 2925–2938. doi: 10.1029/96jb03187.

Tanaka, S. and Tkalčić, H. (2015) ‘Complex inner core boundary from frequency

characteristics of the reflection coefficients of PKiKP waves observed by Hi-net', *Progress in Earth and Planetary Science*, 2(1), p. 34. doi: 10.1186/s40645-015-0064-3.

Tkalčić, H. (2010) 'Large variations in travel times of mantle-sensitive seismic waves from the South Sandwich Islands: Is the Earth's inner core a conglomerate of anisotropic domains?', *Geophysical Research Letters*, 37(14). doi: 10.1029/2010GL043841.

Tkalčić, H. *et al.* (2013) 'The shuffling rotation of the Earth's inner core revealed by earthquake doublets', *Nature Geoscience*, 6(6), pp. 497–502. doi: 10.1038/ngeo1813.

Tkalčić, H. (2015) 'Reviews of Geophysics Complex inner core of the Earth: The last frontier of global seismology', *Rev. Geophys*, 53. doi: 10.1002/2014RG000469.

Tkalčić, H., Kennett, B. L. N. and Cormier, V. F. (2009) 'On the inner-outer core density contrast from PKiKP/PcP amplitude ratios and uncertainties caused by seismic noise', *Geophysical Journal International*, 179(1), pp. 425–443. doi: 10.1111/j.1365-246X.2009.04294.x.

Tromp, J. (1993) 'Support for anisotropy of the Earth's inner core from free oscillations', *Nature*, 366(6456), pp. 678–681. doi: 10.1038/366678a0.

Vidale, J. E., Dodge, D. a. and Earle, P. S. (2000) 'Slow differential rotation of the Earth's inner core indicated by temporal changes in scattering', *Nature*, 405(MAY), pp. 445–448. doi: 10.1038/35013039.

Vidale, J. E. and Earle, P. S. (2000) 'Fine-scale heterogeneity in the Earth's inner core', *Nature*, 404(6775), pp. 273–5. doi: 10.1038/35005059.

Walter, M. J. and Trønnes, R. G. (2004) 'Early earth differentiation', *Earth and*

Planetary Science Letters, pp. 253–269. doi: 10.1016/j.epsl.2004.07.008.

Wang, T., Song, X. and Xia, H. H. (2015) 'Equatorial anisotropy in the inner part of Earth's inner core from autocorrelation of earthquake coda', *Nature Geoscience*, 8(February), pp. 1–4. doi: 10.1038/NGEO2354.

Waszek, L. and Deuss, A. (2011) 'Distinct layering in the hemispherical seismic velocity structure of Earth's upper inner core', *Journal of Geophysical Research: Solid Earth*, 116(12). doi: 10.1029/2011JB008650.

Waszek, L. and Deuss, A. (2015) 'Anomalously strong observations of PKiKP/PcP amplitude ratios on a global scale', *Journal of Geophysical Research B: Solid Earth*, 120(7), pp. 5175–5190. doi: 10.1002/2015JB012038.

Waszek, L., Irving, J. and Deuss, A. (2011) 'Reconciling the hemispherical structure of Earth's inner core with its super-rotation', *Nature Geoscience*. doi: 10.1038/ngeo1083.

Wen, L. (2006) 'Localized temporal change of the Earth's inner core boundary.', *Science (New York, N.Y.)*, 314(2006), pp. 967–970. doi: 10.1126/science.1131692.

Wen, L. and Niu, F. (2002) 'Seismic velocity and attenuation structures in the top of the Earth's inner core', *Journal of Geophysical Research: Solid Earth*, 107(B11), p. ESE 2-1-ESE 2-13. doi: 10.1029/2001JB000170.

Woodhouse, J. H., Giardini, D. and Li, X. ???D (1986) 'Evidence for inner core anisotropy from free oscillations', *Geophysical Research Letters*, 13(13), pp. 1549–1552. doi: 10.1029/GL013i013p01549.

Wookey, J. and Helffrich, G. R. (2008) 'Inner-core shear-wave anisotropy and texture

from an observation of PKJKP waves.', *Nature*, 454(7206), pp. 873–876. doi: 10.1038/nature07131.

Wu, W. and Irving, J. C. E. (2017) 'Using PKiKP coda to study heterogeneity in the top layer of the inner core's western hemisphere', *Geophysical Journal International*, 209(2), pp. 672–687. doi: 10.1093/gji/ggx047.

Yao, J., Sun, L. and Wen, L. (2015) 'Two decades of temporal change of Earth's inner core boundary', *Journal of Geophysical Research B: Solid Earth*, 120(9), pp. 6263–6283. doi: 10.1002/2015JB012339.

Yoshida, S., Sumita, I. and Kumazawa, M. (1996) 'Growth model of the inner core coupled with the outer core dynamics and the resulting elastic anisotropy', *Journal of Geophysical Research*, 101(B12), p. 28085. doi: 10.1029/96JB02700.

Yu, W. C. and Wen, L. (2007) 'Complex seismic anisotropy in the top of the Earth's inner core beneath Africa', *Journal of Geophysical Research: Solid Earth*, 112(8). doi: 10.1029/2006JB004868.

Yu, W. C., Wen, L. and Niu, F. (2005) 'Seismic velocity structure in the earth's outer core', *Journal of Geophysical Research B: Solid Earth*, 110(2), pp. 1–22. doi: 10.1029/2003JB002928.

Zhang, J., Richards, P. G. and Schaff, D. P. (2008) 'Wide-scale detection of earthquake waveform doublets and further evidence for inner core super-rotation', *Geophysical Journal International*, 174(3), pp. 993–1006. doi: 10.1111/j.1365-246X.2008.03856.x.

Zou, Z., Koper, K. D. and Cormier, V. F. (2008) 'The structure of the base of the outer

core inferred from seismic waves diffracted around the inner core', *Journal of Geophysical Research: Solid Earth*, 113(5), pp. 1–13. doi: 10.1029/2007JB005316.